UNIVERSITY OF CALIFORNIA

Santa Barbara

Glacial-Interglacial changes in sea level and seawater delta-O-18 gradients

A dissertation submitted in partial satisfaction of the

requirements for the degree Doctor of Philosophy

in Marine Science

by

Rachel M. Spratt

Committee in charge:

Professor Lorraine Lisiecki, Chair

Professor David Lea

Professor Syee Weldeab

Professor Timothy DeVries

March 2020

The dissertation of Rachel M. Spratt is approved.

Timothy DeVries

David Lea

Syee Weldeab

Lorraine Lisiecki Committee Chair

March 2020

Glacial-Interglacial changes in sea level and seawater delta-O-18 gradients

by

Rachel M. Spratt

DEDICATION

I dedicate this dissertation to David Douglas Livingston, whose affinity for the natural world exceeded mine; he continues to provide me with a template for observation, appreciation, and enthusiasm for the wilderness, the ocean, and their inhabitants.

ACKNOWLEDGEMENTS

I would like to thank Dr. Lisiecki for her assistance in helping me to understand the importance of easy-to-read prose and easily-understood science, and for supporting me during all of my summers here at UCSB. I'd like to thank Dr. David Lea for sharing with me the importance of transparent collaboration and direct and positive communication. I'd also like to thank Dr. Syee Weldeab for being a very interesting and creative teacher. I'd like to thank Libe Washburn (UCSB) and Dr. Mary Spratt (PhD in biology) for being terrific sounding-boards for me during my time at UCSB. Thank you to IGPMS Chairman David Siegel for his support of me on a variety of grant support and for positive encouragement throughout my time at UCSB. Thank you to Dr. Qinghua Ding for sharing his model-data and experiments. Thank you to my best friend David Livingston for all the fun times exploring the geology and wilderness of the Central Coast during my time here at UCSB.

VITA OF RACHEL M. SPRATT
March 2020

EDUCATION

Bachelor of Arts in Biology, Swarthmore College, Swarthmore, PA, June 1990
Bachelor of Arts in Mathematics, Lehman College, City University of New York, June 2012
Doctor of Philosophy in Marine Science, University of California, Santa Barbara, June 2020 (expected)

PROFESSIONAL EMPLOYMENT

2013-2020: Teaching Assistant, Department of Geology, University of California, Santa Barbara
Summer 2018, Fall 2019: Instructor of Record, Department of Geology, University of California, Santa Barbara
Summer 2013 and 2012: Researcher, Computer Modeling and Simulation Conferences, Department of Computer Science, City University of New York, Lehman College

PUBLICATION

A Late Pleistocene sea level stack**,** Climate of the Past, 12, 10791092, doi:/ 10.5194/ cp1210792016, 2016.

AWARDS

Marine Science Departmental grant, University of California, Santa Barbara**,** 2019, 2018

STEM Fellows Award, University of California, Santa Barbara, 2015

Women in Science and Engineering Award, University of California, Santa Barbara, 2014

FIELDS OF STUDY

Major Field: Marine Science

Climate studies with Professors Lorraine Lisiecki and David Lea

Studies in time series analysis and atmospheric dynamics with Professors Leila Carvalho and Charles Jones

Biogeochemical isotope studies and foraminiferal laboratory experience with Professor Syee Weldeab

ABSTRACT

Glacial-Interglacial changes in sea level and seawater delta-O-18 gradients

by

Rachel M. Spratt

Climate states of warm and cold periods have varied on approximately 100,000 year cycles for the last million years. These climate states are represented in similar patterns of global sea level observed in five to seven individual records of sea level over 800-kyr. These records were combined into a 800-kyr long global stack using principal components analysis. A record of $\delta^{18}O$ of benthic foraminiferal calcite shows a correlation of 0.9 to the sea level stack (PC1), suggesting a strong sea level influence in the calcite, but a 2-kyr lag with respect to the calcite record suggests that deep ocean temperature precedes the sea level response. Sea level change is estimated to account for nearly 45% of the 100-kyr power of benthic $\delta^{18}O$.

The principal component analysis also captured regional variation in the sea level records in PC2 and PC3. Regional variations in $\delta^{18}O_{seawater}$ during the modern/Holocene and Last Glacial Maximum (LGM), respectively, may help us to understand ocean and

atmospheric circulation associated with these extreme climate changes. A simple three-box model of the Atlantic Ocean was compared to surface and deep gradients in $\delta^{18}O_{sw}$ from paleoclimate proxy measurements. First, parameters were tuned to realistic modern values that matched modern δ_{sw} observations. The estimated LGM parameters did not fit the proxy evidence for a surface gradient change of -0.04 per mil (‰) or a vertical gradient change of 0.36 ‰. However, the error in the proxy surface and vertical gradient change estimates is quite large (+/-0.29 ‰ and +/-0.14 ‰, respectively). An improved fit to the data was achieved by slowing the overturning circulation while increasing Arctic runoff to a modern value. The results of this study suggest that additional LGM $\delta^{18}O_{sw}$ measurements are needed to constrain ocean and atmospheric circulation changes.

TABLE OF CONTENTS

I Introduction

A deep understanding of past climates and their causes can assist in better comprehending the present climate state. Rising greenhouse gas concentrations will produce warming and ice volume change. However, limitations in studies of past sea level and the causes of cooler and warmer climate come from the combined nature of long-term datasets: for example, $\delta^{18}O$ of foraminiferal calcite records from sediment cores contain both sea level and temperature variations. Although the $\delta^{18}O$ of foraminiferal calcite ($\delta^{18}O_{calcite}$) contains both temperature and ice volume variations (Epstein et al., 1953; Shakleton, 1967), some researchers still refer to a global stack of $\delta^{18}O_{calcite}$ (Lisiecki and Raymo, 2005) as a record of the pattern of eustatic sea level over the last 5 million years (Hughes et al. 2013; Murry-Wallace, 2018).

Data interpreted as a global signal also generally includes a variety of regional effects. Both regional and global signals are present in deep sea sediment records taken from different locations: for example, the $\delta^{18}O$ of Atlantic seawater is slightly more enriched (by

0.11 ‰) than the Pacific because of differences in precipitation and seawater exchange between the two oceans (LeGrande and Schmidt, 2006). The low-latitude surface ocean tends to be enriched in $\delta^{18}O_{sw}$ as heavy isotopes become locally enriched in seawater where evaporation exceeds precipitation. The Mediterranean and the Red Sea are both more enriched than the Atlantic because of intense evaporation in these semi-isolated locations.

Despite varying regional effects, several individual records of eustatic sea level exist which are derived from cores from the Atlantic (Sosdian and Rosenthal, 2009), the Pacific (Elderfield, 2012), the Red Sea (Rohling et al., 2009) and the Mediteranean (Rohling et al., 2013). When graphed together (Fig.1, Ch 2), these records show similar variations over the last several climate cycles; it is evident that they share a common global signal. Combining these records into a single record of sea level shows more clearly changes in global sea level than individual records of sea level derived from single geographic locations. In addition, I present here an in-depth study of three areas in the Atlantic Ocean, to investigate ocean and atmospheric circulation changes that contribute to differences in these sea level datasets.

Thus, this dissertation explores $\delta^{18}O_{sw}$ variations temporally and spatially with data and then with models.

The first study of this project explores the common temporal variation of climate expressed in sea level records derived from $\delta^{18}O_{calcite}$ over the last 800,000 years. The sediment core data is derived from $\delta^{18}O_{calcite}$ and other methods for at least the last 4-8 glacial cycles (Sosdian and Rosenthal, 2009; Elderfield, 2012; Waelbroeck, 2002; Rohling et al., 2009; Rohling et al., 2013; Bintanja, 2005; Shakun et al., 2014). Five records comprise the longer sea level stack, and seven short records comprise the shorter sea level stack. The root mean square error (RMSE) estimate of sea level goes up as the number of combined records gets fewer). All records were either on or were converted to the age model of a stack of $\delta^{18}O$ of benthic foraminiferal calcite (Lisiecki and Raymo, 2005). The most recent 50 ka of sea level variability are better constrained than the records from 50 to 800 ka for two reasons: accurate coral sea level records for which U/Th can be used for sea level are not prevalent beyond 30 ka, though they do exist to 150 ka (Medina-Elizalde,

2013). Records of the $\delta^{18}O_{sw}$ tied to coral benchmarks and age proxies are therefore more accurate when younger.

Individual records of sea level can be combined into a single record of eustatic sea level either by averaging them together, or by utilizing a statistical tool called Principal Components Analysis (PCA). PCA is a useful tool because records may be combined whether or not they were developed with independent methods from one another. The combined sea level record in this study contains data created from several regional $\delta^{18}O$ calcite stacks. The hypothesis of this study is that the first Principal Component or PC1 will represent common sea level change signal shared by the individual records.

Although climate states of warm and cold periods have varied on approximately 100,000 year cycles for the last million years, most recently the warmest and coldest periods occurred during the last 20,000 years, the modern/Holocene and Last Glacial Maximum (LGM), respectively. During these climate extremes one can study the regional changes in $\delta^{18}O_{seawater}$ to understand the changes in climate.

Studies have attempted to understand both regional and temporal variation of Atlantic meridional overturning flux between the LGM and the modern/Holocene using multiple techniques; proxies such as ƐNd (epsilon-Neodymium) indicate a slightly shallower North Atlantic water mass by ~ 200 m in the Atlantic at the LGM than the Holocene (Gutjahr, 2008). Studies examining rates of overturning flux use Pa/Th (Protactinium-Thorium) proxies have suggested a concurrently slower flux rate of 30% of modern (Mcmanus, 2004). Reanalyses of these datasets however, indicate a possible scavenging of Protactinium in the surface ocean by primary producers such as diatoms, thereby altering Pa/Th ratios in a way that makes overturning appear slower (Lynch-Stieglitz et al., 2007).

Attempts by complex climate models to resolve flux rates at the LGM have led to differing results, including both faster and slower models of Atlantic ocean circulation than the present day. This leaves room for debate and study about past ocean dynamics. Because the drivers of cause and effect can be difficult to discern in complex models, the second and third part of this study use a simple box model to infer the effects of vapor transport and

seawater mixing rates on $\delta^{18}O_{sw}$ values in ocean basins. Mix (1992) provides a box model template with a study of Atlantic gradients in $\delta^{18}O_{sw}$ using a simple 3-box model; in the second part of this study, I apply recent literature flux estimates to a similar 3-box model. A preliminary model is tuned to $\delta^{18}O_{sw}$ in the modern ocean (LeGrande and Schmidt, 2006) followed by a slightly more complex model with more realistic Rayleigh fractionation in the atmosphere.

In the third part of this study, the more complex box model is used to evaluate recent paleoclimate literature estimates that Atlantic overturning was slower at the LGM. A multi-model mean of 3 models from the Paleoclimate Model Intercomparison Project 3 (PMIP3) provides estimates of the low-latitude temperature of evaporation, low-latitude evaporative flux and fraction of vapor transport across 50° N in this model. Results of the LGM and Holocene runs are compared to a dataset compiled by Waelbroeck et al., (2014) of the change in the $\delta^{18}O_{sw}$ of the surface ocean between the LGM and Holocene and to deep ocean $\delta^{18}O_{sw}$ change (Adkins and Schrag, 2002). Sensitivity tests are used to explore the

effects of each model parameter on the surface (horizontal) gradient and surface-to-deep (vertical) gradient between the Holocene and the LGM.

The goal of the first study in this project is to create a strong record of global sea level over the past 800,000 years by identifying the common signal in 5-7 records of eustatic sea level derived with differing methods, but based on records of the $\delta^{18}O$ of foraminiferal calcite. The second goal of this project is to better constrain the regional changes in the $\delta^{18}O$ of foraminiferal calcite between two climate extremes: the (cold) Last Glacial Maximum (LGM) 20,000 years ago and the (warm) Holocene to present day (4ka to 0 ka).

II A Late Pleistocene Sea Level Stack

1 Introduction

Late Pleistocene sea level has been reconstructed from ocean sediment core data using a wide variety of proxies and models. However, the accuracy of individual reconstructions is limited by measurement error, local variations in salinity and temperature, and assumptions particular to each technique. Here we present a sea level stack (average) which increases the signal-to-noise ratio of individual reconstructions. Specifically, we perform principal component analysis (PCA) on seven records from 0-430 ka and five records from 0-798 ka. The first principal component, which we use as the stack, describes ~80% of the variance in the data and is similar using either five or seven records. After scaling the stack based on Holocene and Last Glacial Maximum (LGM) sea level estimates, the stack agrees to within 5 m with isostatically adjusted coral sea level estimates for Marine Isotope Stages 5e and 11 (125 and 400 ka, respectively). Bootstrapping and random sampling yield mean uncertainty estimates of 9-12 m (1σ) for the scaled stack. Sea level change accounts for about 45% of the total orbital-band variance in benthic $\delta^{18}O$, compared to a 65% contribution during the LGM-to-Holocene transition. Additionally, the second and third principal components of our

analyses reflect differences between proxy records associated with spatial variations in the $\delta^{18}O$ of seawater.

Glacial-interglacial cycles of the Late Pleistocene (0-800 ka) produced sea level changes of approximately 130 meters, primarily associated with the growth and retreat of continental ice sheets in 100-ka cycles. Recent ice sheet modeling studies support the assertion of Milankovitch theory that Late Pleistocene glacial cycles are primarily driven by insolation changes associated with Earth's orbital cycles (Ganopolski and Calov, 2011; Abe-Ouchi et al. 2013). However, modeling ice sheet responses over orbital timescales remains quite challenging, and the output of such models should be evaluated using precise and accurate reconstructions of sea level change. Thus, Late Pleistocene sea level reconstructions are important both for understanding the mechanisms responsible for 100-ka glacial cycles and for quantifying the amplitude and rate of ice sheet responses to climate change. Sea level estimates for warm interglacials at 125 and 400 ka are also of particular interest as potential analogs for future sea level rise (Kopp et al., 2009; Raymo and Mitrovica, 2012; Dutton et al., 2015).

Nearly continuous coral elevation data have generated well-constrained sea level reconstructions since the Last Glacial Maximum (LGM) at 21 ka (Clark et al., 2009;

Lambeck et al., 2014). However, beyond the LGM sea level estimates from corals are discontinuous and have relatively large age uncertainties (e.g., Thompson and Goldstein, 2005; Medina-Elizalde, 2013). Several techniques have been developed to generate longer continuous sea level reconstructions from marine sediment core data. Each of these techniques is subject to different assumptions and regional influences. Here, we identify the common signal present in seven Late Pleistocene sea level records as well as some of their differences.

These sediment core records convert $\delta^{18}O_c$, the oxygen isotope content of the calcite tests of foraminifera, to sea level using one of several techniques. In three records, temperature proxies were used to remove the temperature-dependent fractionation effect from $\delta^{18}O_c$ in order to solve for the $\delta^{18}O$ of seawater ($\delta^{18}O_{sw}$). Other techniques for transforming $\delta^{18}O_c$ to sea level include the polynomial regression of $\delta^{18}O_c$ to coral-based sea level estimates, hydraulic control models of semi-isolated basins, and inverse models of ice volume and temperature. Each of these techniques produce slightly different results for a variety of reasons. For example, $\delta^{18}O_{sw}$ varies spatially due to differences in water mass salinity and deep water formation processes (Adkins et al., 2002). Reconstructions also vary based on sensitivity to eustatic versus relative sea level (RSL) and temporal resolution.

Principal component analysis (PCA) is used to identify the common sea level signal in these seven records (i.e., to produce a sea level "stack") and to evaluate differences between reconstruction techniques. By combining multiple sea level records with different underlying assumptions and sources of noise, the sea level stack should have a higher signal-to-noise ratio than the individual sea level records used to construct it. We estimate the uncertainty of the sea level stack using bootstrapping and Monte Carlo-style random sampling. For comparison, we also report the standard deviation of highstand and lowstan estimates across individual records and the sea level uncertainties of individual records as estimated in their original publications. A probabilistic reassessment of the uncertainties in individual records is beyond the scope of the current study.

2 Sea level reconstruction techniques

2.1 Corals and other coastal sea level proxies

Corals provide the most prominent Late Pleistocene sea level proxy. They can be radiometrically dated and provide especially accurate sea level estimates between 0-21 ka because of nearly continuous pristine coral specimens from several locations (Fairbanks, 1989; Bard et al., 1990; Edwards et al., 1993; Bard et al., 1996). Dated coral sea level estimates extend as far back as ~600 ka (Stein et al., 1993; Stirling et al., 1995; Medina-Elizalde, 2013; Muhs et al., 2014; Andersen et al., 2008). However, coral data are increasingly discontinuous and inaccurate prior to 21 ka due to difficulty finding pristine and in situ older corals (particularly during sea level lowstands) and due to U-Th age uncertainties in older corals caused by isotope free exchange with the surrounding environment (e.g., Thompson and Goldstein, 2005; Blanchon et al., 2009; Medina-Elizalde, 2013). Interpretation of sea level from corals often requires a correction for rates of continental uplift, which may not be known precisely (Creveling et al., 2015). Glacial isostatic adjustment (GIA) and species habitat depth (up to 6 m below sea level) may also affect sea level estimates (Raymo and Mitrovica, 2012; Medina-Elizalde, 2013). Wave destruction and climate variations also alter coral growth patterns and may affect the height

of colonies relative to sea level (Blanchon et al., 2009; Medina-Elizalde, 2013. Organic proxies such as peat bogs and shell beds can also be used as sea level proxies and can be radiometrically dated (e.g., Horton, 2006). Geological formations indicating sea level such as abandoned beaches and sea cliffs can also be used as sea level proxies (Hanebuth et al., 2000; Boak and Turner, 2005; Bowen, 2010).

Corals and other coastal proxies are indicators of relative (local) sea level and, thus, are affected by in situ glacio-isostatic effects, ocean siphoning processes, and other local effects of sea level rise and fall. However, their wide spatial distribution, particularly corals in tropical regions, allows for modeling of glacioi-sostatic adjustments (GIA) to create a global estimate of mean sea level change (e.g., Kopp et al., 2009; Lambeck et al., 2014; Dutton and Lambeck, 2012; Hay et al., 2014). GIA models constrained by these coastal indicators provide robust sea level change estimates of -130 to -134 m 7for the LGM (Clark et al., 2009; Lambeck et al., 2014). A compilation of dozens of corals and other sea level indicators also provides a relatively well-constrained estimate of 8.7 ± 0.7 m for peak global mean sea level at the last interglacial (Kopp et al., 2009). Estimates from multiple studies using different data are all in relatively good agreement yielding a consensus estimate of 6 to 9 m above modern (Dutton et al., 2015). Additionally, sea level during the last interglacial likely

experienced several meters of millennial-scale variability (Kopp et al., 2013; Govin et al., 2012). Uncertainties increase for older interglacials. GIA-corrected coastal sea level proxies for Marine Isotope Stage (MIS) 11 at ~400 ka suggest a global mean sea level of 6-13 m above modern (Raymo and Mitrovica, 2012).

2.2 Seawater $\delta^{18}O$

Global ice volume is a main control on the global mean of $\delta^{18}O$ in seawater ($\delta^{18}O_{sw}$), with global mean $\delta^{18}O_{sw}$ estimated to decrease by 0.008‰ to 0.01‰ per meter of sea level rise (Adkins et al., 2002; Elderfield 2012; Shakun et al., 2015). However, $\delta^{18}O_{sw}$ also varies spatially based on patterns of evaporation and precipitation and deep water formation processes. The $\delta^{18}O$ of calcite ($\delta^{18}O_c$) is affected both by the $\delta^{18}O_{sw}$ and temperature. In the absence of any post-depositional alteration, subtracting the temperature-dependent fractionation effect from $\delta^{18}O_c$ (Shackleton, 1974) should yield a good estimate of the $\delta^{18}O_{sw}$ in which the calcite formed. Pioneering studies for estimating time series of $\delta^{18}O_{sw}$ using independent measures of temperature include Dwyer et al. (1995), Martin et al. (2002), and Lea et al. (2002). Dwyer et al. (1995) used ostracod Mg/Ca ratios to determine temperature whereas Martin et al (2002) and Lea et al (2002) used benthic and planktonic foraminifera,

respectively. The $\delta^{18}O_c$ of benthic foraminifera reflects the temperature and $\delta^{18}O_{sw}$ of deep water, while the $\delta^{18}O_c$ of planktonic foraminifera is affected by sea surface temperature (SST) and the $\delta^{18}O_{sw}$ of near-surface water.

2.3 Benthic $\delta^{18}O_{sw}$

Our analysis includes two benthic $\delta^{18}O_{sw}$ records from the North Atlantic and South Pacific, which use the Mg/Ca ratio of benthic foraminifera as a temperature proxy. The South Pacific benthic $\delta^{18}O_{sw}$ record (Elderfield et al., 2012) from Ocean Drilling Program (ODP) site 1123 (171 W, 41 S, 3290 m) reflects the properties of Lower Circumpolar Deep Water, which is a mix of Antarctic Bottom Water (AABW) and North Atlantic Deep Water (NADW). Mg/Ca ratios and $\delta^{18}O_c$ were determined from separate samples of the same species of *Uvigerina,* which is considered fairly insensitive to the deep water carbonate saturation state (Elderfield et al., 2012). Elderfield et al. (2012) interpolate their data to 1 ka spacing, perform a 5-ka Gaussian smoothing, and convert from $\delta^{18}O_{sw}$ to sea level using a factor of $0.01‰m^{-1}$. Elderfield et al. (2012) report measurement uncertainties for temperature and $\delta^{18}O_c$ generate a $\delta^{18}O_{sw}$ uncertainty of ±0.2‰, corresponding to bottom water temperature range of ±1°C or about 22 m of sea level.

The North Atlantic $\delta^{18}O_{sw}$ reconstruction is from Deep Sea Drilling Program (DSDP) site 607 (32 W, 41 N, 3427 m) and nearby piston core Chain 82-24-23PC (Sosdian and Rosenthal, 2009). These sites are bathed by NADW today but were likely influenced by AABW during glacial maxima (Raymo et al., 1990). Mg/Ca was measured using two benthic foraminiferal species, *Cibicidoides wuellerstorfi* and *Oridorsalis umbonatus,* which may be affected by changes in carbonate ion saturation state, particularly when deep water temperature drops below 3°C (Sosdian and Rosenthal, 2009). The $\delta^{18}O_c$ data come from a combination of *Cibicidoides* and *Uvigerina* species. Sea level was estimated from benthic $\delta^{18}O_{sw}$ using a conversion of 0.01‰m^{-1} and then taking a 3-point running mean. Combining the uncertainties for temperature (±1.1°C) and $\delta^{18}O_c$ (±0.2‰) reported by Sosdian and Rosenthal (2009) yields a sea level uncertainty of approximately ±20 m (one standard error) for the 3-point running mean.

2.4 Planktonic $\delta^{18}O_{sw}$

A 49-core global stack uses the $\delta^{18}O_c$ from planktonic foraminifera paired with SST proxies from the same core. The planktonic species in this reconstruction were: *G. ruber*, *G. bulloides*, *G. inflata*, *G. sacculifer*, *N. dutretriei*, and *N. pachyderma*. Forty-four records span

the most recent glacial cycle, and seven records extend back to 798 ka. Thirty-four records use Mg/Ca temperature estimates, and fifteen use the alkenone $U^{k'}_{37}$ temperature proxy. Because $U^{k'}_{37}$ measurements derive from coccolithophore rather than foraminifera, there is some chance the temperature measured may differ slightly from that affecting $\delta^{18}O_c$ (Schiebel et al. 2004). However, Shakun et al. (2015) observed no significant differences in $\delta^{18}O_{sw}$ estimated from the two SST proxies. An additional concern is that the surface ocean is affected by greater hydrologic variability and characterizes a smaller ocean volume than the deep ocean. Thus, planktonic $\delta^{18}O_{sw}$ may differ more from ice volume changes than benthic data. However, these potential disadvantages of using planktonic records may be largely compensated by the use of a global planktonic stack.

The first principal component (stack) of the planktonic records spanning the last glacial cycle represents 71% of the variance in the records (n=44), suggesting a strong common signal in planktonic $\delta^{18}O_{sw}$. However, the 800-ka planktonic $\delta^{18}O_{sw}$ stack appears to contain linear trends that differ from other sea level estimates. Therefore, Shakun et al. (2015) corrected their sea level estimate by detrending planktonic $\delta^{18}O_{sw}$ based on differences between planktonic and benthic $\delta^{18}O_c$. Standard errors reported by Shakun et al. (2015) for the $\delta^{18}O_{sw}$ stack increased from 0.05‰ for the last glacial cycle to 0.12‰ at 800 ka due to

the reduction in the number of records. The equivalent sea level uncertainties are ±6 m and ±18 m (1σ), respectively. All data were interpolated to even 3 ka time intervals.

2.5 Benthic $\delta^{18}O_c$ - coral regression

The sea level reconstruction of Waelbroeck et al. (2002) was developed by fitting polynomial regressions between benthic $\delta^{18}O_c$ from North Atlantic cores NA 87-22/25 (55 N, 15 W, 2161 and 2320 m) and equatorial Pacific core V19-30 (3 S, 83 W, 3091 m) to sea level estimates for the last glacial cycle, primarily from corals. Quadratic polynomials were fit during times of ice sheet growth and during the glacial termination in the North Atlantic whereas a linear regression was fit to the Pacific glacial termination. A composite sea level curve was created from the most reliable sections of several cores, primarily from the Pacific. Waelbroeck et al. (2002) interpolated the composite time series to an even 1.5 ka time window and estimated the uncertainty associated with this technique to be ±13 m of sea level. Transfer functions between benthic $\delta^{18}O_c$ and coral sea level estimates have also been estimated at lower resolution and applied to 10 different benthic $\delta^{18}O$ records spanning 0-5 Ma (Siddall et al., 2010; Bates et al., 2014).

2.6 Inverse ice volume model

The inverse model of Bintanja et al. (2005) is based on the concept that Northern Hemisphere (NH) subpolar surface air temperature plays a key role in determining both ice sheet size and deepwater temperature, which are the two dominant factors affecting benthic $\delta^{18}O_c$. A three-dimensional thermomechanical ice sheet model simulates ice sheet $\delta^{18}O$ content, height, and volume for NH ice sheets (excluding Greenland) as forced by subpolar air temperature, orbital insolation, and the modern spatial distributions of temperature and precipitation. Antarctic and Greenland ice sheets are assumed to account for 5% of ocean isotopic change and 15% of sea level change. Deep water temperature is assumed to scale linearly with the 3-ka mean air temperature. At each time step air temperature is adjusted to maximize agreement between predicted $\delta^{18}O_c$ and the observed value 0.1 ka later in a benthic $\delta^{18}O_c$ stack (Lisiecki and Raymo, 2005). The model solves for ice volume, temperature, and sea level changes since 1070 ka in 0.1 ka time steps; however, the $\delta^{18}O_c$ stack used to constrain the model has a resolution of 1-1.5 ka. Bintanja et al. (2005) report the uncertainty of their sea level model to be approximately ±12 m (1σ).

2.7 Hydraulic control models of semi-isolated basins

Two sea level reconstructions use hydraulic control models to relate planktonic $\delta^{18}O_c$ from the Red Sea and Mediterranean Sea to relative sea level. In these semi-isolated basins, $\delta^{18}O_{sw}$ is strongly affected by evaporation and exchange with the open ocean as affected by relative sea level at the basin's sill.

Red Sea RSL (Rohling et al., 2009) from 0-520 ka is estimated using the $\delta^{18}O_c$ of planktonic foraminifera from the central Red Sea (GeoTü-KL09). Because extremely saline conditions killed foraminifera during MIS 2 and MIS 12, $\delta^{18}O_c$ data for these time intervals were estimated by transforming bulk sediment values. Sea level is estimated using a physical circulation model for the Red Sea combined with an oxygen isotope model (Siddall et al., 2004). The physical circulation model simulates exchange flow through the Bab-el-Mondab strait which depends strongly on sea level. The current sill depth is 137 m, and its estimated uplift rate is 0.2 m ka^{-1}. The isotope model assumes steady state with exchange through the sill and evaporation/precipitation. Assumptions of the isotope model include: (1) modern evaporation rates and humidity, (2) open ocean $\delta^{18}O_{sw}$ scales as 0.01‰m^{-1}, and (3) SST scales linearly with sea level. A 5° C change in SST between Holocene and LGM is used to optimize the model's LGM sea level estimate. Steady state model solutions for different sea

level estimates are used to develop a conversion between $\delta^{18}O_c$ and sea level, which is approximated as a fifth-order polynomial. Rohling et al. (2009) performed sensitivity tests using plausible ranges of climatic values to produce a 2-σ uncertainty estimate of ± 12 m.

A Mediterranean RSL record (Rohling et al., 2014) is derived from a hydraulic model of flow through the Strait of Gibraltar (Bryden and Kinder, 1991) combined with evaporation and oxygen isotope fractionation equations for the Mediterranean (Siddall et al., 2004). Runoff and precipitation are parameterized based on present-day observations, humidity is assumed constant, and temperature is assumed to covary with sea level. The $\delta^{18}O_{sw}$ of Atlantic inflow is scaled using $0.009‰m^{-1}$, and net heat flow through the sill is assumed to be zero. The combined models yield a converter between $\delta^{18}O_c$ and sea level, which is approximated as a polynomial. This polynomial conversion is applied to an eastern Mediterranean planktonic $\delta^{18}O_c$ stack (Wang et al., 2010) after identification and removal of sapropel layers. Model uncertainty is evaluated using random parameter variations, which yield 95% confidence intervals of ±20 m for individual $\delta^{18}O_c$ values. By performing a probabilistic assessment of the final sea level reconstruction with 1-ka time steps, Rohling et al. (2014) estimate that these uncertainties are reduced to ±6.3 m. Additionally, the authors propose that RSL at this location is linearly proportional to eustatic sea level.

3 Methods

3.1 Record inclusion criteria

The criteria for record inclusion in our stack were availability, a temporal resolution of at least 5 ka, and a length of at least 430 ka. The five records which extended to 798 ka were also included in a longer stack. Some available records were too short for inclusion (e.g., Dwyer et al., 1995; Martin et al, 2002; Lea et al., 2002). The record of Siddall et al (2010) was not included because it was based on the same technique as Waelbroeck et al (2002) but with lower resolution. Bates et al (2014) extended this technique to many benthic $\delta^{18}O$ records but advocated against placing them all on a common age model; therefore, we include a summary of that study's lowstand and highstand estimates in Table 2 rather than aligning them for inclusion in the stack.

3.2 Age models

To create an average (or stack) of sea level records, all of the time series must be placed on a common age model (Fig. 1). Here we use the age model of the orbitally tuned "LR04" benthic $\delta^{18}O_c$ stack (Lisiecki and Raymo, 2005), which has an uncertainty of 4 ka in the Late Pleistocene. An age model for the Red Sea reconstruction based on correlation to

speleothems is generally similar to LR04 with smaller age uncertainty but only extends to 500 ka (Grant et al., 2014) and, thus, does not provide an age framework for the entire 798 ka stack. Due to age model uncertainty, our interpretation focuses on the amplitude of sea level variability rather than its precise timing.

We do not assume that sea level varies synchronously with benthic $\delta^{18}O_c$. Age models for three of the reconstructions are based on aligning individual $\delta^{18}O_c$ records to the LR04 $\delta^{18}O_c$ stack, and one reconstruction (Bintanja et al., 2005) was derived directly from the LR04 stack. The other three sea level reconstructions were dated by aligning their sea level estimates to a preliminary stack of the four sea level records that were dated using $\delta^{18}O_c$ alignments. Alignments were performed using the Match graphic correlation software package (Lisiecki and Lisiecki, 2002).

The three records which use $\delta^{18}O_c$ alignments to the LR04 stack are Sites 607, 1123, and the planktonic $\delta^{18}O_{sw}$ stack. For Site 607 we perform our own alignment of benthic $\delta^{18}O_c$ to the LR04 stack, whereas for the other two we use the same age models published by Elderfield et al. (2012) and Shakun et al (2015). One potential concern about aligning benthic $\delta^{18}O_c$ records is that the timing of benthic $\delta^{18}O_c$ change at different sites may differ by as much as 4 kyr during glacial terminations (Skinner and Shackleton, 2005; Lisiecki and

Raymo, 2009; Stern and Lisiecki, 2014). The potential effects of lags in benthic $\delta^{18}O_c$ are evaluated using bootstrap uncertainty analysis (Section 4.2).

For three reconstructions (Waelbroeck et al., 2002; Rohling et al., 2009, 2014) we aligned the individual sea level records with a preliminary sea level stack based on the other four sea level records on the LR04 age model. This was necessary because the local $\delta^{18}O_c$ signals in semi-isolated basins (Rohling et al., 2009; 2014) differ substantially from global mean benthic $\delta^{18}O_c$. In the coral-regression reconstruction, Waelbroeck et al. (2002) pasted together portions of individual cores to form a preferred global composite. Although each core has benthic $\delta^{18}O_c$ data, generating new age estimates for these cores could alter their $\delta^{18}O_c$ regression functions or create gaps or inconsistencies in the composite. The procedure of aligning these three sea level records (Waelbroeck et al, 2002; Rohling et al., 2009, 2014) to a preliminary sea level stack should be approximately as accurate as the $\delta^{18}O_c$ alignments. However, the direct sea level alignments do have a slightly greater potential to align noise or local sea level variability.

After age models were adjusted, five of the records ended within the Holocene. Therefore, we appended a value of 0 m (i.e., present day sea level) at 0 ka. In the two records

which did end at 0 ka, modern sea level estimates were slightly below zero: -1.5 m (Bintanja, 2005) and -1.3 m (Rohling et al., 2014).

3.3 Principal component analysis

Principal Component Analysis (PCA) is commonly used to create stacks of paleoclimate data (e.g., Huybers and Wunsch, 2004; Clark et al, 2012; Gibbons et al, 2014) and to quantify the common signal contained in core data. Synthesis is valuable because each record has its own assumptions and errors. If these records are all well-constrained measures of sea level, then PCA will reveal their respective levels of agreement or discrepancy. Additionally, PCA does not require the assumption that each sea level record represents an independent measure of common signal. In contrast, a sea level estimate based on the unweighted mean of records would imply that uncertainties are uncorrelated across individual reconstructions. While all records contain a strong ice volume signal, some of the non-ice volume signals are expected to correlate with one another. For example, as the $\delta^{18}O$ of ice sheet changes as it melts or freezes, the conversion from the $\delta^{18}O_{sw}$ to ice volume will be systematically biased, whereas changes in the hydrological cycle may induce changes in the spatial variability of $\delta^{18}O_{sw}$ at different locations in the ocean.

We include both relative and eustatic sea level estimates in the analysis because PCA should identify the common variance that dominates both relative and eustatic sea level records. Three records are proxies for relative sea level at their respective locations: the strait of Gibraltar (Rohling et al., 2014), the Bab el Mondab strait (Rohling et al., 2009), and tropical coral terraces (Waelbroeck et al., 2002). The inverse model generates eustatic sea level from a modeled ice volume estimate (Bintanja et al., 2005), and the three $\delta^{18}O_{sw}$ records (Elderfield et al., 2012; Sosdian and Rosenthal, 2009; Shakun et al., 2015) were scaled to eustatic sea level. However, for the planktonic stack we use the $\delta^{18}O_{sw}$ record rather than the eustatic sea level conversion because the sea level conversion involved detrending to make planktonic $\delta^{18}O_c$ values agree with benthic $\delta^{18}O_c$. Because PCA is designed to identify the common variance between the sea level proxies, it is preferable to keep the planktonic and benthic $\delta^{18}O_{sw}$ records independent of one another.

In the Mediterranean RSL record we removed putative sapropel layers at 434-452 ka, 543-558 ka, and 630-663 ka as visually identified by Rohling et al. (2014). Because interpolating linearly across these gaps (Fig. 1) would bias sea level estimates towards higher lowstands for the glacial maxima occurring during these sapropel layers, we assumed that sea level remained constant at its pre-sapropel (glacial) level and then immediately

jumped to the higher sea level values observed the ends of the sapropel layers (midway through the glacial terminations). Although this solution is not ideal, we must assume some sea level value at these times in order to include this record in the PCA.

Before PCA all seven records were interpolated to an even 1-ka time step. Then, to ensure equal weighting for each record in the PCA, each time series was normalized to a mean of zero and a standard deviation of one within each of the two time windows (0-430 ka and 0-798 ka). PCA was performed on seven records from 0-430 ka and five records from 0-798 ka (Fig. 2). Because PC1 produces similar loadings for each record (Table 1), the PC1 scores approximate the average of all records for each point in time, which we refer to as a sea level stack.

We scaled the short and long stacks to eustatic sea level using an LGM value of -130 m at 24 ka based on a GIA-corrected coral compilation (Clark et al., 2009) and a Holocene value of 0 m at 5 ka. We scale the Holocene at 5 ka because eustatic sea level has been essentially constant for the past 5 ka (Clark et al., 2009), whereas the sea level stacks display a trend throughout the Holocene perhaps due to bioturbation in the sediment cores. Scaling the sea level stack based on the mid-Holocene (rather than 0 ka) should more accurately correct for the effects of bioturbation on previous interglacials because those highstand

values have been subjected to mixing from both above and below. Finally, a composite sea level stack was created by joining the 0-430 ka stack with the 431-798 ka portion of the long stack after each was scaled to sea level. Because the two scaled sea level stacks produce similar values for 0-430 ka (Fig. 2), no correction was needed to combine the records.

4 Uncertainty analysis

Because each of the records in the PCA is a sea level proxy and PC1 describes the majority of variance in the records, PC1 should represent the underlying common eustatic sea level signal in all proxies. PC1 describes 82% of the variance in the seven records from 0-430 ka and 76% of proxy variance from 0-798 ka. Where the two time windows overlap (Figure 2), the scaled sea level stacks have a root mean square error of only 3.4 m, thereby suggesting that the long stack is nearly as accurate as the short stack although it contains two fewer records. We assess the uncertainty of the scaled PC1 using multiple techniques: comparison with highstand and lowstand estimates from individual records (Section 4.1), comparison with the unweighted mean of all records (Section 4.1), and using bootstrapping and Monte Carlo-style random sampling (Section 4.2).

4.1 Mean sea level estimates

To test the effectiveness of using the scaled PC1 as a record of mean sea level, we compared our stack with highstand and lowstand values identified from individual records and with coral-based estimates where available (Tables 2 and 3). We picked the relevant highstand or lowstand for each individual record by choosing the peak that lies within the age range of each Marine Isotope Stage (MIS) as identified in the sea level stack. Highstand or lowstand peaks which occurred outside of the age range of each particular glacial or interglacial stage were not used (e.g., extreme values at ~250 ka from ODP Sites 1123 and 607).

Highstand sea level estimates vary widely between individual records with standard deviations of 11-26 m for each isotopic stage (Table 3). For example, individual estimates for MIS 11 at ~400 ka vary between -5 to 57 m above modern, with a mean of 18 m and a standard deviation of 25 m. MIS 5e (119-126 ka) estimates range from -4 to 28 m above modern with a mean of 7 m and a standard deviation of 12 m. Generally, the highstand means have slightly greater amplitudes than our scaled stack; for example, the scaled stack estimates are 18 m and 7 m for MIS 11 and MIS 5e, respectively. On the other hand, the

mean of individual lowstands for the LGM (-123 m) underestimates eustatic sea level change, which is estimated to be -130 to -134 m (Clark et al, 2009; Lambeck et al., 2014).

The means of the individually picked highstands may be biased by the additive effects of noise. Conversely, the stack may underestimate sea level highstands if the individual age models are not properly aligned. The most definitive sea level estimates come from GIA-corrected coral compilations, which yield highstand estimates of 6-13 m above modern for MIS 11 (Raymo and Mitrovica, 2012) and 8-9.4 m for MIS 5e (Kopp et al., 2009). These values suggest that the stack may be more accurate for MIS 11 than MIS 5e, potentially because age model uncertainty would have less effect on the longer MIS 11 highstand. In contrast, MIS 5e may have consisted of two highstands each lasting only ~2 ka separated by several thousand years with sea level at or below modern (Kopp et al., 2013). Thus, the stack's highstand estimates likely fail to capture short-term sea level fluctuations but rather reflect mean sea level during each interglacial.

To further test the sensitivity of our method, we compared the scaled PC1 with the unweighted mean of the seven interpolated sea level records (Figure 2b). The unweighted-mean stack incorporates the same data as scaled PC1 except that it excludes Mediterranean estimates from sapropel intervals and uses the detrended sea level estimates

from Shakun et al. (2015) instead of the raw $\delta^{18}O_{sw}$ data. The unweighted stack closely resembles PC1 because the loadings of PC1 are very similar for all seven records (Table 1). However, the unweighted stack underestimates LGM sea level, possibly because some records (e.g., Rohling et al, 2009) may contain brief gaps at the glacial maximum. Thus, we prefer to scale PC1 to agree with well-constrained LGM sea level estimates. The scaled PC1 is in better agreement with the glacial sea level estimates of the unweighted five-record stack from 430-798 ka.

4.2 Bootstrapping and random sampling

We estimate uncertainty in the stack using a bootstrap technique instead of using the published uncertainty estimates for each sea level reconstruction, which are based on different assumptions and techniques and do not necessarily include all sources of uncertainty (e.g., uncertainty in benthic $\delta^{18}O_c$ alignments). We ran 1000 bootstrap iterations while also performing random sampling to account for several of the uncertainties associated with our method. Before each iteration of the bootstrapped PCA, we simulate the effects of uncertainty associated with our age model alignments by applying an independent age shift of -2, -1, 0, +1, or +2 ka to each component record, with each potential value selected with

equal probability. After performing each iteration of the PCA, we use random sampling to evaluate the effects of uncertainty associated with scaling PC1 to Holocene and LGM sea level. The particular Holocene point scaled to 0 m is randomly sampled from 0 – 6 ka with uniform distribution. The LGM age is identified as the minimum sea level estimate between 19-34 ka, and the sea level to which it is scaled is sampled with a normal distribution centered at 132 m with a standard deviation of 2 m. The bootstrap results for the scaled PC1 yield a mean standard deviation of 9.4 m with seven records (0-430 ka) and 12 m with five records (0-798 ka). Additionally, the inclusion of age uncertainty in the bootstrap analysis has the effect of systematically smoothing the record. Because many of the individual reconstructions are of low resolution relative to brief interglacial highstands such as MIS 5e and 7e, the bootstrapped median is biased towards underestimating these highstands (Figure 2c). Therefore, in Table 3 we additionally describe the 95% confidence interval for sea level maxima and minima in the bootstrapped samples.

5 The sea level contribution to benthic $\delta^{18}O_c$

The sea level stack and the LR04 benthic $\delta^{18}O_c$ stack are strongly correlated (r = -0.90). However, because $\delta^{18}O_c$ contains both an ice volume and temperature component, the $\delta^{18}O_c$ record has a greater amplitude than the ice volume-driven $\delta^{18}O_{sw}$ record. The spectral variance of $\delta^{18}O_{sw}$ and $\delta^{18}O_c$ in each orbital band can be used to determine the relative contributions of sea level and temperature variability in $\delta^{18}O_c$. For this comparison, we convert the sea level stack to $\delta^{18}O_{sw}$ using 0.009‰ m^{-1}.

Although some studies have used 0.01‰m^{-1} (e.g., Sosdian et al., 2009; Elderfield et al., 2012; Rohling et al., 2009), this conversion factor is likely too high for global mean $\delta^{18}O_{sw}$ change at the LGM. Several lines of evidence suggest an LGM $\delta^{18}O_{sw}$ change of 1–1.1‰ (Duplessy et al., 2002; Adkins et al., 2002; Elderfield et al., 2012; Shakun et al., 2015), while LGM sea level was likely 125-134 m below modern (Clark et al., 2009; Lambeck et al., 2014; Rohling et al, 2014). These estimates suggest a conversion factor between 0.008-0.009‰m^{-1}. A conversion of 0.008‰m^{-1} would be consistent with a $\delta^{18}O_{ice}$ of -32‰ (Elderfield et al., 2012), similar to estimates for the Laurentide and Eurasian ice sheets (Duplessy et al., 2002; Bintanja et al., 2005; Elderfield et al., 2012). Therefore, 0.009‰m^{-1} may be more appropriate when also considering changes in Greenland and Antarctic ice.

However, the conversion factor between sea level and mean $\delta^{18}O_{sw}$ also likely varies through time as a result of changes in the mean isotopic content of each ice sheet (Bintanja et al, 2005) and their relative sizes.

Spectral analysis shows strong 100-ka and 41-ka peaks in both the LR04 benthic $\delta^{18}O_c$ stack and the sea level stack (Figure 3). When converted to $\delta^{18}O_{sw}$, the sea level stack contains 47% as much 100-ka power (0.009-0.013 ka^{-1} frequency band) as benthic $\delta^{18}O_c$ as benthic $\delta^{18}O_c$ and 37% as much 41-ka power (0.024-0.026 ka^{-1}). The bootstrapped PC1 samples described in Section 4.2 are used to estimate 95% confidence intervals (CI) of 31-65% and 22-54% for the relative power of $\delta^{18}O_{sw}$ in the 100-ka and 41-ka bands, respectively. Considering all frequencies less than 0.1 ka^{-1}, $\delta^{18}O_{sw}$ explains 44% (95% CI = 33-57%) of the variance in $\delta^{18}O_c$. Therefore, we estimate that on average about 45% of the glacial cycle variance in benthic $\delta^{18}O_c$ derives from ice volume change and 55% from deep sea temperature change.

This ~45% ice volume contribution to benthic $\delta^{18}O_c$ is smaller than the contribution estimated across the LGM to Holocene transition. An LGM sea level change of 130 m (Clark et al., 2009) should shift mean $\delta^{18}O_{sw}$ by 1.17‰, whereas benthic $\delta^{18}O_c$ changed by 1.79‰ (Lisiecki and Raymo, 2005), suggesting that 65% of the LGM $\delta^{18}O_c$ change was driven by

ice volume. Many other studies have similarly found that the ice volume ($\delta^{18}O_{sw}$) contribution to $\delta^{18}O_c$ is greatest during glacial maxima (Bintanja et al, 2005; Elderfield et al, 2012; Rohling et al., 2014; Shakun et al, 2015). Additionally, the $\delta^{18}O_{sw}$ contribution varies by location, ranging from 0.7‰ to 1.37‰ based on glacial pore water reconstructions (Adkins et al., 2002). The wide variability in $\delta^{18}O_{sw}$ between sites suggests that changes in deep water formation processes (e.g., evaporation versus brine rejection) greatly affect the $\delta^{18}O_{sw}$ signal regionally or locally. Therefore, the $\delta^{18}O_{sw}$ at a single site may differ considerably from eustatic sea level.

6 Converting from benthic $\delta^{18}O_c$ and sea level

Many studies have used benthic $\delta^{18}O_c$ as a proxy for ice volume based on the argument that temperature and ice volume should be highly correlated through time (e.g., Imbrie and Imbrie, 1980; Abe-Ouchi et al., 2013). However, calculations based on the sea level stack spectral power and LGM-to-Holocene change, suggest that ice volume change accounts for only 45-65% of benthic $\delta^{18}O_c$ glacial cyclicity Additionally, over the course of a glacial cycle the relative contributions of ice volume and temperature change dramatically, with temperature change preceding ice volume change (Bintanja et al., 2005; Elderfield et al.,

2012; Shakun et al., 2015). Despite these complications the LR04 benthic $\delta^{18}O_c$ stack is strongly correlated with the sea level stack (r = -0.9). Here we explore more closely the functional relationship between benthic $\delta^{18}O_c$ and sea level as inspired by Waelbroeck et al (2002).

Waelbroeck et al. (2002) solved for regression functions between several benthic $\delta^{18}O_c$ records and coral elevation data over the last glacial cycle and found different functional forms for glaciation versus deglaciation and for the North Atlantic versus equatorial Pacific $\delta^{18}O_c$. Here we compare the LR04 global benthic stack with the sea level stack from 0-798 ka. One advantage of this comparison is that both records use the same age model. We evaluate whether a single regression can be used for the Late Pleistocene and identify a potential change in the relationship between benthic $\delta^{18}O_c$ and sea level at ~400 ka.

One difference between the two stacks is that the sea level stack is smoother (Fig. 2), likely because some of the sea level records are low resolution and all records were interpolated to 1 ka spacing for PCA. Smoothing the LR04 stack using a 7-ka running mean improves the correlation between benthic $\delta^{18}O_c$ and sea level from -0.90 to -0.92. Additionally, we estimate the phase lag between the two records by measuring their correlation with different time shifts. This analysis suggests a 2 ka phase lag between LR04

and the sea level stack, likely resulting from the fact that deep water temperature change leads ice volume change (e.g., Sosdian and Rosenthal, 2009; Elderfield et al., 2012; Shakun et al., 2015). When we apply this 2 ka lag to the smoothed LR04 stack, its correlation with sea level improves to -0.94.

OLS linear regression between the smoothed-and-lagged LR04 benthic $\delta^{18}O_c$ stack (x) and sea level in meters (h) yields the equation

$$h = -73\ x + 251 \quad (1)$$

(Fig. 4, black line). Using the bootstrapped PC1 samples described in Section 4.2 and Monte Carlo-style sampling of smoothing windows that range from 0 – 7 kyr and lags from 0 – 3 kyr, we find that the 95% CI for the slope of this regression is -56 to -79 $m‰^{-1}$. The root mean square error (rmse) for this model is 10.7 m (95% CI = 9-22 m), but the fit is better for the older portion of the record (398-798 ka, rmse=10.2 m) than the more recent portion (0-397 ka, rmse=11.2 m). In particular, the linear model estimates sea levels that are 10-20 m too high during most highstands and lowstands back to MIS 10 at ~345 ka. The difference in fit before and after 398 ka is somewhat dependent upon the assumed lag between benthic $\delta^{18}O$ and sea level; the linear model fits the older portion of the record better in 84% of samples with a 3-ka lag but only 61% of sampled regressions with no lag. The

effect of a smaller lag is mainly to increase the rmse of the older portion of the linear regression from a mean of 12.7 m (3-ka lag) to 15.7 m (no lag).

A plot of sea level versus the smoothed and lagged benthic $\delta^{18}O_c$ (Figure 4b) suggests that the relationship between the two is approximately quadratic:

$$h = -26\ x^2 + 135\ x - 163 \qquad (2)$$

from 0 – 397 ka (rmse = 9.4 m, 95% CI = 8-22 m) and linear from 398-798 ka. This transition appears to take place between 360-400 ka because MIS 11 clearly falls on the linear trend whereas MIS 10 is much better fit by the quadratic (Figure 4a). Because this transition occurs after MIS 11, the extreme duration or warmth of this interglacial might have played an important role in the transition.

A change in the relationship between benthic $\delta^{18}O_c$ and sea level could be caused by a change in the mean isotopic content of ice sheets or the relationship between ice volume and deep water temperature (possibly also global surface temperature). Interglacials after MIS 11 were likely warmer or had more depleted $\delta^{18}O_{sw}$ relative to ice volume. Similarly, glacial maxima were probably warmer and/or had less $\delta^{18}O_{sw}$ change. Combined changes in temperature and isotopic fractionation may be the most likely explanation since warmer ice sheets also probably have less depleted $\delta^{18}O_{ice}$. In fact Antarctic ice cores are isotopically less

depleted during MIS 5e and MIS 9 than MIS 11 (Jouzel et al., 2010). Additionally, Antarctic surface temperatures and CO_2 levels were similar for all three interglacials (Masson-Delmotte et al., 2010; Petit et al., 1999) despite the smaller ice volume during MIS 11.

There is little direct evidence to explain the changing relationship between $\delta^{18}O_c$ and sea level during glacial maxima because glacial values for both deep water temperature and the isotopic composition of Antarctic ice are similar throughout the last 800 ka (Elderfield et al., 2012; Masson-Delmotte et al., 2010). The change in glacial maxima after 400 ka could be caused by less depleted $\delta^{18}O_{ice}$ in Northern Hemisphere (NH) ice sheets. Although no long records of NH $\delta^{18}O_{ice}$ exist, global mean SST was 0.5-1^{o}C warmer during MIS 2, 6, and 8 than during MIS 12 (Shakun et al., 2015). Alternatively, the apparent linear trend between sea level and $\delta^{18}O_c$ during glacial maxima before 400 ka (Figure 4c) could be an artifact of poor sea level estimates for MIS 12 and 16, which may be biased 10-20 m too high (Table 3) by missing data during sapropel intervals in the Mediterranean RSL record (Rohling et al., 2014).

In conclusion, a systematic relationship can be defined between Late Pleistocene benthic $\delta^{18}O_c$ and sea level, and the functional form of this relationship likely changed after MIS 11.

Change in the $\delta^{18}O_c$-sea level relationship during interglacials likely results from warmer high latitudes with less depleted $\delta^{18}O_{ice}$ after 400 ka. Glacial maxima after 400 ka may also have been warmer with less depleted NH $\delta^{18}O_{ice}$, but this apparent change during glacial maxima could be an artifact of bias in the sea level stack during MIS 12 and 16. Changes in the relationship between benthic $\delta^{18}O_c$ and sea level are also likely to have occurred during the early or mid-Pleistocene. For example, the same regression probably would not apply to the 41-ka glacial cycles of the early Pleistocene (Tian et al., 2003).

7 Differences between sea level proxies

Whereas PC1 tells us about the common variance between the sea level proxies, PC2 and PC3 tell us about their differences. PC2 represents 6% and 8% of the variance for the short and long time windows, respectively. The scores and loads are similar for both analyses (Fig. 5 and Table 1) except for a sign change; therefore, we multiply by -1 the scores and loads of PC2 and PC3 of the short time window. Large PC2 loadings with opposite sign contributions for the 1123 and 607 benthic $\delta^{18}O_{sw}$ records suggest that PC2 represents differences in the $\delta^{18}O_{sw}$ of deep water in the Atlantic and Pacific basins. Most notably, PC2 has a strong peak at approximately 250 ka (Fig. 5), associated with very low

values in the 607 benthic $\delta^{18}O_{sw}$ record and very high values in the 1123 benthic $\delta^{18}O_{sw}$ record (Fig. 1).

PC3 captures 5% of the variance in the 430-ka stack and 6% of the variance in the 798-ka stack. Unlike PC1 and PC2, the loads vary between the short and long PC3 (Table 1); here we focus on the short version because it contains more proxy records. In the 430-ka stack, PC3 is most highly represented by the planktonic $\delta^{18}O_{sw}$ stack with a load of -0.7 and the 1123 and 607 benthic $\delta^{18}O_{sw}$ records with loads of about 0.5. These loads suggest that PC3 dominantly reflects planktonic versus benthic differences in $\delta^{18}O_{sw}$. PC3 scores exhibit a linear trend from 0-430 ka, which supports the findings of previous studies that suggest planktonic $\delta^{18}O_{sw}$ should be detrended for conversion to sea level (Lea et al., 2002; Shakun et al., 2015). Furthermore, PC3 suggests that benthic $\delta^{18}O_{sw}$ may also need to be detrended in the opposite direction. This effect could be caused by long-term changes in the hydrologic cycle or deep water formation processes, which lead to a change in the partitioning of oxygen isotopes between the surface and deep ocean.

8 Conclusions

PCA indicates a strong common sea level signal in the seven records analyzed for 0-430 ka and five records for 0-798 ka. Furthermore, the similarity between the short and long stacks indicate that the longer stack with five records is nearly as good an approximation of sea level as the seven-record stack. Sea level estimates for each interglacial vary greatly between records, producing standard deviations of 11-26 m. Generally, the mean for each individual highstand is greater in magnitude than our stack estimate. Based on comparison with GIA-corrected coral sea level estimates for MIS 5e and 11, the stack likely reflects mean sea level for each interglacial and fails to capture brief sea level highstands, such as those lasting only ~2 ka during MIS 5e (Kopp et al., 2013).

A comparison of individual records shows that high and lowstand estimates have a mean standard deviation of 17 m (for MIS 5e - 19). Uncertainty in the stack is estimated using bootstrapping and random sampling, which yields a mean standard deviation for scaled PC1 of 9.4 m with seven records (0-430 ka) and 12 m with five records (0-798 ka). The bootstrap uncertainty estimates also include age uncertainty; however, this systematically smooths the bootstrap results and, thus, underestimates individual highstands relative to both individual records and scaled PC1 (Figure 2c).

We estimate that sea level change accounts for only about 45% of the orbital-band variance in benthic $\delta^{18}O_c$, compared to 65% of the LGM-to-Holocene benthic $\delta^{18}O_c$ change. Nonetheless, benthic $\delta^{18}O_c$ is strongly correlated with sea level ($r = -0.9$). If LR04 benthic $\delta^{18}O_c$ stack is smoothed and lagged by 2 ka, the relationship between benthic $\delta^{18}O_c$ and sea level is well-described by a linear function from 398-798 ka and a quadratic function from 0-398 ka. In particular, interglacials MIS 9 and 5e which had larger ice sheets than MIS 11 appear to have been as warm (or warmer) than MIS 11 with isotopically less depleted ice sheets.

The second and third principal components of the sea level records describe differences between the proxies. PC2 represents the difference between the $\delta^{18}O_{sw}$ of deep water in the Atlantic and Pacific basins; a peak in PC2 scores at 250 ka indicates large differences between the basins at this time. PC3 represents the differences between planktonic and benthic $\delta^{18}O_{sw}$ records and suggests a linear trend between the two from 0-430 ka. Thus, $\delta^{18}O_{sw}$ records vary across ocean basins and between the surface and the deep. In conclusion, the stack of sea level proxies presented here should be a more accurate eustatic sea level record than any of the individual records it contains.

Table 1 Principal Component Analysis (PCA) loading for each proxy record. "Short" refers to the 0-430 ka time window, and "Long" refers to 0-798 ka. Numbers in parentheses give the percent variance explained by each principal component.

	PC1 Short (83%)	PC1 Long (77%)	PC2 Short (6%)	PC2 Long (8%)	PC3 Short (5%)	PC3 Long (6%)
Inverse model (Bintanja et al., 2005)	0.4	0.48	-0.05	-0.11	-0.16	0.02
Pac. benthic $\delta^{18}O_{sw}$ (Elderfield et al., 2012)	0.34	0.44	-0.7	-0.5	0.52	0.67
Planktonic $\delta^{18}O_{sw}$ (Shakun et al., 201	0.37	0.45	-0.01	-0.19	-0.65	-0.65
RSL_{Med} (Rohling et al, 2014)	0.38	0.45	0	0.01	0.04	-0.27
Atl. benthic $\delta^{18}O_{sw}$ (Sosdian and Rosenthal, 2009)	0.35	0.42	0.7	0.84	0.51	0.26
$\delta^{18}O_c$ regression (Waelbroeck et al., 2002)	0.4	-	0.08	-	-0.11	--
RSL_{Red} (Rohling et al., 2009)	0.4	-	-0.01	-	-0.07	--

Table 2 Sea level highstand and lowstand estimates from individual records (in meters above modern). See Table 1 for references. The last column gives the mean values from nine cores in Bates et al (2014); these estimates were not included in our PCA.

Marine Isotope Stage	Age (ka)	Inverse model	Pac. benthic $\delta^{18}O_{sw}$	RSL $_{Red}$	RSL $_{Med}$	Plank. $\delta^{18}O_{sw}$	Atl. benthic $\delta^{18}O_{sw}$	$\delta^{18}O_c$ regression	Bates et al. (2014) mean
2	18-25	123	-113	-114	-120	-130	-124	-123	-133
5e	119-126	0	3	18	-4	-10	28	4.9	12
6	135-141	123	-130	-99	-94	-138	-97	-129	-130
7a-c	197-214	-20	12	14	12	-16	34	-3.6	-3
7e	236-255	-18	16	-3	1	-20	-6.2	-9.4	-10
9	315-331	-0.5	40	11	-5	-27	43	5	8
10	342-353	111	-96	-114	-77	-98	-112	-126	-122
11	399-408	0	58	4	12	-5	57	5.7	9
12	427-458	126	-146	-118		-142	-100		-147
13	486-502	-29	18		-8	-11	32		-5
16	625-636	126	-113			-144	-125		-141
17	682-697	-23	31		0.5	-12	8.1		-4
19	761-782	-21	21		7.2	-1	-6.8		-2

Table 3 Mean and standard deviation of sea level highstand and lowstand estimates (in meters above modern) from Table 2 compared to scaled PC1 and GIA-corrected from corals and other coastal proxies. GIA-corrected estimates for MIS 2 are from Clark et al. (2009) and Lambeck et al. (2014), for MIS 5e from Dutton et al. (2015), and for MIS 11 from Raymo and Mitrovica (2013). Bootstrap 95% confidence intervals are from sampling the seven-record short PC1 for MIS 2 – 11 and from the five-record long PC1 for MIS 12 – 19.

Marine Isotope Stage	Age Range (ka)	Standard deviation	Mean	GIA corrected estimates	Scaled PC1 (0-430 ka)	Scaled PC1 (0-798 ka)	Bootstrap 95% confidence interval
2	18-25	7	-123	-130 to -134	-130	-130	-136 to-128
5e	119-126	12	7	6 to 9	3	-1	-14 to 17
6	135-141	18	-118		-123	-125	-142 to-111
7a-c	197-214	18	4		-7	-5	-25 to 14
7e	236-255	11	-6		-9	-13	-32 to -1
9	315-331	23	9		-1	-2	-27 to 20
10	342-353	16	-107		-108	-103	-128 to -92
11	399-408	25	18	6 to 13	16	19	-11 to 40
12	427-458	19	-130			-124	-163 to -100
13	486-502	22	-1			-11	-35 to 16
16	625-636	13	-130			-115	-149 to -87
17	682-697	19	0			-9	-28 to 15
19	761-782	14	0			-6	-25 to 10

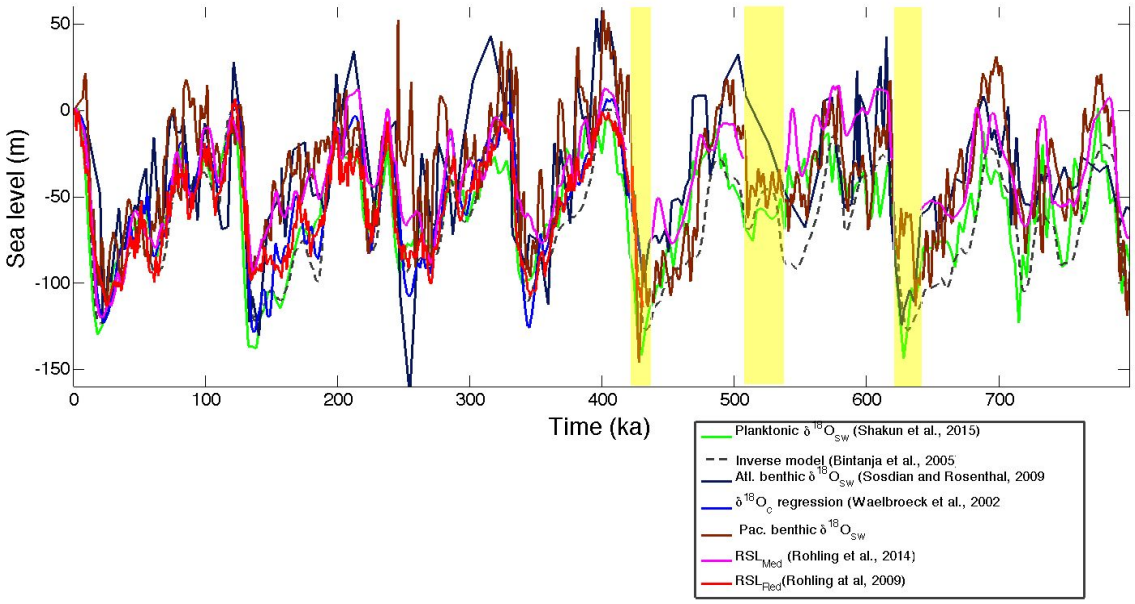

Figure 1 Eustatic and relative sea level estimates for the seven records on the LR04 age model (Lisiecki and Raymo, 2004). Yellow bars mark the sapropel layers removed from the Mediterranean RSL record (Rohling et al, 2014).

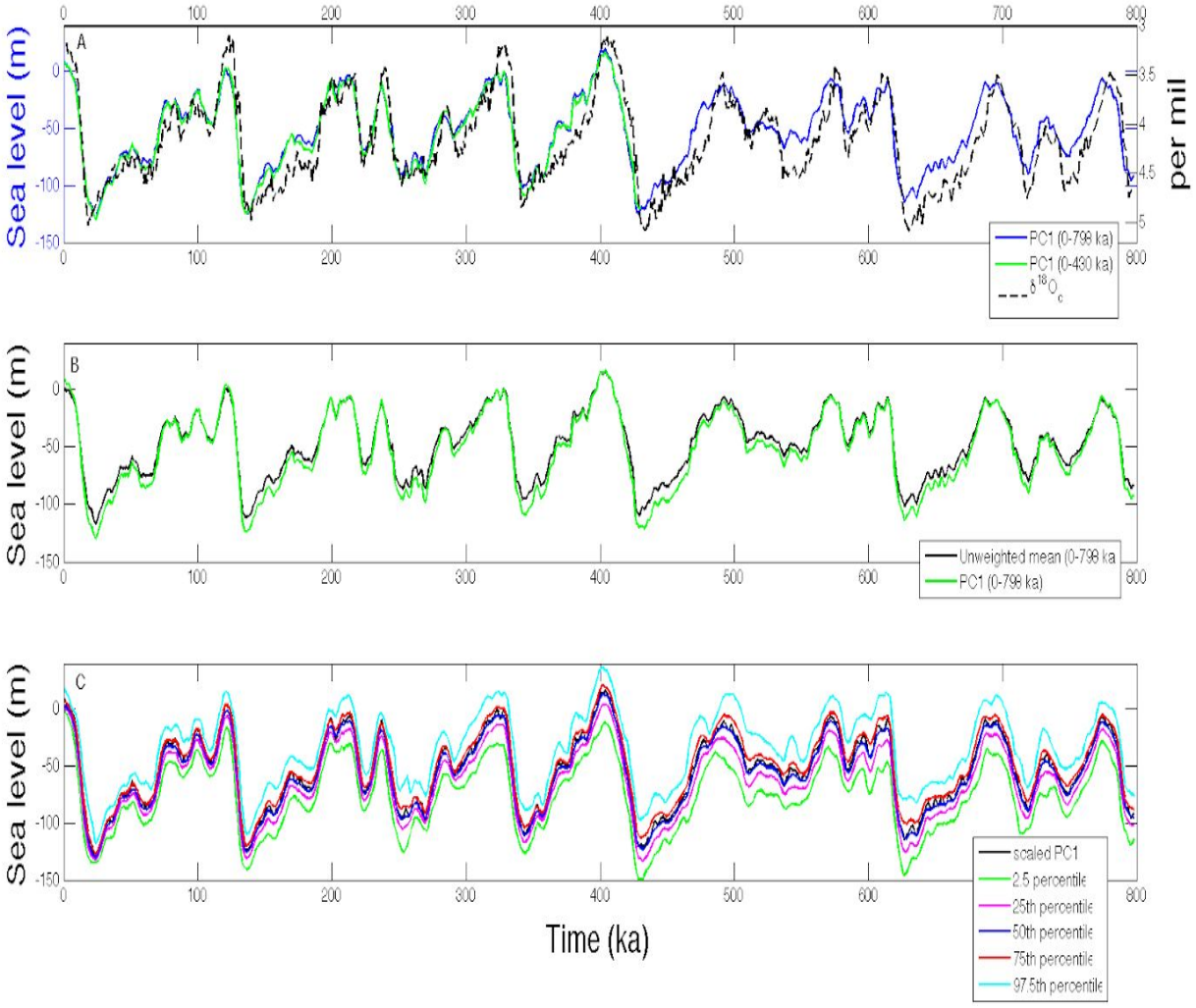

Figure 2 A. Long and short sea level stacks compared to the LR04 benthic $\delta^{18}O_c$ stack (Lisiecki and Raymo, 2005). B. Scaled PC1 compared to unweighted mean of individual records. Scaled PC1 is comprised of short PC1 (0-431 ka) pasted to long PC1 (431-798 ka). C. Scaled PC1 compared with percentile levels from the bootstrap results, which are also plotted as a composite of the short (0-431 ka) and long (431-798 ka) time windows.

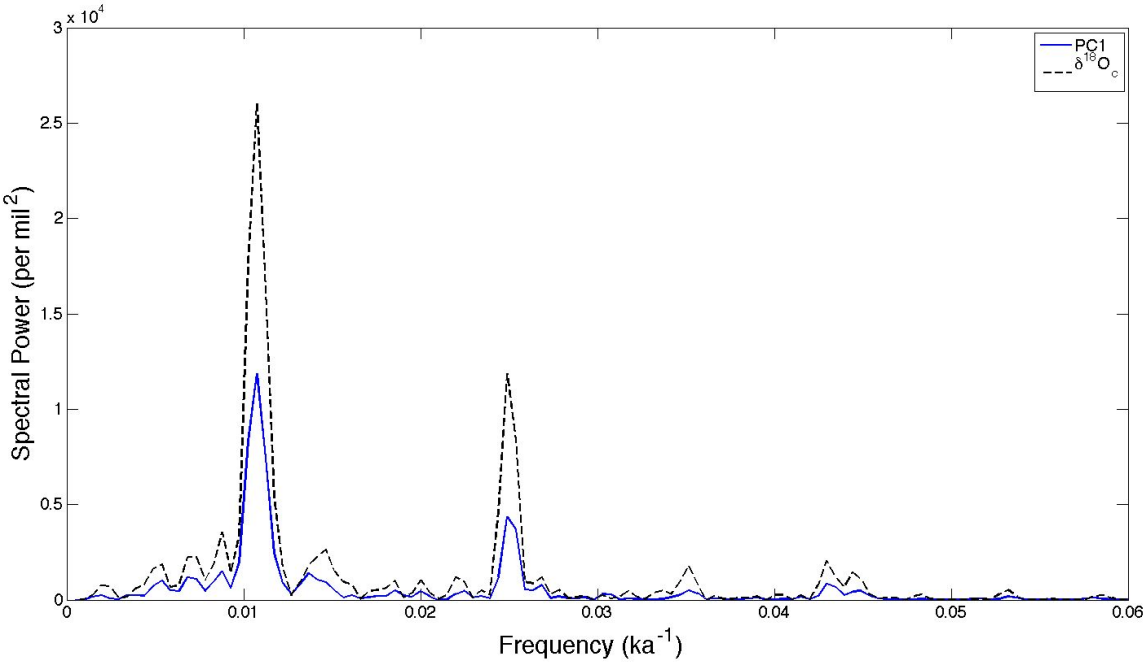

Figure 3 Spectral analysis for composite sea level stack (scaled PC1) converted to its $\delta^{18}O_{sw}$ contribution using 0.009‰m^{-1} and benthic $\delta^{18}O_c$ stack (Lisiecki and Raymo, 2005) from 0-798 ka.

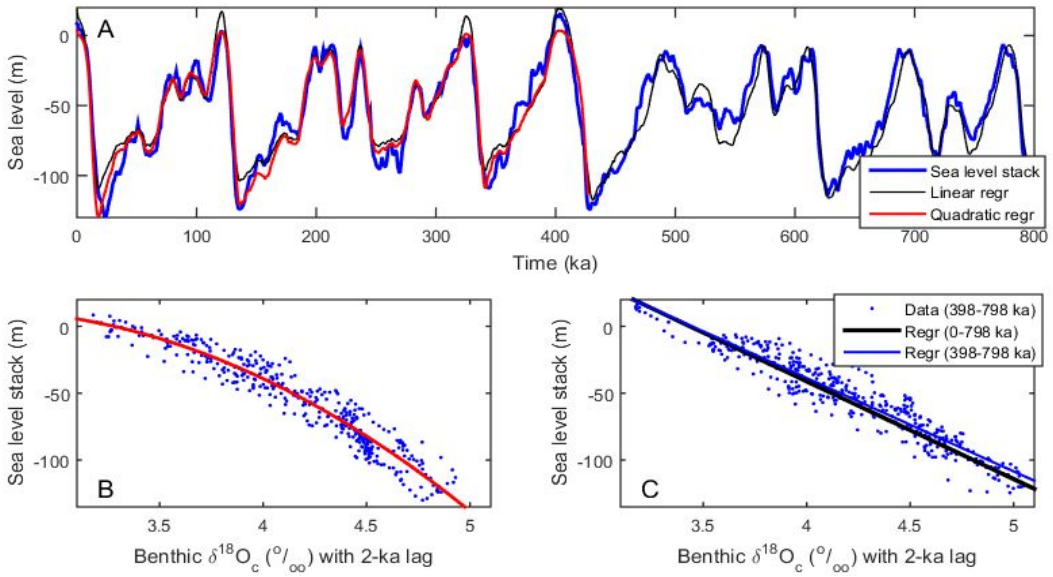

Figure 4 Comparison of benthic $\delta^{18}O_c$ and sea level. A. Linear and quadratic sea level models (Eq. 1 and 2, respectively) using smoothed benthic $\delta^{18}O_c$ (Lisiecki and Raymo, 2005) lagged by 2 ka. B. Data from 0-397 ka with quadratic regression (red line). C. Data from 398-798 ka with linear regression for 0-798 ka (black line) and 398-798 ka (blue line).

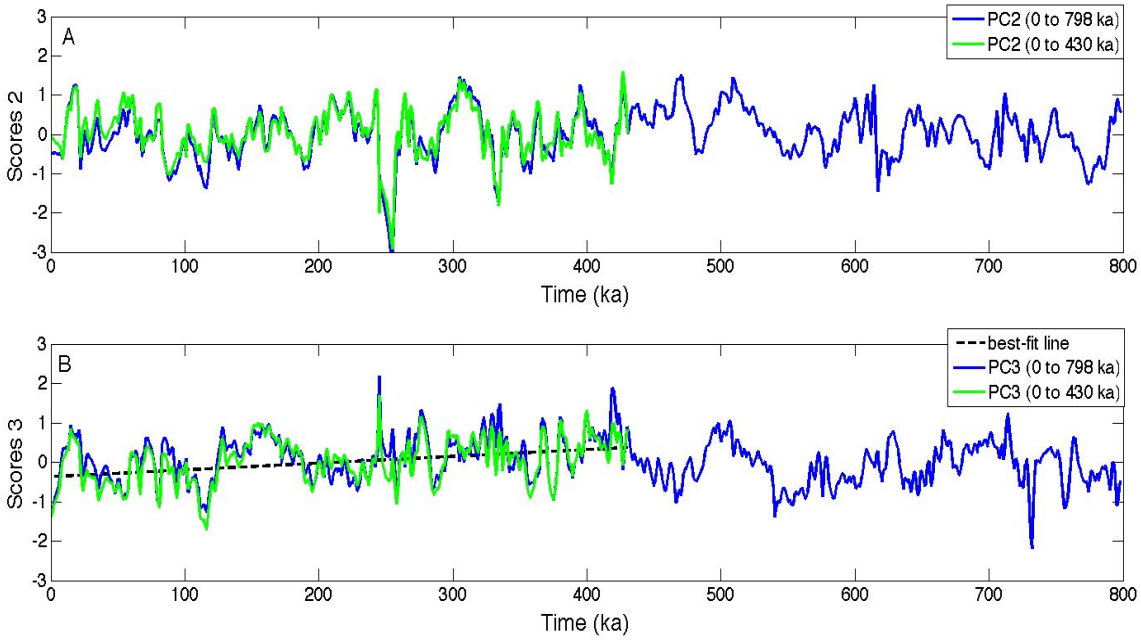

Figure 5 Second and third principal components for 0-430 ka and 0-798 ka. A. Scores for PC2 largely reflect difference between Atlantic and Pacific benthic $\delta^{18}O_{sw}$. B. Scores for PC3 largely reflect the difference between benthic and planktonic $\delta^{18}O_{sw}$. Dashed black line marks linear trend from 0-430 ka.

9 References

Abe-Ouchi, A., Saito, F., Kawamura, K., Raymo, M. E., Okuno, J., Takahashi, K., & Blatter, H.: Insolation-driven 100,000-year glacial cycles and hysteresis of ice-sheet volume.,Nature, *500*,7461, 190–3, doi: 10.1038/nature12374, 2013.

Adkins J. F., McIntyre, K., Schrag, D. P.: The Salinity, Temperature, and $\delta^{18}O$ of the Glacial Deep Ocean, Science, 29, 298, 5599, 1769-1773, doi: 10.1126/science.1076252, 2002.

Andersen, M.B., Stirling, C.H., Potter, E.K., Halliday, A.N., Blake, S.G., Mc-Culloch, M.T., Ayling, B.F. and O'Leary, M.: High-precision U-series measurements of more than 500,000 year old fossil corals, Earth and Planetary Science Letters, 265, 229-245, 2008.

Bard, E., Hamelin, B., Fairbanks, R. G., Zindler, A.: Calibration of the ^{14}C timescale over the past 30,000 years using mass spectrometric U–Th ages from Barbados corals, Nature, 345, 405-410, 1990.

Bard, E., Hamelin, B., Arnold, M., Montaggioni, L., Cabioch, G., Faure, G., & Rougerie, F.: Deglacial sea-level record from Tahiti corals and the timing of global meltwater discharge, *Nature,* doi: 10.1038/382241a0, 1996.

Bates, S. L, Siddall, M., Waelbroeck, C.: Hydrographic variations in deep ocean temperature over the mid-Pleistocene transition, Quaternary Science Reviews, 88, 147-158, doi:10.1016/j.quascirev.2014.01.020, 2014.

Bintanja, R., Roderik, S.W., van de Wal, O. J.: Modeled atmospheric temperatures and global sea levels over the past million years, Nature, 437, 125-128 doi:10.1038/nature03975, 2005.

Blanchon, P., Eisenhauer, A., Fietzke, J., & Liebetrau, V.: Rapid sea-level rise and reef back-stepping at the close of the last interglacial highstand, Nature, 458, 7240, 881–884, doi: 10.1038/nature07933, 2009.

Boak, E. H., Turner, I. L.: Shoreline Definition and Detection: A Review, Journal of Coastal Research, 214, 688–703, doi: 10.2112/03-0071.1, 2005.

Bowen, D. Q.: Sea level,~400,000 years ago (MIS 11): analogue for present and future sea-level?, Clim. Past, 6,19–29, 2010.

Bryden, H. L., Kinder T.H.: Steady two-layer exchange through the Strait of Gibraltar, Deep Sea Res., 38, S1, S445–S463, 1991.

Clark, P.U., Dyke, A.S., Shakun, J.D., Carlson, A.E., Clark, J., Wohlfarth B., Mitrovica, J. X., Hostetler S.W., McCabe A. M.: The Last Glacial Maximum, Science, 325, 5941, 710-714, doi: 10.1126/science.1172873, 2009.

Clark, P. U., et al.: Global climate evolution during the last deglaciation, Proceedings of the National Academy of Sciences, 109,19, E1134–E1142, doi: 10.1073/pnas.1116619109, 2012.

Creveling, J.R., Mitrovica, J.X., Hay, C.C., Austermann, J., Kopp, R.E.: Revisiting tectonic corrections applied to Pleistocene sea-level highstands, Quat. Sci. Rev., 111, 72-80, doi:10.1016/j.quascirev.2015.01.003, 2015.

Duplessy, J.C., Labeyrie, L., Waelbroeck, C.: Constraints on the ocean isotopic enrichment between the Last Glacial Maximum and the Holocene: Paleoceanographic implications, Quat. Sci. Rev., 21, 315-330, 2002.

Dutton, A, Carlson, A., Long, A., Milne, G., Clark, P., DeConto, R., Horton, B. P., Rahmstorf S., Raymo, M.: Sea-level rise due to polar ice-sheet mass loss during past warm periods, Science, *349*, 6244, 153 aaa4019–1. http://doi.org/10.1126/science.aaa4019, 2015.

Dutton, A., Lambeck, K.: Ice Volume and Sea Level During the Last Interglacial, Science, 337, 216–220, 2012.

Dwyer, G. S., Cronin, T. M., Baker, P. A., Raymo, M. E., Buzas, J. S., & Corrige, T.: North Atlantic Deepwater Temperature Change During Late Pliocene and Late Quaternary Climatic Cycles, Science, 270, 1347–1351, doi: 10.1126/science.270.5240.1347, 1995.

Edwards, R.L., Beck, J. W., Burr, G. S., Donahue, D. J., Chappell, J. M. A., Bloom, A. L., Druffel, E. R. M., Taylor, F. W.: A Large Drop in Atmospheric $^{14}C/^{12}C$ and Reduced Melting in the Younger Dryas, Documented with ^{230}Th Ages of Corals, Science, 260, 962-968, 1993.

Elderfield, H., Ferretti, P., Greaves, M., Crowhurst, S. J., McCave, I.N., Hodell, D. A., Piotrowski, A. M.: Evolution of ocean temperature and ice volume through the Mid-Pleistocene Climate Transition, Science, 337,6095, 704-709, doi:10.1126/science.1221294, 2012.

Fairbanks, R.G.: A 17,000 year glacio-eustatic sea level record: influence of glacial melting rates on the Younger Dryas event and deep-ocean circulation, Nature, 342, 637-642, 1989.

Ganopolski, A., Calov, R.: The Role of Orbital Forcing, Carbon Dioxide and Regolith in 100 kyr Glacial Cycles, Climate of the Past, 7, 1415-1425, 2011.

Gibbons, F. T., Oppo, D. W., Mohtadi, M., Rosenthal, Y., Cheng, J., Liu, Z., Linsley, B.K.: Deglacial $\delta^{18}O$ and hydrologic variability in the tropical Pacific and Indian Oceans, Earth and Planetary Science Letters, 387, 240–251, 2014.

Govin, A., Braconnot, P., Capron, E., Cortijo, E., Duplessy, J.-C., Jansen, E., Labeyrie, L., Landais, A., Marti, O., Michel, E., Mosquet, E., Risebrobakken, B., Swingedouw , D., Waelbroeck, C.: Persistent influence of ice sheet melting on high northern latitude climate during the early Last Interglacial, Climate of the Past, *8*, 2, 483–507, doi: 10.5194/cp-8-483-2012, 2012.

Grant, K.M., Rohling, E.J., Bronk Ramsey, C., Cheng, H., Edwards, R.L., Florindo, F., Heslop, D., Marra, F., Roberts, A.P. Tamisiea, M.E., and Williams, F.: Sea-level variability over five glacial cycles, Nature Communications, *5*, 5076, doi: 10.1038/ncomms6076, 2014.

Hanebuth, T., Stattegger, K., Grootes, P. M.: Rapid Flooding of the Sunda Shelf: A Late-Glacial Sea-Level Record, *Science*, *288,*1033–1035, doi: 10.1126/science.288.5468.1033, 2000.

Hay, C., Mitrovica, J. X., Gomez, N., Creveling, J. R., Austermann, J., & E. Kopp, R.: The sea-level fingerprints of ice-sheet collapse during interglacial periods, Quaternary Science Reviews, *87*, 60–69, doi: 10.1016/j.quascirev.2013.12.022, 2014.

Horton, B. P.: Late Quaternary Relative Sea-level Changes in Late Quaternary Relative Sea-level Changes in Mid-latitudes, Encyclopedia of Quaternary Science, 2064–3071, 2006.

Huybers, P. and C. Wunsch: A depth-derived Pleistocene age model: Uncertainty estimates, sedimentation variability, and nonlinear climate change, Paleoceanography, 19, 1–24, doi: 10.1029/2002PA000857, 2004.

Jouzel, J., Masson-Delmotte, V., Cattani, O., Dreyfus, G. Falourd, S., Hoffmann, G., Minster, B., Nouet, J., Barnola, J. M., Chappellaz, J., Fischer, H., Gallet, J. C., Johnsen, S., Leuenberger, M., Loulergue, L., Luethi, D., Oerter, H., Parrenin, F., Raisbeck, G., Raynaud, D., Schilt, A., Schwander, A., Selmo, E., Souchez, R., Spahni, R., Stauffer, B., Steffensen, J. P. Stenni, B., Stocker, T. F., Tison, J. L., Werner, M., Wolff, E. W.: Orbital and Millennial Antarctic Climate Variability over the Past 800,000 Years, Science 317, 793, doi: 10.1126/science.1141038, 2007.

Kopp, R. E., Simons, F. J., Mitrovica, J. X., Maloof, A. C., Oppenheimer M.: Probabilistic assessment of sea level during the last interglacial stage, Nature, 462, 863-867, doi:10.1038/nature08686, 2009.

Kopp, R. E., Simons, F. J., Mitrovica, J. X., Maloof, A. C., Oppenheimer M.: A probabilistic assessment of sea level variations within the last interglacial stage, Geophys. J. Int*.,* 193, 711–716, 2013.Lambeck, K., Esat, T. M., & Potter, E.-K. (2002). Links between climate and sea levels for the past three million years, *Nature*, *419*, 6903, 199–206, doi: 10.1038/nature01089, 2002.

Lambeck, K., Rouby, H., Purcell A., Sun, Y., Sambridge, M.: Sea level and global ice volumes from the Last Glacial Maximum to the Holocene, Proc. Nat. Ac. Sci., 111, 43, doi:10.1073/pnas.1411762111, 2014.

Lea, D. W., Martin, P. a., Pak, D. K., & Spero, H. J.: Reconstructing a 350 ky history of sea level using planktonic Mg/Ca and oxygen isotope records from a Cocos Ridge core, Quaternary Science Reviews, 21,1-3, 283–293, doi: 10.1016/S0277-3791(01)00081-6, 2002.

Lisiecki, L. E., Raymo, M. E.: A Pliocene-Pleistocene stack of 57 globally distributed benthic $\delta^{18}O$ records, Paleoceanography, 20, PA1003, doi:10.1029/2004PA001071, 2005.

Lisiecki, L. E., & Raymo, M. E.: Diachronous benthic δ^{18} O responses during late Pleistocene terminations, Paleoceanography, *24*, 3, doi: 10.1029/2009PA001732. 2009.

Masson-Delmotte, V., Stenni, B., Jouzel, J., Landais, A., Röthlisberger R., Minster B., Hansen, J., Pol K., Barnola, J.M., Mikolajewicz, U., Braconnot, P., Chappellaz, J., Otto-Bliesner, B., Cattani, O., Krinner, G.: EPICA Dome C record of glacial and interglacial intensities, Quat. Sci. Rev., 29, 113-128, 2010.

Medina-Elizalde, M.: A compilation of coral sea level benchmarks: Implications and new challenges, Earth. Planet. Sc. Lett., 362, 310-318, 2013.

Petit, J. R., Jouzel, J., Raynaud, D., Barkov, N. I., Barnola, J. -M., Basile, I., Bender, M., Chappellaz, J., Davisk, M., Delaygue, G., Delmotte, M., Kotlyakov, V. M., Legrand, M., Lipenkov, V. Y., Lorius, C., Pépin, L., Ritz, C., Saltzman, E., Stievenard M.: Climate and atmospheric history of the past 420,000 years from the Vostok ice core, Antarctica, Nature, 399, 429-436, 1999.

Martin, P. A., Lea, D. W., Rosenthal, Y., Shackleton, N. J., Sarnthein, M., & Papenfuss, T.: Quaternary deep sea temperature histories derived from benthic foraminiferal Mg/Ca, Earth and Planetary Science Letters, *198*,1-2, 193–209. doi: 10.1016/S0012-821X(02)00472-7, 2002.

Medina-Elizalde, M.: A global compilation of coral sea-level benchmarks: Implications and new challenges, Earth and Planetary Science Letters, 362, 310–318, doi.: 10.1016/j.epsl.2012.12.001, 2013.

Muhs, D. R., Meco, J., Simmons, K. R.: Uranium-series ages of corals, sea level history, and palaeozoogeography, Canary Islands, Spain: An exploratory study for two Quaternary interglacial periods, Palaeogeography, Palaeoclimatology, Palaeoecology, 394, 99–118, doi: 10.1016/j.palaeo.2013.11.015, 2014.

Raymo, M. E., Mitrovica, J. X.: Collapse of polar ice sheets during the stage 11 interglacial, Nature, doi:10.1038/nature10891, 2012.

Raymo M.E., Ruddiman W.F., Shackleton N.J., Oppo D.W.: Evolution of Atlantic-Pacific $\delta^{13}C$ gradients over the last 2.5 m.y., Earth Planet. Sci. Lett., 97, 353-368, 1990.

Rohling, E.J., Grant, K., Bolshaw, M., Roberts, A.P., Siddall, M., Hemleben, C., Kucera, M.: Antarctic temperature and global sea level closely coupled over the past five glacial cycles. Nat. Geosci., 2, 500–504, 2009.

Rohling, E. J. et al. Reconstructing past planktic foraminiferal habitats using stable isotope data: a case history for Mediterranean sapropel S5, Mar. Micropaleontol. 50, 89–123, 2004.

Rohling, E. J., Grant, K.M., Bolshaw, M., Roberts, A. P., Siddall, M., Hemleben C. Kucera, M., Foster, G.L., Marino, G., Roberts, A.P., Tamisiea, M.E., and Williams, F.: Sea-level and deep-sea-temperature variability over the past 5.3 million years, Nature, 508, 477–482, 2014.

Schiebel, R., Zeltner, A., Treppke, U. F., Waniek, J.J., Bollmann, J., Rixen, T., Hemleben, C.: Distribution of diatoms, coccolithophores and planktic foraminifera in the Arabian Sea, Mar. Micropaleontol., doi: 51, 345-371, doi:10.1016/j.marmicro.2004.02.001, 2004.

Shackleton, N. J.: Attainment of isotopic equilibrium between ocean water and the benthonic foraminifera genus Uvigerina: Isotopic changes in the ocean during the last glacial, Colloque International sur les Methodes Quantitatives d'Etude des Variation du Climat au Sours du Pleistocene, Coll. Int. C.N.R.S., 219, 203–209, 1974.

Shakun, J.D., Clark, P.U., He, F., Marcott, S. A., Mix, A. C., Liu, Z., Otto-Bliesner, B., Schmittner A., Bard E.: Global warming preceded by increasing carbon dioxide concentrations during the last deglaciation, Nature, 484, 49–54, doi:10.1038/nature10915, 2012.

Shakun, J. D., Lea, D. W., Lisiecki, L. E., Raymo, M. E.: An 800-kyr record of global surface ocean $\delta^{18}O$ and implications for ice volume-temperature coupling, Earth. Planet. Sc. Lett., 426, 58–68, 2015

Siddall, M., Hönisch, B., Waelbroeck, C., Huybers, P.: Changes in deep Pacific temperature during the mid-Pleistocene transition and Quaternary, Quat. Sci. Rev., 29, 170-181, 2010.

Siddall, M., Smeed, D.A., Hemleben, Ch., Rohling, E.J., Schmeltzer, I., and Peltier, W.R.: Understanding the Red Sea response to sea level, Earth. Planet. Sc. Lett., 225, 421-434, 2004.

Skinner, L. C., Shackleton, N. J.: An Atlantic lead over Pacific deep-water change across Termination I: implications for the application of the marine isotope stage stratigraphy, Quaternary Science Reviews, 24, 5-6, 571–580, doi: 10.1016/j.quascirev.2004.11.008, 2005.

Sosdian S., Rosenthal Y.: Deep-Sea Temperature and Ice Volume Changes Across the Pliocene-Pleistocene Climate Transitions, Science, 17, 325, 5938, 306-310, doi: 10.1126/science.1169938, 2009.

Stein, M., Wasserburg, G., Aharon, P., Chen, J., Zhu, Z. ., Bloom, a, & Chappell, J.: TIMS U-series dating and stable isotopes of the last interglacial event in Papua New Guinea, Geochimica et Cosmochimica Acta, 57, 11, 2541–2554, doi: 10.1016/0016-7037(93)90416-T, 1993.

Stern, J. V., Lisiecki, L.E.: Termination 1 timing in radiocarbon dated regional benthic $\delta^{18}O$ stacks, Paleoceanography, 29, 1127-1142, doi:10.1002/2014PA002700, 2014.

Stirling, C. H., Esat, T. M., McCulloch, M. T., & Lambeck, K.: High-precision U-series dating of corals from Western Australia and implications for the timing and duration of the Last Interglacial, Earth and Planetary Science Letters, *135*, 1-4, 115–130 doi: 10.1016/0012-821X(95)00152-3, 1995.

Thompson, W. G., Goldstein, S. L.: Open-System Coral Ages Reveal Persistent Suborbital Sea-Level Cycles, Science, 308, 5720, 401-404, doi: 10.1126/science.1104035, 2005.s on the Tibetan Plateau, J. Geophys. Res.,108, 4293, D9, 2003.

Waelbroeck, C., Labeyrie, L., Tian, L., Yao T., Schuster, P.F., White, J.W.C., Ichiyanagi K., Pendall, E., Pu, J., Yu W.: Oxygen-18 concentrations in recent precipitation and ice coreMichel, E., Duplessy J.C., McManus J.: Sea-level and deep water temperature changes derived from benthic foraminifera isotopic records, Quaternary Sci. Rev., 21, 295–305, 2002.

Wang, P., Tian, J. & Lourens, L. J.: Obscuring of long eccentricity cyclicity in Pleistocene oceanic carbon isotope records, Earth Planet. Sci. Lett., 290, 319–330 , 2010.

III Tuning a 3-box model to modern $\delta^{18}O_{sw}$ of seawater targets in the Atlantic Ocean

1 Introduction

This chapter describes a three-box ocean reservoir model and experiments simulating modern values of the oxygen isotope composition of seawater ($\delta^{18}O_{sw}$) in the Atlantic Ocean. The focus of this chapter is to test the ability of a simple box model of ocean dynamic processes to match observed mean values of the $\delta^{18}O$ of seawater for the model's boxes. The model's tracer, $\delta^{18}O_{sw}$, is a standard way of describing the ratio of the heavy (^{18}O) to light (^{16}O) oxygen isotopes present in seawater. The model is a steady-state ocean system with three reservoirs in the Atlantic (low-latitude surface box, high-latitude surface box, and deep box) and water vapor transport flux from low to high-latitudes across 50° North. In addition to vapor transport (in Sv), the other model parameters include water vapor fractionation of $\delta^{18}O$, overturning circulation and vertical and horizontal mixing between ocean boxes (in Sv). A general circulation model (GCM) was used to develop the parameters of atmospheric transport flux and alpha (Battisti et al., 2014).

The goal of this chapter is to 'tune' the model's parameter values so the model's basin $\delta^{18}O_{sw}$ tracer values match modern-day seawater $\delta^{18}O$ as defined by measurements since

1950 (LeGrande and Schmidt, 2006). The model's parameters are tuned within realistic flux and transport as defined by modern observations of ocean dynamics (Webb and Suginohara, 2001; McCarthy et al, 2015). The model has 6 input parameters and 4 output ocean reservoir $\delta^{18}O_{sw}$ values, which makes it an under-constrained system; therefore, it is possible mathematically to have an infinite number of solutions which fit the observations for the 4 reservoirs. These are defined by the three boxes plus the vapor transport in the model. I hypothesize that the model can be tuned to find *at least* two sets of realistic parameters which match ocean reservoir $\delta^{18}O_{sw}$ values in each of its 3 boxes and its atmospheric flux.

Sensitivity tests are difficult to perform using complex models due to the intricacy of model parameter interactions; the small number of parameters in the box model will help provide insight into the climate impact of each dynamic process that would be difficult to deduce from a complex model. The model's sensitivity is determined by changing the values of its parameters independently of each other to test how each affects the modeled high-to-low latitude surface gradient in $\delta^{18}O_{sw}$.

2 Background

2.1 $\delta^{18}O_{sw}$ box models: structure and components

Box models require at least one tracer to define their system of related reservoirs, but tracers may vary according to the type of experiment. For example, inorganic tracers such as $\delta^{18}O$ can simulate physical processes such as the movement of water from low-latitude surface ocean through the atmosphere to the surface high-latitude ocean; atmospheric transport causes selective fractionation of the isotope (Rayleigh fractionation). Literature values of flux between reservoirs are important for testing model validity. Flux values can be tuned to produce $\delta^{18}O$ values that match observed concentrations for the reservoirs being examined. Specifically, the modeled fluxes are overturning, vertical and horizontal mixing between basins, atmospheric vapor transport and isotopic enrichment of the low-latitude surface ocean, depletion of the high latitude surface ocean. Flux values between basins and fractionation parameters affect final tracers in each modeled ocean reservoir.

Spatial resolution of model reservoirs can vary from as coarse as two boxes to as fine as the resolution of a GCM. The number of reservoirs is limited by the user's

computational resources (Archer et al., 2000) and may be based on the desired complexity or simplicity of questions being asked. In general, ocean box models divide reservoirs into surface and deep boxes to distinguish the processes which can be assigned to atmospheric transport and surface mixing from those derived from overturning.

Processes vary according to the location of the box in the ocean system. For example in carbon models inorganic carbon may be fixed in the upper 100 m of the ocean by photosynthesis, whereas the solubility pump requires deeper designations for the surface ocean (Köhler et al., 2005; 2010); carbon in the deep ocean is then sequestered in the ocean floor or lost out of the system into the Earth's crust. The deep ocean floor is a place for burial/removal of small percentages of non-conservative ocean tracers such as organic carbon, calcium carbonate, and phosphate (Wallmann, 2010).

In general, model reservoirs represent oceans and are therefore initialized with real world ocean volumes; however, some abstract or conceptual models give arbitrary depths based on average depths for various processes and box locations in the model. The maximum depth of shallow surface boxes vary generally from 100-300 m. Deep ocean reservoirs generally range from a top height of 300 m to a deepest value of 6000 m (Köhler et al, 2005; 2010, Gebbie, 2014; LeGrande and Schmidt, 2006). In the three-box model of

Toggweiler and Sarmiento (1984), the warm, low-latitude surface box represents 2% of the ocean volume, the cold high-latitude box represents 1% of the ocean volume, and the deep ocean makes up 97% of the total volume.

A previous 3-box $\delta^{18}O$ model has two surface boxes that are both 100 m deep (Mix, 1992). However, surface boxes do not have to be equal depths. A three-box model by Archer et al. (2000) has a 250 m depth boundary for its high-latitude box and a 100 m depth boundary for its low-latitude surface box. Köhler et al. (2005) has a ten-box reservoir model where the surface high-latitude reservoirs are at least 4 times deeper than the surface low-latitude reservoirs. The idea of a deeper high-latitude surface box is supported by high-latitude turbulent mixing that reaches 1000 m depth (Webb and Suginohara, 2001).

2.2 Atmospheric processes in box models with ^{18}O as a tracer

2.2.1 Rayleigh fractionation of ^{18}O

Models with ^{18}O tracers follow the concentration of ^{18}O as it moves throughout model ocean reservoirs or boxes. A latitudinal differential in ^{18}O of seawater is created by the poleward transport of water vapor from the low-latitudes to the high-latitudes. Isotopic

depletion in water vapor during evaporation and transport is created by the ratio of the rates of fractionation between the heavy (and rare) isotope ^{18}O as compared to the light (and ubiquitous) ^{16}O during transport from the low to high-latitude box. The selective fractionation of oxygen isotopes in water vapor is governed by a process called Rayleigh fractionation. Rayleigh fractionation describes changes in the ratio of isotope species in relation to the decreasing reservoir size. In the transport of atmospheric water vapor, Rayleigh fractionation is the depletion of the heavy isotope (e.g., $\delta^{18}O$) as it is evaporated from the low-latitude surface ocean and then by condensation/precipitation as it travels to high-latitudes.

Rayleigh fractionation has been simulated with box models for the last 5 decades. Models such as Mix (1992); Craig and Gordon (1965); Broecker and Peng (1986) examine the process of vapor transport from low to high-latitudes with volumetric flux and a process which modulates the amount of depletion of the high-latitudes and enrichment of the low- latitudes. This model simplifies the Rayleigh fractionation process by using a single, unitless fraction term for water vapor transport.

2.2.2 Depletion of $\delta^{18}O$ during vapor transport in box models

Sophisticated models may use cloud layers to move vapor from the low to the high latitudes whereas others have a simpler setup where depleted vapor is moved directly from the low-latitude surface ocean to the high-latitude surface ocean. However, the depletion of vapor transported to the high latitudes is governed by the selective thermodynamic process of evaporation, latitudinal transport, and precipitation; therefore, we do see similarities in vapor depletion between model types with different structures.

For example, the conceptual atmosphere-ocean model by Craig and Gordon (1965) has several interacting cloud layers and uses a $\delta^{18}O$ depletion value of 17.5‰ from the cloud layer to the surface ocean. However, a simpler model by Broecker (1986) has two boxes in total, a surface reservoir and a deep ocean reservoir; this model also uses a 17.5‰ depletion from the low-latitude surface ocean to the high-latitude ocean. A three-box model by Mix, (1992) yields a 25‰ depletion from the low surface latitudes to the water vapor.

Improvement of the accuracy of individual parameters such as vapor transport in the box model will lead to more useful model predictions. Thus, an attempt to refine the vapor

flux and vapor transport parameters includes modern-day whole earth vapor flux and vapor transport. An earlier estimate for oceanic flux budgets suggests 0.31 Sv of vapor transport across 40° N in the Atlantic (Baumgartner and Reichel, 1975). A more recent model by Sevellec and Fedorov (2011) suggests the largest vapor flux of ~0.26 Sv is transported across 37° N in the Atlantic. A precipitation flux of 0.27-0.35 Sv in the North Atlantic is reported by Emile-Geay et al. (2003). Another study reports a net evaporation flux value of 0.42 Sv south of 40° N in the Atlantic (Broecker et al., 1990). The majority of vapor transport occurs in the mid-latitudes, at latitudes of approximately 37° N and S with ~0.26 Sv of flux transport; North Atlantic latitudes of vapor transport are greatest from 12° N to 60° N, (Oort, 1983). A total-global vapor flux value of 1.5 Sv across 60° N was estimated by Mix (1992) for the present day based on the precipitation minus evaporation values across the northern high latitudes in a GCM (Kutzbach and Guetter, 1986). An atmosphere GCM with a slab ocean has flux of 0.56-0.61 Sv for global-ocean vapor transport across 50° N (Battisti et al., 2014).

2.2.3 Alpha

The unitless fraction which modulates the depletion of a simple model's tracer from one model box to another is defined by the parameter alpha (**α**). The terminology of the depletion fraction alpha (**α**) was codified in a review of stable isotope values in the ocean by Craig and Gordon, (1965). It is defined as the ratio of heavy-to-light isotope of vapor to the heavy-to-light isotope of liquid (indicating depletion). This can be written as: ($Ratio_v/Ratio_l$). A depleted vapor flux is modulated by a parameter which is a simple fraction with a value between 0 and 1, called alpha (**α).** In a simple model **α** determines the concentration of the tracer in the flux of water vapor transported from low-to-high latitudes. This will result in a depleted high-latitude surface ocean box. Because these models do not always separately simulate evaporation, vapor transport, and precipitation fluxes, this is a simplified parameterization of the Rayleigh fractionation in which the modeled $\delta^{18}O$ value of the vapor flux (integrated over the model run to steady-state) is directly proportional to **α**. Therefore, the user can translate from **α** to $\delta^{18}O$ of the flux via the simple expression: $\alpha=1.000+(\delta^{18}O_v/1000)$. For example, a vapor flux of -12 ‰ translates to a fraction of 0.988: 1.000+(-12/1000)=0.988.

2.3 Ocean processes affecting the ^{18}O tracer

All ocean box models require choices for fluxes between reservoirs. Often, estimates of these processes are taken from a combination of modeled and real-world values in the literature (Mix, 1992; Archer, 2000, Köhler, 2005). Atlantic overturning circulation is the main driver of flux between ocean boxes. Overturning in a simple three-box model drives flux from one reservoir box to another, in a loop through all three boxes. Overturning moves in one direction from the high-latitude surface box to the deep box and up to the low latitude surface box. Previous three-box models use overturning fluxes of 19 Sv (Toggweiler and Sarmiento, 2013), 14.5 Sv (Mix, 1992), and 15-20 Sv (Archer and Broecker, 2000).

Areas of deep water formation at 62.5° N in the North Atlantic are estimated to entrain 15 +/- 2 Sv of seawater (Ganachaud and Wunsch, 2000). Overturning stream-functions from GCMs suggest that overturning at 50° N varies with depth from 3 Sv at the surface to 6 Sv at 300 m to 15 Sv at 1000 m (Kuhlbrodt et al, 2001). At 26° N, the mean Atlantic Meridional Overturning (AMOC) flux is 17.5 Sv and lower NADW flux has a mean returning northward flux of 6.5 Sv (Smeed et al., 2014). In addition to overturning, the

North Atlantic also has a small influx of water from the Arctic, consisting of 0.18 Sv of river runoff from Russia and Canada (Ostlund, 1984) and 0.8 Sv of flow through the Bering Strait, 0.1-0.3 Sv of which is freshwater (Jones, et al., 1998; Woodgate et al, 2010).

High-latitude vertical mixing in the three-box model is represented by a bidirectional flux between the (cold) high-latitude surface reservoir and the deep ocean. Modern vertical mixing is reported to be between 9-12 Sv by Webb and Suginohara (1991), which is a re-evaluation of modelling studies by Toggweiler and Samuels (1998), and Doos and Coward (1997). Comparison of observations of NADW convection with modeling results suggests a high-latitude mixing maximum of 8 Sv (McCarthy et al., 2015; Wunsch and Ferrari, 2004). Schmitz and McCartney (1993) conclude that 14 Sv is the maximum total vertical flux, including overturning, in the upper 200 m of the water column in the North Atlantic.

Three-box models do not always use realistic high latitude vertical mixing. In models where CO_2 solubility is a factor, high latitude vertical mixing may vary upwards of 50-300 Sv (Toggweiler 1999; Archer et al., 2000). However, extreme mixing values do not seem to be relevant to models using $\delta^{18}O_{sw}$ as a proxy: For example, vertical mixing between

high latitude cold surface water and deep water is given as 11 Sv in the three-box model by Mix (1992).

Transport between the surface low-latitudes and the deep ocean also includes a bidirectional vertical flux. Vertical mixing between the low-latitude (warm) ocean and the deep ocean is suggested to be 3-5 Sv by Webb and Suginohara (1991). Mix (1992) uses a maximum of 4.5 Sv of vertical mixing between the low-latitude surface box and the deep ocean. Archer et al. (2000) uses a lower value of 1 Sv.

Horizontal mixing is represented by bidirectional flux between the two surface ocean boxes and is represented with a single parameter that serves both as wind driven mixing and mixing driven by latitudinal differences in heat. A mean of 3 Sv fluxis estimated at 26° N and 100 m transport depth (McCarthy et al., 2015). Additionally, 5 Sv of flux travels from the Caribbean northwards through the Florida current (Schmitz and McCartney, 1993). Jansen et al. (2019) estimate that total mixing approaches 6 Sv North of 50° N in the surface Atlantic. The three-box model of Mix (1992) uses a value of 5 Sv mixing between the two surface reservoirs 60° N in the Atlantic.

3 Methods

3.1 Ocean boxes

The three-box model has two surface boxes and a deep box. The model uses Atlantic basin boundaries because a single ocean basin as an initial study area is less complex than an interconnected ocean system. The Atlantic has all the physical requirements of an ocean model including vapor transport from low-to-high latitudes and subsequent high-latitude depletion of $\delta^{18}O_{sw}$, deep water formation, and bidirectional mixing between reservoirs. The separation of the two surface boxes allows depletion of the $\delta^{18}O_{sw}$ in the high-latitude box as compared to the low-latitude box.

The latitude demarcation between high and low-latitude surface boxes in this model is 50° N, and both surface boxes are 225 m deep. The southernmost boundary of the low-latitude reservoir (42° S) is inclusive of transport of water vapor which occurs across the equator. The boundaries of the surface high-latitude box (Figure 1, below) are 50°-74° N, 76° W- 20° E, and the boundaries of the surface low latitude box are in three parts. The *low-latitude box part 1* includes 18°-50° N, 100° W-20° E. *Low-latitude box part 2* has

boundaries of 10°-18°N, 88° W-20° E, while *low-latitude box part 3* encompasses 42° S-10° N, 68° W-20° E. Small, semi-isolated basins were excluded which had $\delta^{18}O_{sw}$ values which differed from open-ocean values. For example, the Hudson Bay and Arctic ocean are depleted in ^{18}O whereas the easternmost Mediterranean is enriched.

Two distinct model configurations in this chapter balance simplicity of model structure with the desire to use realistic flux parameters consistent with literature estimates. Model setup *type 1* (Figure 1) defines a simple overturning cell in the Atlantic; the three sources of flux between the two surface reservoirs are atmospheric transport, overturning, and horizontal mixing. Model setup *type 2* (Figure 2) adds two additional transport terms from the low-latitude surface reservoir to the high-latitude surface reservoir via the Arctic Ocean. These two terms are (1) freshwater river runoff from North America, Europe, and Asia into the Arctic Ocean and (2) Pacific seawater flux through the Bering Strait and Arctic, which derives in part from vapor transport across the Isthmus of Panama. Model setup type 2 matches model vapor flux to more realistic literature flux estimates of vapor transport across 50° North in the Atlantic.

\

Figure 1 Model configuration type 1: Simple Atlantic overturning cell plus atmospheric transport and a horizontal mixing parameter between the two surface boxes.

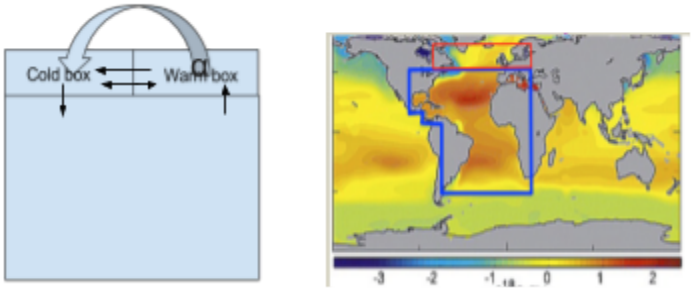

Figure 2 Model configuration type 2: All fluxes from type 1 plus two additional fluxes.

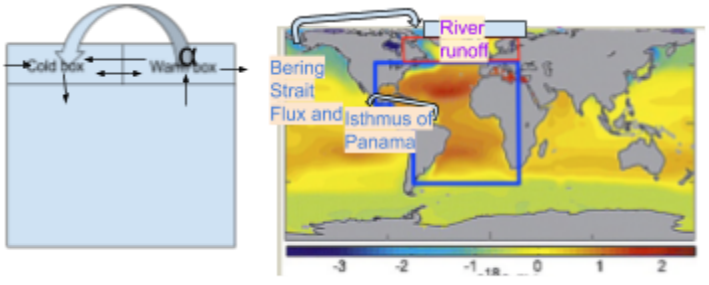

Figure 2 Flux terms from the low-latitude surface box to the high-latitude surface, representing transport through the Bering Strait and continental runoff into the Arctic Ocean. The modern day ocean tuning target $\delta^{18}O_{sw}$ values for the model come from a compilation of $\delta^{18}O_{sw}$ measurements by LeGrande and Schmidt (GISS; 2006) (Figure 3). A modified version of this record is by Gebbie (2014) was used to calculate the $\delta^{18}O_{sw}$ and volume for each of the three ocean reservoir boxes in our model. The $\delta^{18}O_{sw}$ of each ocean box is volume-weighted to account for varying depth increments and diminishing grid-cell size as one moves north or south from the equator. The dataset includes nearly 23,000 points, but gaps still exist in the Southern Ocean. However, this method discards points outside of this grid, in addition to values less than -8 ‰ because they indicate riverine input. Error correction on some of the constituent datasets in this series have been applied.These corrections vary from 0.14-1.0‰. The $\delta^{18}O_{sw}$ of the GISS surface measurements are used as a first guess for the Gebbie (2014) interpolated model inputs; after the data are mapped into the deep ocean via known circulation pathways, the Gebbie (2014) interpolated model's validity is tested against $\delta^{18}O_{sw}$ measurement error, which is considered to be 0.08 ‰ in the deep ocean. The lowest depth boundary of the ocean in the Gebbie (2014) interpolated model is 5750 m, and the grid cells are 4° latitude by 4° longitude.

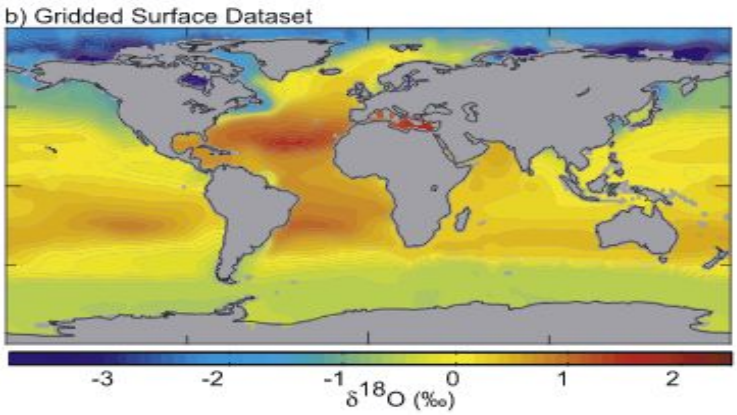

Figure 3 Global gridded dataset of the surface ocean (Legrande and Schmidt, 2006)

3.2 Rayleigh fractionation

The fractionation term alpha **(α)** is defined as $k^{18}O/k^{16}O$, or the ratio of the rates of fractionation of $^{18}O/^{16}O$. However, the model only traces the concentration of the heavier oxygen isotope written as [^{18}O]. The reader can assume for the sake of this model the light isotope ^{16}O remains constant in each of our three ocean basins because it is so plentiful as compared to ^{18}O. Therefore, one can also assume there is no selective fractionation of ^{16}O in the vapor transport from low to high-latitudes and the rate of fractionation of ^{16}O and ($k^{16}O$) approaches the value of 1 in the ratio of $k^{18}O/k^{16}O$ and can therefore be ignored as a variable.

This a closed system; no mass is lost as ^{18}O is fractionated in the water vapor flux from low to high latitudes. The time-evolving value of the concentration of ^{18}O is defined as the change in ^{18}O of vapor at the next time step ($\mathbf{\Delta}^{18}O_v$) which is equal to the rate of fractionation of ^{18}O (***k***^{18}O**)** multiplied by the concentration of ^{18}O **([**$^{18}O_{(\text{at start of vaporization})}$**])** then multiplied by the incremental time step value (**dt)** :

$$\Delta^{18}O_v = k^{18}O^* [^{18}O_{(\text{at start of vaporization})}]^*dt, \qquad (1.1)$$

If alpha (α) is 0.98, then $k^{18}O=0.98$, (and $k^{16}O$ will then be defined as: $k^{16}O=1$), yielding the alpha value of $k^{18}O/k^{16}O = 0.98$.

$$\Delta^{18}O_v = 0.011 \text{ mmol/m^3/s} * [^{18}O_{(\text{at start of vap.})}] * 1 \text{ sec} \quad (1.2)$$

Atmospheric transport $\delta^{18}O$ values and atmospheric flux values across 50° N are derived from the precipitation minus evaporation from an isotope enabled atmosphere GCM (aGCM) with a simple slab ocean (Battisti et al., 2014). The $\delta^{18}O$ value of the water vapor was estimated separately by calculating the fluxes of ^{18}O and ^{16}O. Modern-day daily rain flux values in centimeters per day were converted to volumetric transport values (Sv/yr). The atmospheric flux value in the model is 0.56-0.61 Sv across 50° N. These values are in line with global flux magnitudes across 50° N, with an average isotopic value of -10.8‰. An approximate 0.47 Sv vapor transport across 50° N was observed in a climatological study (Oort, 1983) and 0.76 Sv in an aGCM run (Zaucker et al., 1993). Flux and transport values in the first iteration of this model (Table 2 columns 1 and 2) are derived from whole-earth values instead of Atlantic basin transport because of the difficulty of calculating the percentage of water vapor transport across 50° N only in the Atlantic. The Atlantic is roughly 30% of the world ocean surface area, and because the Atlantic basin accounts for 14% of the distance around the Earth at 50° N, the relevant value for vapor flux in the model is approximately 14-30% of global atmospheric transport (Eakins and Sharman, 2010).

Complex Rayleigh formulations requiring temperature values during the process of fractionation require special integration and will not be explored here. Several models of

historical interest including Craig and Gordon (1965) and Roche (2013) require variables for humidity when developing Rayleigh values and are also beyond the scope of this study.

3.3 Model runs

This model is time-evolving. Seawater $\delta^{18}O$ for each box is initialized with mean ocean $\delta^{18}O_{sw}$ values for the Atlantic of 0.1117‰. Each model experiment was run for 900 years to achieve steady-state, and the steady state results were compared with observed modern day $\delta^{18}O_{sw}$. The model runs are repeated for different parameter combinations based on literature estimates.

Model tuning is used to identify realistic parameter values that generate results consistent with observed mean $\delta^{18}O_{sw}$ in the model's three Atlantic boxes as well as the $\delta^{18}O$ of atmospheric water vapor transport across 50° N. Additionally, sensitivity tests measure the effect of varying each parameter independently. Understanding the relationships between the model parameters and the model solutions will help to better understand the effects of atmospheric and ocean circulation changes on $\delta^{18}O$ in each box. For example, increasing overturning circulation lowers the $\delta^{18}O_{sw}$ gradient between the low and the high-latitudes. Increasing overturning and atmospheric flux together will work towards depletion in the high latitudes. Results of Mix (1992) give the reader an intuition about how the model works: As vapor flux increases the greatest changes in [^{18}O] are in the

low-latitude surface ocean as compared to the high-latitude surface ocean and the deep ocean (Mix, 1992). The low-latitude warm surface ocean $\delta^{18}O_{sw}$ changes more with respect to increasing vapor flux than do the high-latitude and deep boxes. (See Figure 4, below.)

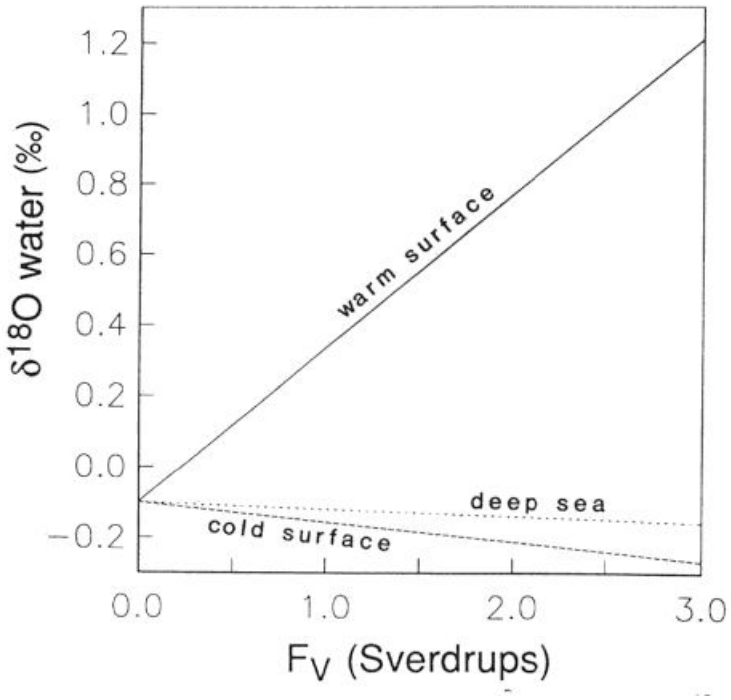

Figure 4 Increasing the vapor flux parameter shows a greater effect on the (warm) low latitude surface box than on the (cold) high latitude surface box.

3.4 Solution matrix and cost function

The number of values of the solution output matrix is determined by the increment size of the user input domain. The structure of the solutions matrix for each ocean reservoir is a 6-dimensional matrix because there are 6 input variables.

The fit produced by each set of parameter values is evaluated using a cost function. The cost function is the sum of the absolute values of the difference between the final model values for each box and the observed values for each box. The atmospheric $\delta^{18}O$ value is weighted less than the ocean reservoirs by a factor of 1000 because the ocean flux reservoirs are more well-documented than the atmospheric $\delta^{18}O$. (See section 4.2.) The best solution in the solution matrix is the one with the smallest cost (Figures 5-8, at end of chapter). An optimal solution is also required to reside within the given upper and lower search range for each variable.

cost_box1 = |**box1**(solutions for each combination of inputs) - **observed_value_box_1**|

cost_box2 = |**box2**(solutions for each combination of inputs) -**observed_value_box_2**|

cost_box3 = |**box3**(solutions for each combination of inputs) -**observed_value_box_3**|

cost_flux = |(**flux**(solutions for each combination of inputs)-**observed_flux_value)/1000**|

optimal_soln=

minimum_of_all_added_cost_values(cost_box1+cost_box2+cost_box3+cost_flux)

3-box model solution matrix cost function (1.4)

Because the model has 6 input parameters and 4 output reservoirs, it is likely that the model has more than one solution that will match observations. (This model is under-constrained). I graphed each of the input parameters against each other variable, looking for solutions that resided between each of the upper and lower boundaries for each input parameter (Figures 5-8).

4 Results for two high-flux experiments

4.1 Broad parameter range initial results

The first tuning attempt for the model included used parameter search ranges approximately 10% above and below each literature estimate for that parameter. Because of the computational cost of running a model with nested input values, I first ran wide-parameter searches with step sizes of one-fourth to one fifth of the total input domain apart. The $\delta^{18}O_{sw}$ values for each box during the final model year of each experimental model-run were stored in a six-dimensional solution matrix. Then from this matrix the cost function was used to select one set of optimal input parameter values (one value for each model variable).

Based on the location of the optimal solution within the cost function for each model run, I chose the values for the next experiment. For example, if one of the optimally tuned solutions yielded values at the low-end of the parameter's domain, then I chose a domain with a lower starting parameter value for the next experiment. A goal in tuning the model was to center each optimally tuned solution within the center of the input vector for each

parameter. Using the solution matrix, each variable was graphed against the other. The cost function optimal solution appeared as a diamond shape or diagonal line in the graphs (see Figure 5-8) with darker and cooler colors indicating the more desirable solution (with the least cost).

When I was able to narrow the search range, I then made the parameter incremental step sizes smaller, as small as 1/13 of the model domain, to improve the resolution of the model's solution for that run. In the initial tuning experiment I ran the model for a total of 113,400 different parameter combinations, which required a runtime of 120-160 minutes. If the optimal result was at either the lower end or the higher end of the parameter input vectors, I chose ~10 % higher (or ~10% lower) initial domains for the next experiment's modeled values with a narrower search field to fine-tune the experiment. Graphs of each variable plotted against the other helped me with the tuning method.

4.2 Very-High flux solution (experiment 1)

In the solution to experiment 1 (Table 1, column 1) all parameters selected by the cost function were within the edges of the parameter input domains indicating that the model found an optimal solution for each parameter given the search values. However, horizontal

mixing was within one step of the lower edge of the cost function.This solution was not further tuned because although overturning circulation was at the lower limit of realistic values (within the limits provided by stream-functions of overturning circulation (Kuhlbrodt et al., 2001), an increase in horizontal mixing would also decrease the difference (gradient) between the low and the high latitudes, requiring a further decrease in overturning circulation. An increase in overturning circulation would also require an increase in atmospheric flux, which is already much higher than expected. The misfit between model $\delta^{18}O_{sw}$ and observations for this tuning experiment are all very small; the largest misfit is in the high-latitude box at -0.0390‰, which is a difference of one-thousandth of a per mil from the observed value of -0.0402‰.

4.3 High-flux solution (experiment 2)

Because the first tuned solution had water vapor-flux values that were too high, a second search was created based on the idea of allowing overturning to reach its minimum for this experiment, allowing a higher flux for high-latitude vertical mixing than in the earlier experiment. The rationale was that this would allow the overall difference between the low and high latitudes to remain similar to the first experiment while allowing a

smaller water vapor-flux and a lower alpha value (more vapor fractionation to compensate for reduced flux). This solution is reported as experiment 2 (column 2) in Table 1, and has similar domain windows for parameters of water vapor-flux, overturning circulation, and alpha as experiment 1.

With the exception of horizontal mixing, each of the optimally tuned values resides within the cost function at least three increments above its lowest parameter value. (Alpha was tuned to within one value of the upper parameter input value). In this experiment, the targets were very closely matched for the low and the high-latitudes. The largest misfit was for the high-latitude box which was matched within eight ten-thousandths of a ‰ value at -0.0410 ‰ (-0.0402‰ is the target). However, the new atmospheric water vapor flux of 0.44 Sv is 79% of the global value of 0.56 Sv, which is still much too high for a model of the Atlantic Ocean.

5 Modified model with Arctic Flux

5.1 Additional freshwater transport from low to high latitudes

Because the model-estimated atmospheric flux values of the prior two experiments are too high (whole-earth instead of local Atlantic values), a third experiment was created by adding a low-to high latitude seawater trajectory to the model in addition to the overturning, mixing, and vapor transport parameters across 50° N. Physically, this represents the process of transport (loss) out of the low-latitude Atlantic into the Pacific Basin via vapor transport across the Isthmus of Panama and through the Southern Ocean, which returns to the high-latitude Atlantic via seawater flux through the Bering Strait. Additionally, river runoff into the Arctic Ocean is produced by water vapor transport outside of the longitude range of the Atlantic-only model. (See Figure 2 above for water bypass trajectory). These additional sources of depleted $\delta^{18}O$ to the high-latitude North Atlantic should help reduce the tuned atmospheric flux values to more realistic magnitudes.

Here I consider literature estimates for the modified low-to-high flux and $\delta^{18}O$ mass balance from the Arctic into the North Atlantic. This Arctic water has two sources: flow through the Bering Strait and river runoff.

5.2 Reported literature values and model values of cross-basin transport flux and flux through Bering Strait

The model uses 0.8 Sv of total flux through the Bering Strait, which is the value reported by Woodgate (2008). This net flow must be balanced by net water flux, the total flux out of the Atlantic into the Pacific (0.79 Sv) (Zaucker and Broecker, 1992).Transport out of the Atlantic Basin includes 0.1-0.3 Sv of water vapor transport across the Isthmus of Panama (Prange et al., 2010; Benway and Mix, 2004; Zaucker and Broecker, 1992; Richter and Xie, 2008; Fielder 2002; Lohmann 2003). Mean $\delta^{18}O_{sw}$ flux at the mouth of the Bering Strait is estimated as -1.1 to -0.98 ‰ (Cooper et al, 2006) and -1 +/-0.5 ‰ (Bauch et al, 1995). Flux at the mouth of Bering Strait varies from -0.75 to -1.5 ‰ at surface and -0.5 to -2 ‰ from 400 to 150 m depth (Cooper et al, 1997). I used a value of -1.1‰ for $\delta^{18}O_{sw}$ through the Bering Strait.

5.3 Runoff of freshwater into the Arctic Ocean and flow into Atlantic

Freshwater flux out of the Arctic into North Atlantic has two branches: the flux into the Fram Strait (to the East of Greenland from the Eastern Arctic) and West of Greenland around the island chain of the Canadian Arctic Archipelago (From the Western Arctic and Lincoln Sea), which together total 0.172 Sv +/-0.044 Sv (Alkire et al, 2017). Similarly, the Encyclopedia of Ocean Sciences reports 0.07 Sv of river runoff and 0.1 Sv of precipitation in the Arctic ocean (Rudels, 2009). The North American drainage divide for the Arctic Ocean is located at ~60° N on the Atlantic continental margin. Similarly, all rivers from northern Asia and the tip of Norway flow into the Arctic. Average runoff into the Arctic Ocean is -18 to -22 ‰ (Alkire et al, 2015).

5.4 Summary of additional Arctic fluxes

Flux transport of ~0.8 Sv and -1.1 ‰ is designated through the Bering Strait into the high-latitude North Atlantic, which is implicitly balanced by flux out of the low-latitude Atlantic basin and through the Pacific. Consistent with modern runoff and precipitation

values, a runoff flux value of 0.18 Sv flows into the Arctic ocean. A -20 ‰ $\delta^{18}O$ value simulates runoff/precipitation into the Arctic Ocean, which is transported to the North Atlantic (See sections 5.2.1 and 5.2.2 above). Each of these new parameters are held constant in the following experiment.

5.5 Results of model with Arctic flux

Because the two simple 3-box model solutions had water vapor-flux values on the high-end of the vapor flux input domain, a third experiment uses additional transport pathways between the low and high-latitude surface boxes with a search domain of lower flux values for the water vapor parameter based on the assumption that atmospheric flux in the Atlantic is ¼-⅓ of total global flux (Eakins and Sharman, 2010). Similar search parameters are used for overturning circulation, and alpha as the first two experiments. Thus with the additional transport values for freshwater flux between the high-and low-latitude surface boxes, a new hypothesis is that it would be possible to tune the atmospheric flux parameter to a fraction of its originally tuned value.

The results for this experiment were as follows (Table 1, column 3): Overturning was 5-7.45 Sv with an increment step size of 0.35 Sv (8 steps). The cost function found an

optimal overturning value of 5.4 Sv. Low-latitude vertical mixing was 1.6-2.6 Sv with an increment value of 0.14 Sv (8 steps) and yielded a low-latitude vertical mixing value of 1.89 Sv. High-latitude vertical mixing was 5-19 Sv with an increment step size of 2 Sv (8 steps). This experiment gave a high-latitude mixing value of 7 Sv. Alpha was given a parameter domain as 0.9840-0.9940 (0.0014) which yielded a tuned alpha value of 0.9874‰ (~11.8‰ less than the low-latitude value of the surface box). Horizontal mixing was evaluated from 1.85-7.85 Sv with an increment value of 0.85 Sv (8 steps). This gave an optimal horizontal mixing value of 1.85 Sv. Atmospheric flux was given a search domain of 0.92-0.155,with an increment of 0.009 Sv, and the cost function yielded a tuned value of 0.146 Sv.

The horizontal mixing resides on the low-edge of the cost function. High-latitude vertical mixing, alpha, and atmospheric flux reside at least 1 step away from the edge of the cost function. In this experiment, I also matched very closely the targets for the low and the high-latitude surface boxes. The largest misfit for this experiment was less than 0.002‰.

6 Discussion

6.1 Sensitivity tests for high-flux solutions

Contour plots of the cost function result from each pair of model parameters. These plots give us a sense of how the model parameters affect the final reservoir values in each experiment. Although the cost function finds the parameter value which yields the solution closest to the given literature or calculated reservoir value, the blue or darker colors in each solution graph indicate a possible continuum of solutions which are close in value to the optimal solution. There is at least one additional near-possible solution (in dark blue) in each of the three graphs with overturning and atmospheric flux (Very-High flux, High-Flux and Realistic Flux; Figure 5, Row 5). These indicate that as overturning increases, a small increase of atmospheric flux is required to achieve a solution with a similar cost. Increasing atmospheric flux brings more depleted waters to the high latitudes thereby allowing the fraction of alpha to more closely approach the value of one. Increasing (decreasing) atmospheric flux also increases (decreases) the estimated values

for alpha and horizontal mixing. (Increased vapor transport will bring increasingly depleted vapor across the high latitudes, allowing a less depleted alpha value or a lowered horizontal mixing value to achieve the same depletion value in the high-latitude surface box; Very-High flux, High-Flux and Realistic Flux; Figure 5, Row 4, 3). When decreased, the overturning and alpha parameters strengthen or enhance the gradient between the low and high-latitudes. For example, I was able to solve for a lower vapor flux value of 0.44 Sv in experiment 2 (Table 1 High-Flux) than the flux value of 0.62 Sv in experiment 1(Table 1 Very-High Flux) by allowing overturning to reach a lower value (5.4 Sv as compared to 5.7 Sv).

Graphs for alpha versus horizontal mixing produce cost function contours with a negative slope (Figure 6, row four). In these experiments, increasing alpha results in a decrease of horizontal mixing because less mixing is required to achieve the same gradient between the low and the high latitude boxes when the fraction alpha is close to the value of one (i.e., less water vapor fractionation).

However, some solution graphs indicate that for the given value of atmospheric flux, only one value of low or high-latitude mixing will yield an optimal solution, e.g., high latitude vertical mixing vs atmospheric flux (Figure 5, row one a b c). These plots have a

center value of darker color, with lighter colors emanating in a circular or diamond pattern around them. In these graphs there is not a linear shape in the cost function minimum, which would correspond to a variety of possible or near-solutions.

The model estimates of overturning are 5.4-5.7 Sv. Although AMOC flux is measured to be ~17 Sv at 1000 m at 26 °N (McCarthy et al., 2015), overturning in the 3-box model should reflect flux across the boundary between surface and deep boxes at 225 m. Tuned overturning fluxes in the model are similar to GCM stream functions of 6 Sv at 300 m depth (Kuhlbrodt et al, 2001).

Low-latitude vertical mixing estimates of the Atlantic model (1.89 - 2.5 Sv) are slightly lower than the literature estimates (at 3 Sv) suggesting that the model estimates are within real-world values (Webb and Suginohara, 2001). By increasing the vertical mixing between the low-latitude box and the deep ocean one can deplete the low-latitude surface box. Low-latitude vertical mixing yields a single target value rather (i.e. bulls-eye pattern) rather than a linear minimum when graphed against high latitude vertical mixing (Figure 8 row three a b c). This result indicates that the model system is sensitive to the values of vertical mixing; as the high-latitude vertical mixing parameter changes, the low-latitude mixing adjusts, so there is one relevant value for each change.

Modeled high-latitude vertical mixing (9-11 Sv) is similar to literature values of 9-12 Sv (Webb and Suginohara, 2001). However, high-latitude vertical mixing in 3-box models is traditionally less accurate because the parameter is often tuned to be much greater than realistic values (Toggweiler, 1999; Archer, 2000). Archer (2000) uses increased vertical diffusion or mixing between high-latitude and deep ocean to decrease the sensitivity of the model to changes in the high-latitude mixing. Increasing the mixing between the high-latitude surface box and the deep box has the effect of enriching the high latitude surface box (thereby decreasing the gradient between the low and the high latitude surface boxes.

High-latitude mixing in all three experiments yields one possible tuned value (bulls-eye pattern) with atmospheric flux (Figure 5, row 1, a,b, c) and overturning Figure 8, row 1, a,b,c). However, both the high-flux experiments (Table 2 columns 1 and 2) and more realistic low-flux experiment (Table 2 column 3) the high-latitude vertical mixing value is sensitive to the overturning value to which it is being compared. Overturning flux of 5.4 Sv yields a higher high-latitude vertical mixing parameter of 11 Sv as compared to the higher overturning flux in experiments (columns 1 and 3) of 5.7 Sv which yield lower high-latitude vertical mixing of 9 Sv. In an earlier experiment the high-latitude vertical

mixing term has a relatively higher input vector of 9-15 Sv (Figure 2); this experiment did not show the bulls-eye pattern that you described for all (other) high-latitude mixing graphs.

The modeled horizontal mixing term between basins is 1-1.85 Sv, which is similar in magnitude to the literature estimate of 3 Sv that comes from surface observations of Ekman transport in the Atlantic (McCarthy et al., 2014) at 26° N. Increasing the horizontal mixing between the two surface boxes has the effect of decreasing difference, or $\delta^{18}O_{sw}$ gradient, between low and high-latitudes (similar to the effect on overturning circulation). A lower overturning value will be required to achieve the same surface box values because increased overturning and increased alpha also decreases the gradient between low and high latitude boxes.

The target alpha value of 0.988 was determined from atmospheric transport values from an aGCM (Battisti, et al, 2014), and atmospheric $\delta^{18}O$ from the aGCM was used as one of the 'boxes' of the cost function. The modeled values for both flux experiments are quite close, at 0.9877 (high flux) and 0.9846 (low flux) or -11.46 and -14.61 ‰. Alpha generates a contour plot with a single, circular minimum when plotted against the vertical-mixing parameter in the realistic flux experiment but tends to appear linear in

graphs with a larger magnitude atmospheric flux (Figure 7, row 1 and 2). This means that a single value of alpha will generate the minimum in the cost function when high-latitude mixing is varied but the lower the atmospheric flux, the more sensitive the cost function will be to a single value of alpha. In contrast, alpha creates a positive-slope graph versus vapor-flux in both high-flux and low-flux experiments (Figure 5, row 4) and a negative-slope graph versus overturning in the three experiments (Figure 7 row 3). Increased vapor flux increases the $\delta^{18}O_{sw}$ gradient between the two surface boxes. Increasing alpha however, decreases the gradient between the two surface boxes. Thus as you increase (decrease) alpha, vapor flux must increase (decrease) to retain the same difference between the high and low latitude reservoir boxes. Increased vapor flux and increased overturning however, both work towards decreasing the gradient between the high and the low latitudes. Thus as you increase (decrease) overturning circulation, the value of alpha must decrease (increase) to maintain the same difference between the high and the low-latitudes.

6.2 Parameter interactions for realistic flux solution

The newer model that includes Arctic fluxes tunes to within two thousandths of a per mil for each of the two surface ocean reservoirs and a ten thousandth of a per mil for the deep ocean reservoir. Additionally, the atmospheric transport parameter was tuned to within a per mil for this experiment, which was about as accurate as the 'very high flux' experiment of the simpler model (Table 2, column 1). With the lowest of the 'realistic flux' experiments the model provided a solution to the three-box model which allowed a maximal gradient between the low and high latitudes while maintaining a lower atmospheric flux. In this case, optimal overturning was tuned to 5.7 Sv, and this value is within the modeled stream function values for overturning strength considering the depth of the surface boxes in the model which are 225 m deep (McCarthy et al., 2014).

The high-latitude vertical mixing term of 9 Sv in this model run, is the same as the 'highest flux' solutions of the prior experiment. The shapes of the high latitude vertical mixing graphs of the prior experiment indicated that there was one optimal value for high latitude vertical mixing experiment (Figure 5, row 1). However, unlike this bulls-eye

pattern the results graph of horizontal mixing vs overturning in Figure 6 shows a negative-slope relationship between overturning and horizontal mixing. The negative-slope relationship between horizontal mixing and overturning circulation, means that overturning must slow in response to an increase in horizontal mixing.

6.3 Multiple tuning solutions

A successful model solution includes tuned values which are as close to literature values as possible and will match each reservoir value to within the uncertainty of real-world observations. I was able to match two out of three reservoirs in each experiment to a ten-thousandth of a per mil. However, error in the dataset (LeGrande and Schmidt, 2006) is likely much larger because error correction on some of the constituent datasets in this series have been applied. These corrections vary from 0.14-1.0‰.

As another measure of uncertainty in the tuning targets, I measured the effect of changing the surface low latitude boundary: shifting the low-latitude surface boundary deeper by 25 m decreases the $\delta^{18}O_{sw}$ by 0.028‰ and shifting the depth boundary to 25 m shallower increases the $\delta^{18}O_{sw}$ of this reservoir by 0.026‰. Shifting of the low-latitude box up or down therefore, changes the target by ~ +/-3 %.

In the high-latitude box deepening the high-latitude boundary increases the $\delta^{18}O_{sw}$ of this reservoir by 0.038‰ and shoaling the high latitude depth boundary decreases the $\delta^{18}O_{sw}$ by 0.053‰. Deepening the boundary therefore decreases the target by -94% and shoaling the boundary increases the target by 132%.

However, lowering the deep reservoir depth boundary by 25 m decreases the value 0.007‰ and raising the depth boundary increases the $\delta^{18}O_{sw}$ by 0.008‰. Thus, shifting the deep box boundary up or down shifts the target by +/-10%.

Increasing the surface high-latitude northernmost boundary from 74° N to 78° N decreases the $\delta^{18}O_{sw}$ of this reservoir by 0.02‰. Conversely, decreasing the surface high-latitude northernmost boundary from 74° N to 70° N increases the $\delta^{18}O_{sw}$ of this reservoir by 0.04‰. The sensitivity of the model to the high-latitude boundary indicates that the choice of the northernmost boundary is important to the model structure; the high-latitude target of -0.04 changes by 50% to -100% with these sensitivity tests.

6.3 At least one viable solution

If the model had at least as many tuning targets as model parameters, it would be able to find at most one solution. However, with more model parameters than tuning targets, an infinite number of possible solutions exist. Because there were two more parameters than tuning targets it was hypothesized that the model would find more than one solution which would approach the criteria for a successfully tuned solution. Although the simple model found two discrete solutions which agreed with the $\delta^{18}O_{sw}$ target values to within thousandths of a per mil for each modeled reservoir (Table 1) (LeGrande and Schmidt, 2006), the atmospheric transport flux for solutions one and two (Table 1 columns 1 and 2) are too high. However, experiment 3, which included Arctic fluxes (Table 1 column 3) finds a solution which not only comes very close to the model tuning targets but also satisfies the need to tune the Atlantic model to within ¼-⅓ of global vapor flux. In the cost function contour plots of overturning, alpha, versus atmospheric flux (Figure 5 , rows 5 and 4, column 3) a continuum of solutions is possible for experiment 3. For example, as

one increases overturning, atmospheric flux also increases. As one decreases alpha, atmospheric flux decreases.

In graphs of low and high-latitude mixing versus atmospheric flux the modeled atmospheric flux value is constrained in each of the experimental runs (shown below) (Figures 5 rows 1 and 2, columns 1 2 3). Only one possible tuned value is possible for each vertical mixing term when graphed against atmospheric flux. However, the low-latitude mixing appears slightly more linear than the high-latitude mixing. The optimal values for high and low-latitude mixing differ between the runs where a very high flux value is chosen ([hi-lat] 9 Sv, [low-lat]1.85 Sv), from the runs where a high value is chosen ([hi-lat] 11 Sv, [low-lat]1 Sv) and as compared to the realistic run([hi-lat] 7 Sv, [low-lat]1.85 Sv) (Table 1) . It appears that a slightly higher horizontal mixing parameter is possible with a lower high-latitude vertical mixing flux because less mixing is then occurring with the deep ocean.

6.5 Can the model find a physically realistic solution?

The realistic flux solution shwed box model reservoir values were tunable to within a thousandth of a per mil (Table 1 column 3), While the model closely matched the literature values given for each parameter with the exception of vertical mixing in the low-latitude surface box. The tuned overturning circulation values of 5.4-5.9 Sv are smaller than the estimate of 17.2 Sv at 26° N (McCarthy et al., 2014). However, overturning varies with depth: In the CLIMBER part 2 model of intermediate complexity in the Atlantic latitudes of 45-60° N maximum overturning of greater than 20 Sv occurs in the Atlantic ocean at ~1000 m depth, but at a depth of 200 m, overturning is 6-10 Sv (Ganopolski et al., 2001). A two-dimensional model with the forcing parameters of freshwater flux, surface temperature, and wind stress shows maximum overturning of greater than 16 Sv in the Atlantic at 60° N at 1000m depth, but the surface 200m exhibit ~ 4-8 Sv of overturning strength from 40-60° N at ~200 m depth (Sevellec and Fedorov, 2011).

Modeled stream function values indicate that while maximum overturning likely occurs at 1000 m depth in the Atlantic, overturning circulation at ~200m depth or slightly

lower is in general less than 10 Sv (Ganopolski et al., 2001; Sevellec and Fedorov, 2011). The model overturning values at 225 m depth therefore likely do not reflect values for maximum overturning which occur at 1000 m depth (McCarthy et al, 2014). More boxes to separate flow above and below 1000 m would be needed to observe the total Atlantic overturning.

The optimal atmospheric flux values for the simpler model (0.47-0.64 Sv) are consistent with observed literature values of vapor transport across the northern high latitudes of 0.47-0.76 Sv (Zaucker et al., 1993), the lower of which is consistent with the GCM simulation of whole earth vapor transport across 50° N, (Battisti et al., 2014). However, the simple box model only represents the Atlantic basin. Atmospheric transport for the Atlantic likely represents one-quarter to one-third of vapor transport in the whole ocean since the Atlantic only contains a fraction of the water vapor transport across high latitudes. Therefore, the atmospheric flux values are likely too high in the first two experiments with the simple model.

To find realistic atmospheric transport, one would need to calculate just the transport of water vapor in the Atlantic across 50° N. The alpha value is constructed from the GCM data which was used to calculate alpha (Battisti et al., 2014), and therefore the fractionation

value of 0.988 may also be different for the Atlantic. Thus, because of model limitations as outlined above, one would not be able to achieve more accurate model tuning with more experiments with the simple model as it is currently configured. More boxes are needed to observe the total Atlantic overturning and more accurately modeled vapor flux would be needed to refine these experiments. However, experiment 3 with Arctic flux allows the simple model to be tuned to within realistic vapor flux for the Atlantic.

Table 2 Observed values compared to Experiment 1, Experiment 2
Alternate Table 2. Higher horizontal mixing flux values: Experiment 3

	observ values	param search range (step size)	Expt 1 (Very High Flux)	param search range (step size)	Expt 2 (High Flux)	param search range *Bering St=0.8 Sv, -1.1‰)* (step size)	Expt 3 *Realistic flux*
low-lat $\delta^{18}O_{sw}$	0.8363		0.8364		0.8366		**0.8348**
high-lat $\delta^{18}O_{sw}$	-0.0402		-0.0390		-0.0410		**-0.0425**
deep $\delta^{18}O_{sw}$	0.0736		0.0736		0.0736		**0.0737**
vapor $\delta^{18}O$ range	-10.8 (global)		-11.46		-14.61		**-11.75**
low-lat vertical mixing	1-3 Sv	1.6-2.58 (0.14)	2.2 Sv	1.6-2.6 (0.14)	2.5 Sv	1.6-2.6 (0.14)	**1.89**
overturn at 50° N, 225 m	6 Sv	5-7.45 (0.35)	5.7 Sv	5-7.5 (0.35)	5.4 Sv	5-7.5 (0.35)	**5.4**
hi-lat vertical mixing	9-12 Sv	5-19 (2)	9 Sv	5-19 (2)	11 Sv	5-19 (2)	**7**
vapor flux	0.12-0.15 Sv ¼ global	0.55-0.65 (0.014)	0.62 Sv	0.40-0.50 (0.02)	0.443 Sv	0.092-0.155 (0.009)	**0.146**
alpha		0.9860-0.996 (0.0014)	0.9877	0.9760-0.986 (0.0014)	0.9846	0.9860-0.9960 (0.0014)	**0.9874**
horizontal mix		1-7 (0.85)	1.85 Sv	1-7 (0.85)	1 Sv	1.85-7.85 (0.85)	**1.85**

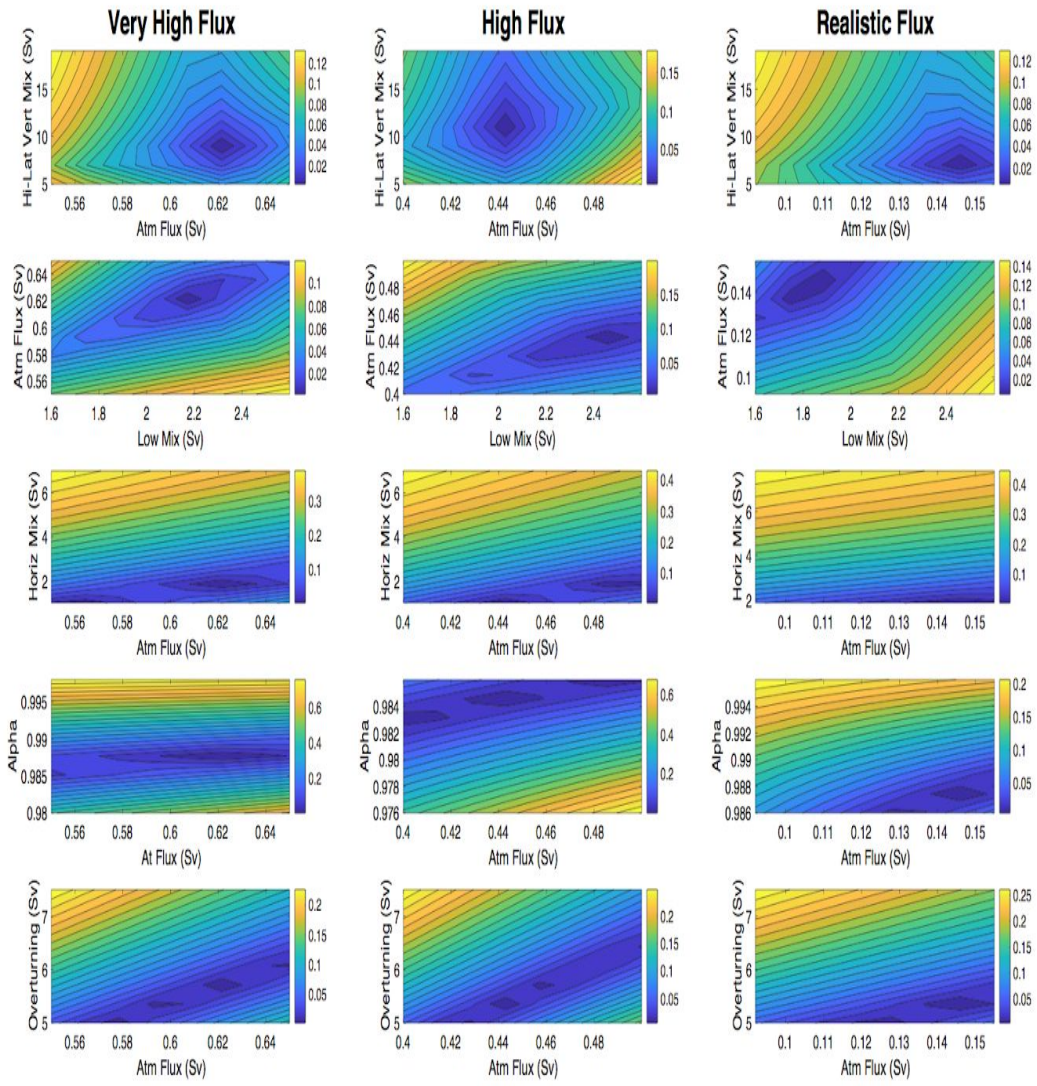

Figure 5 Experiments 1-3: Each variable graphed against atmospheric flux. Contours represent cost function value.

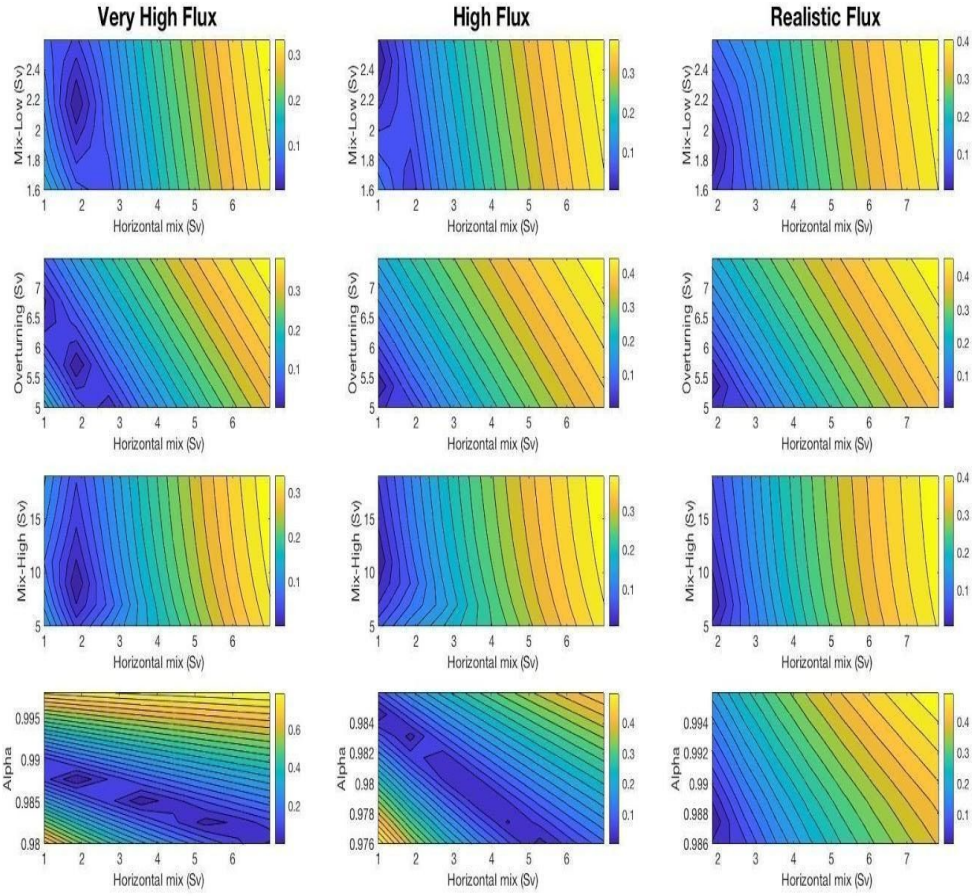

Figure 6 Very High flux experiment High Flux Experiment Realistic Flux: Horizontal mixing vs. low-latitude mixing, high latitude mixing, overturning, and alpha

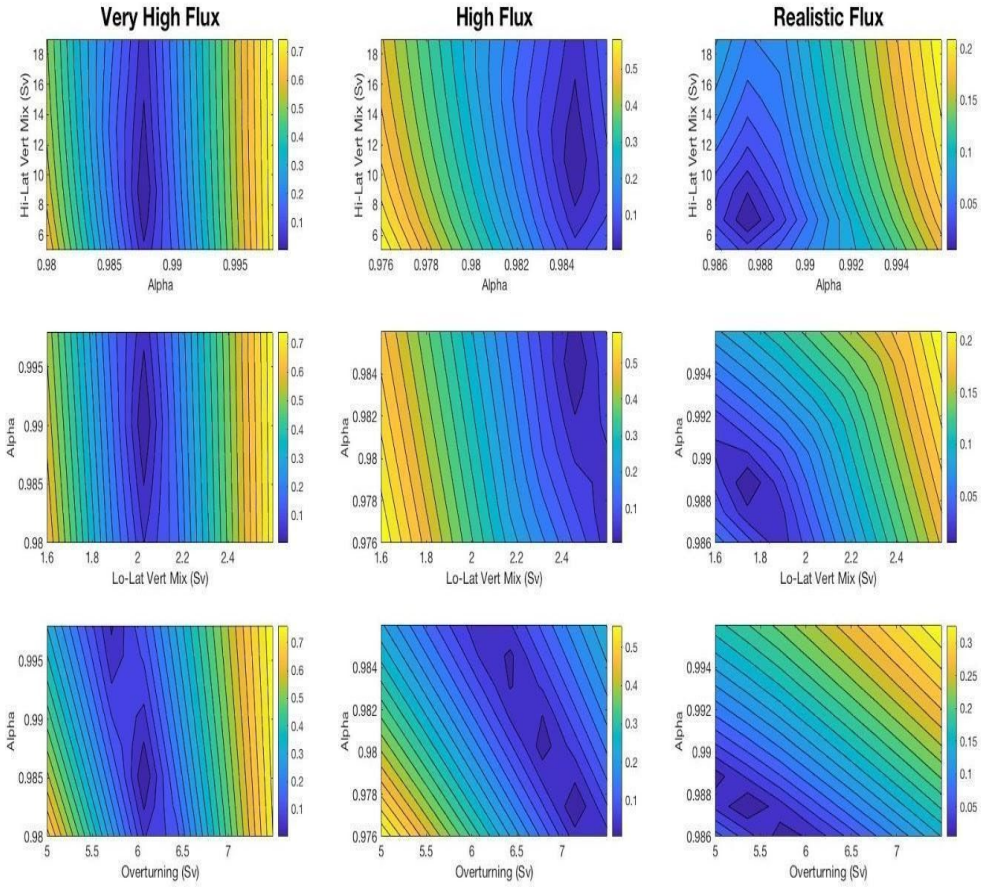

Figure 7 Very High flux experiment High Flux Experiment Realistic Flux: Alpha vs. High latitude vertical mixing, low latitude vertical mixing, and overturning

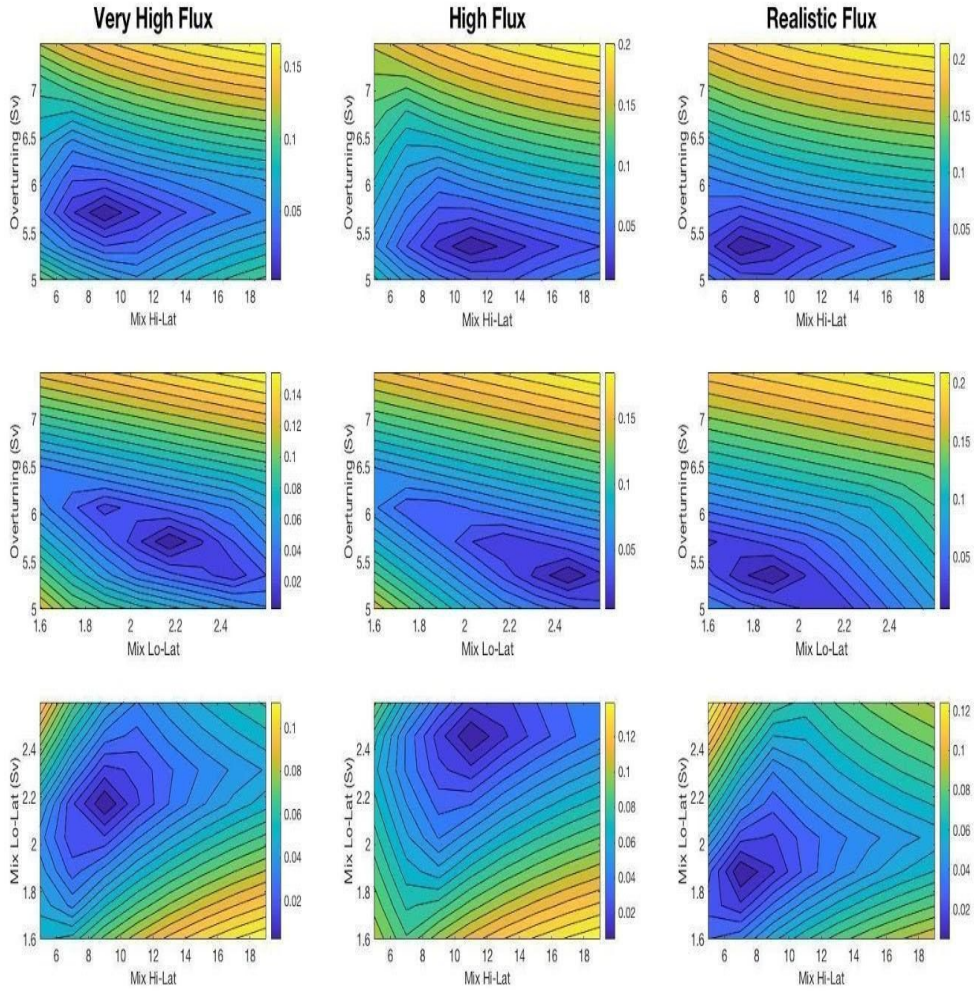

Figure 8 Very High flux experiment High Flux Experiment Realistic Flux: overturning vs. high latitude vertical mixing and low latitude vertical mixing

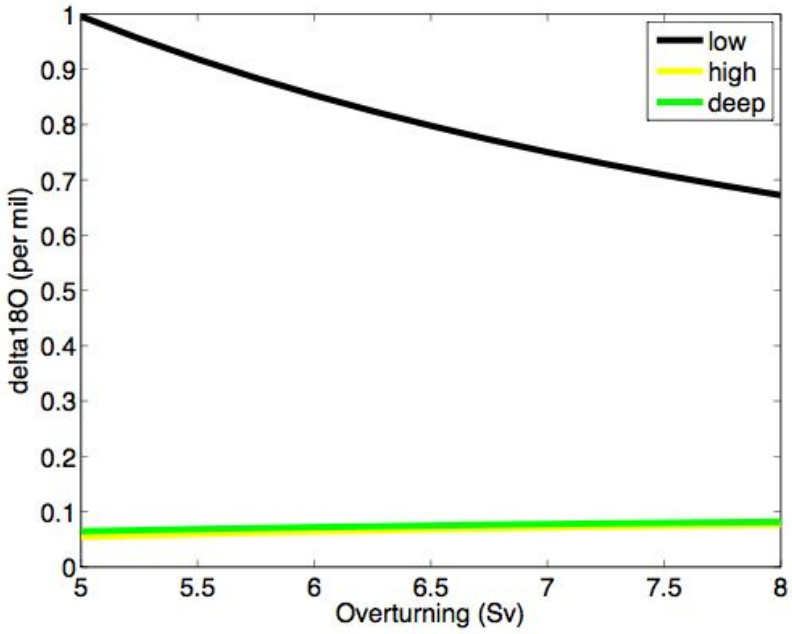

Figure 9 Increasing overturning decreases the gradient between low and high-latitude boxes

7 Conclusions

A three-box model of ocean circulation was created with a simple vapor transport from the low to the high-latitudes and a vapor fraction value. This model was able to accurately match each ocean reservoir value to within a thousandth of a per mil. Notably because the model is under constrained one can find multiple discrete solutions with differing amounts of water vapor transport which match the $\delta^{18}O_{sw}$ of all three ocean boxes to within a thousandth of a per mil for each reservoir. However, finding a tuned solution with realistic $\delta^{18}O_{sw}$ results and realistic parameter values requires the model to include terms for flux through the Arctic Ocean into the North Atlantic.

The model parameters have varying effects on the gradient between the low and high-latitude surface reservoir; these give the reader an intuition about how the model variables work. The vapor fractionation value alpha and the vapor flux value drive the depletion in the high-latitude $\delta^{18}O_{sw}$. With increasing overturning the low-latitude surface ocean reservoir changes more than the high-latitude reservoir and the deep ocean reservoir (Figure 9). Because increased (decreased) horizontal-mixing decreases (increases) the

gradient between the low and the high latitudes it also creates the need for a lower (higher) alpha value, or overturning, or atmospheric flux to compensate (See negative-slope graphs in Figure 6, row 4, for Very-High Flux, and High Flux experiments. High-latitude vertical mixing requires a single value of overturning circulation (bulls-eye pattern), (Figure 8, row one). Low-latitude vertical mixing values have a very slight negative slope relationship with overturning (Figure 8, row 2) (or slightly enhancing effect on the surface low-high gradient) because increased low-latitude vertical mixing will require slightly less overturning to achieve the same gradient between the low and the high latitudes.The effect is small because low-latitude vertical mixing is approximately 1/3 that of overturning.

Modeled overturning flux came close to the 6 (at 200 m depth) Sv of McCarthy et al., (2014); however, the boundary between shallow and deep boxes is too shallow to capture the maximum overturning flux achieved by high-latitude vertical mixing which occurs at 1000 m depth.

Low-latitude vertical mixing values of 1.7-2 Sv in the model are lower than the whole-earth estimates of 3 Sv Webb and Suginohara (2001), which is what might be expected for an Atlantic-only model. Values of low-latitude mixing, alpha, and atmospheric flux were tunable to within 1-2 Sv of literature values. The parameters of

atmospheric flux is tunable to ⅓-¼ of global flux across 50° N with additional bypass fluxes into the high-latitude surface Atlantic that represent flow through the Bering Strait and Arctic runoff.

Chapter 3 expands upon these results with the addition of a more realistic atmosphere that better simulates Rayleigh fractionation, with temperature-dependent alpha terms for both evaporation and precipitation, and accounting for the fraction of water vapor that rains out over the low latitude ocean.

8 References

Aagaard, K., and Carmack, E. C.: The role of sea ice and other fresh water in the Arctic circulation, J. Geophys. Res., 94, 14,485–14, 498, doi:/10.1029/JC094iC10p1448, 1989.

Alkire M., Morison J., Schweiger A., Zhang J., Steele M., Peralta-Ferriz C., Dickinson S.: A Meteoric Water Budget for the Arctic Ocean Journal of Geophysical Research, Oceans**,** vol: 122 (12) pp: 10020-10041 doi:/full/10.1002/2017JC012807, 2017.

Archer, D. E., Eshel G, Winguth A., Broecker W., Pierrehumbert R., Tobis M., Jacob R..: Atmospheric pCO_2 sensitivity to the biological pump in the ocean, Global Biogeochemical Cycles, 14(4), 1219-1230, doi: /10.1029/1999GB001216, 2000.

Battisti, D., Ding Q., Gerard, R..: Coherent pan-Asian climate and isotopic response to precessional forcing, J. of Geophy. Research, 119 (21), 11,997-12,020, doi:/10.1002/2014JD021960, 2014.

Baumgartner, A. and Reichel, E. World Water Balance: Mean Annual Global, Continental and Maritime Precipitation, Evaporation and Run-Off, Elsevier, Amsterdam, 1975.

Benway, H. M. & Mix, A. C.: Oxygen isotopes, upper-ocean salinity, and precipitation sources in the eastern tropical Pacific. Earth Planet. Sci. Lett. 224, 493-507, 2004.

Benway, H, Mix, A.: Using Oxygen Isotopes to Characterize Local Freshwater Balance and Trace the Origins of Precipitation in the Gulf of Panama, Eastern Tropical Pacific, Earth and Planetary Science Letters, 224 493 – 507, 2004.

Broecker, W. S.: Oxygen isotope constraints on surface ocean temperatures: Quaternary Research, v. 26, p. 121—134, 1986.

Broecker, W. S., Peng, T. H.: Carbon cycle: 1985, Radiocarbon, v. 28, p. 309-327, 1986.

Broecker, W.S., T.-H. Peng, J. Jouzel, and G. Russell: The magnitude of global fresh-water transports of importance to ocean circulation. Clim. Dyn., 4, 73-79 doi:/10.1007/BF00208902, 1990.

Chereskin, T. K., Rocha, C. B., Gille, S. T., Menemenlis, D., & Passaro, M.: Characterizing the transition from balanced to unbalanced motions in the Southern California current. Journal of Geophysical Research-Oceans, 124(3), 2088-2109. doi: /10.1029/2018jc014583, 2019.

Cooper, L.W., Whitledge, T.E., Grebmeier, J.M.,Weingartner,T.: The nutrient, salinity, and stable oxygen isotope composition of Bering and Chukchi Seas waters in and near the Bering Strait,Journal of Geophysical Research Atmospheres, 1021(C6):12563-12574, doi:/10.1029/97JC00015, 1997.

Craig, H., Gordon, L.I.: Deuterium and oxygen 18 variations in the ocean and marine atmosphere, in Tongiorgi, 15., ed., Stable isotopes in oceanic studies and paleotemperatures (Third SPOLETO Conference on Nuclear Geology: Pisa, Consiglio Nazionale Delle Richerche, Laboratorio di Geologia Nucleare, p. 9—130, 1965.

Doos, K. Coward, A.C.: The Southern Ocean as the Major Upwelling Zone of North Atlantic Deep Water, International WOCE Newsletter, 27, 3−5, 1997.

Dufresne, J., Foujols, M., Denvil, S. et al.: Climate change projections using the IPSL-CM5 Earth System Model: from CMIP3 to CMIP5, Clim Dyn 40, 2123–2165, https://doi.org/10.1007/s00382-012-1636-1, 2013.

Dwyer, G. S., Cronin, T. M., Baker, P. A., Raymo, M. E., Buzas, J. S., & Corrige, T.: North Atlantic Deepwater Temperature Change During Late Pliocene and Late Quaternary Climatic Cycles, Science, 270, 1347–1351, doi: /10.1126/science.270.5240.1347, 1995.

Eakins, B.W., Sharman, G.F.: Volumes of the World's Oceans from ETOPO1, NOAA National Geophysical Data Center, Boulder, CO, 2010.

Fielder, P. C.: Environmental change in the eastern tropical Pacific Ocean: review of ENSO and decadal variability, Mar. Ecol. Prog. Ser., 244: 265–283, 2002.

Fiedler, P. C.: The annual cycle and biological effects of the Costa Rica Dome, Deep Sea Res. Part I 49, 321-338, 2002.

deVries, P., Weber S. L.: The Atlantic freshwater budget as a diagnostic for the existence of a stable shut down of the meridional overturning circulation, Geophys. Res. Lett., 32, L09606, doi:10.1029/2004GL021450, 2005.

Eakins, B.W. Sharman G.F.: Volumes of the World's Oceans from ETOPO1, NOAA National Geophysical Data Center, Boulder, CO, 2010.

Emile-Geay, J., Cane, M. A., Naik N., Seager, A.C., Clement,vanGeen A. : Warren revisited: Atmospheric freshwater fluxes and ‘‘Why is not deep water formed in the North Pacific,’’ J. Geophys. Res., 108(C6), 3178, doi:/10.1029/2001JC001058, 2003.

Ganachaud, A., and Wunsch C.:The oceanic meridional overturning circulation, mixing, bottom water formation, and heat transport. Nature, 408, 453–457, 2000.

Gebbie, G.:How much did Glacial North Atlantic Water shoal? Paleoceanography, 29(3), 190-209, doi: /10.1002/2013PA002557, 2014.

Jansen, M.F., Nadeau L.: A Toy Model for the Response of the Residual Overturning Circulation to Surface Warming. J. Phys. Oceanogr., 49, 1249–1268, doi:/10.1175/JPO-D-18-0187.1, 2019.

Jones, E.P., Anderson, L.G., Swift, J.H..: Distribution of Atlantic and Pacific Waters in the Upper Arctic Ocean: Implications for Circulation, Geophysical Research Letters 25(6), doi/10.1029/98GL00464, 1998.

Köhler, P., Fischer, H., Munhoven, G., Zeebe, R.E.,: Quantitative interpretation of atmospheric carbon records over the last glacial termination, Global Biogeochemical Cycles, 19,. GB4020, doi:10.1029/2004GB002345, 2005.

Köhler P., Fischer H., Schmitt J.: Atmospheric δ13CO2 and its relation to pCO2 and deep ocean δ13C during the late Pleistocene, Paleoceanography vol: 25, doi:/10.1029/2008PA001703, 2010.

Kuhlbrodt, T., Titz, S., Feudel, U. et al.: A simple model of seasonal open ocean convection, Ocean Dynamics 52**,** 36–49, doi: /10.1007/s10236-001-8175-3, 2001.

Kutzbach, J., Guettar, P.: The Influence of Changing Orbital Parameters and Surface Boundary Conditions on Climate Simulations for the Past 18,000 Years, Journal of the Atmospheric Sciences, 43(16), 1726, 1986.

Lachniet M.S., Patterson, W.P., Burns, S. Asmerom, Y , Polyak V.: Caribbean and Pacific moisture sources on the Isthmus of Panama revealed from stalagmite and surface water $\delta^{18}O$ gradients, doi:/0094-8276/07/2006GL028469, Copyright 2007 by the American Geophysical Union.

Lawrence J.R., Gedzelman S.D.,Dexheimer D., Cho H.-K.,.Carrie G D., Gasparini R.,Anderson C.R.,Bowman K.P., Biggerstaff M.I.: Stable isotopic composition of water vapor in the tropics Journal of Geophysical Research, Vol. 109, D06115, doi:10.1029/2003JD004046, 2004.

Leduc, G.,Vidal, L., Tachikawa, K., Rostek, F., Sonzogni, C. Beaufort, L. Bard, E.: Moisture transport across Central America as a positive feedback on abrupt climatic changes, Nature, doi:/445. 908-11. 10.1038/nature05578, 2007.

LeGrande, A.N., Schmidt, G.A., Global gridded data set of the oxygen isotopic composition in seawater, Geophys. Res. Lett., **33**, L12604, doi:/10.1029/2006GL026011, 2006.

Lohmann, G. , Atmospheric and oceanic freshwater transport during weak Atlantic overturning circulation. Tellus A, 55: 438–449, doi:/10.1034/j.1600-0870.2003.00028.x, 2003.

Manabe, S. & Stouffer, R. J.: Two stable equilibria of a coupled ocean-atmosphere model, J. Clim. 1, 841–866, 1988.

Majoube, M., Fractionnement en oxygene-18 et en deuterium entre l'eau et sa vapeur. J . Chin,. Phys., 68, 1423- 1436, 1971b.

McCarthy, G.D., Smeed, D.A., Johns, W.E., Frajka-Williams E., et al.., Measuring the Atlantic Meridional Overturning Circulation at 26 N, Progress in Oceanography, 130, 91-111, doi: /pii/S0079661114001694, 2015.

Mix, A, Constraints on timing and extent of ice-growth events (120-65 ka): Special Paper, Geological Society of America, 270, The Last Glacial-Interglacial Transition, Peter D. Clark, ed., pp. 19-30, doi: /10.1594/PANGEA/836033, 1992.

Oort, A., Global Atmospheric Circulation Statistics, 1958–1973. NOAA Professional Paper 14, 180, 1983.

Östlund, H. G., and Hut, G., Arctic Ocean water mass balance from isotope data, *J. Geophys. Res.*, 89(C4), 6373– 6381, doi:/10.1029/JC089iC04p06373, 1984.

Prange M., Steph S., Liu H., Keigwin L.D., Schulz M.: Hydroclimatic Variability in the Panama Bight Region During Termination 1 and the Holocene M. Schulz and A. Paul (eds.), Integrated Analysis of Interglacial Climate Dynamics (INTERDYNAMIC), SpringerBriefs in Earth System Sciences, doi:/10.1007/978-3-319-00693-2_11, 2010.

Richter, I., Xie S. P.: On the origin of equatorial Atlantic biases in coupled general circulation models.Climate Dyn.,31, 587–598, 2008.

Roche, D. M.: $\delta^{18}O$ water isotope in the *i*LOVECLIM model (version 1.0) – Part 1: Implementation and verification, Geosci. Model Dev., 6, 1481–1491, doi: /10.5194/gmd-6-1481-2013, 2013.

Rudels, B., Marnela M., Eriksson P. : Constraints on Estimating mass, heat and freshwater transports in the Arctic Ocean: An exercise, in *Arctic-Subarctic Ocean Fluxes*, edited by R. R Dickson, J. Meincke, and P. Rhines, pp. 315– 341, Springer, Dordrecht, Netherlands, 2008.

Sarmiento, J. L. Toggweiler, J. R.: A new model for the role of the oceans in determining atmospheric PCO_2 , Nature, 308, 621–624, doi:/10.1038/308621a0, 1984.

Schmitt,R.W., Bogden, P.S., Dorman, C.E.: Evaporation minus Precipitation and Density Fluxes for the North Atlantic*, Journal of Physical Oceanography, Vol.(19) pp.1208-1221 doi:/10.1175/1520-0485, 1989.

Schmitz, W. J., and McCartney, M. S.: On the North Atlantic Circulation, *Rev. Geophys.*, 31(1), 29– 49, doi:/10.1029/92RG02583, 1993.

Sévellec, F., Fedorov, A.V.: Stability of the Atlantic meridional overturning circulation and stratification in a zonally averaged ocean model: Effects of freshwater flux,.... Deep-Sea Research II, doi:/10.1016/j.dsr2.2010.10.070, 2011.

Talley, LD.: Freshwater transport estimates and the global overturning circulation: Shallow, deep and throughflow components. Progress in Oceanography. 78:257-303, 2008.

Toggweiler, J R., Samuels B.L., On the ocean's large-scale circulation near the limit of no vertical mixing. Journal of Physical Oceanography, 28(9), 1832-1852, 1998.

Toggweiler, J.R. and Sarmiento, J.L.: Glacial to Interglacial Changes in Atmospheric Carbon Dioxide: The Critical Role of Ocean Surface Water in High Latitudes. In The Carbon Cycle and Atmospheric CO_2: Natural Variations Archean to Present (eds E. Sundquist and W. Broecker). doi:/10.1029/GM032p0163, 2013.

Toggweiler, J.R..: Variation of atmospheric CO 2 by ventilation of the ocean's deepest water, Paleoceanography, 14(5), 571-588, doi/10.1029/1999PA900033, 1999.

Wallmann, K.: Phosphorus imbalance in the global ocean? Global Biogeochem. Cycles, 24, GB4030, doi:/10.1029/2009GB003643, 2010.

Webb, D. J., Suginohara N.,Vertical mixing in the ocean, Nature, 409, 37, 2001.

Weber, S. L., Drijfhout S. S.: Stability of the Atlantic Meridional Overturning Circulation in the Last Glacial Maximum climate, Geophys. Res. Lett., 34, L22706 doi:/10.1029/2007GL031437, 2007.

Woodgate, R. & Aagaard, K.: The Freshwater Flux to the Arctic via the Bering Strait. AGU Fall Meeting Abstracts, 2004.

Woodgate, R. A., Weingartner, T., and Lindsay, R..: The 2007 Bering Strait oceanic heat flux and anomalous Arctic sea‐ice retreat, Geophys. Res. Lett., 37, L01602, doi:/10.1029/2009GL041621, 2010.

Wunsch, W., Ferrari, R..:Vertical Mixing, Energy, and the General Circulation of the Oceans, Annu. Rev. Fluid Mech.. 36:281–314. doi: /10.1146/annurev.fluid.36.050802.122121, 2004.

Zaucker F., Stocker, T., Broecker, W., :Atmospheric freshwater fluxes and their effect on the global thermohaline circulation,Journal of Geophysical Research, 99(C6), 12443–12457 doi:/10.1029/94JC00526 , 1997.

Zaucker, F., Broecker, W.S.: The influence of atmospheric moisture transport on the fresh water balance of the Atlantic drainage basin: GCM simulations and observations. J. Geophys. Res. 97, 2765–2774, 1992.

Appendix A

4. Model Methods

4.2.1 PMIP3 Models

The PMIP project started over 20 years ago as a way to coordinate and compare complex model outputs to define the drivers of climate change, to coordinate and synthesize paleo-proxies and to evaluate the climate outputs of coupled atmosphere-ocean general circulation models. We calculated model means of evaporation and precipitation from 90° S to 90° N in 9 Holocene-PMIP3 Holocene and LGM model-pairs before we chose 3 models for our model mean (*Dufresne et al., 2013* (Institut Simon LaPlace CM5A); *Jungclaus et al., 2013* (Max Planck Institute Earth System Model)); *Voldoire et al., 2011* (CNRM-CM5)). The models chosen for the final compilation filled the requirement that the cumulative evaporation minus precipitation from 90° S to 90° N summed to a value close to zero (less than or equal to 0.07) Sv because our simple model conserves mass. Three *PMIP3* model experiments are run as pre-industrial controls set in 1850 with boundary conditions of 260 ppm CO2, year 1850 insolation parameters, and vegetation

according to model specification; experiments at the LGM were initialized with orbital parameters of 21 ka, CO2 of 185 ppm, specified ice sheet forcing and river pathways consistent with ice sheet forcing.

Originally, eight model pairs (LGM, Holocene) were included in this mean but models included in the final model mean are models whose cumulative evaporation minus precipitation from 90° S to 90° N sum close to zero (less than +/-0.07 Sv).

4.2.2 Evaporative flux

Evaporative flux in the low-latitudes completely supplants the flux parameter from the low to the high latitudes in the model described in Chapter 2. Evaporation flux (E) in m^3 per second is calculated from 30°-50° N in the subtropical Atlantic for the 3 PMIP3 models listed above. To calculate the multi-model means we create an annual mean from each model's monthly evaporation and precipitation flux in kg/m^2s^2: the function reads each model's monthly mean in grid-matrix format (taking into account the number of days in each month) and concatenates the data into a consecutive 3-dimensional matrix : (latitude by longitude by month). A second function takes the height of the horizontal latitude bands as determined by each model's grid size (which vary from 1.4 to 2.8 degrees in height) and

determines the amount of global flux by sending the area to a function which multiplies the flux in each grid cell by the area in each grid cell. The total volumetric flux is then determined for each latitude band specified by the function. A final function determines an idealized latitude band area based on a spherical Earth and adjusts the model's volumetric flux in Sv according to the percent of the idealized total it represents. Mean evaporative flux in the modern and LGM is calculated from an average of the maximum evaporative flux (model means of evaporation from 30°-50° N) and minimum evaporative flux (model means of area weighted evaporation minus precipitation *(E-P)* from 30°-40° N plus *E* from 40°-50° N). We divide by 4 in order to calculate the approximate area of evaporation in the Atlantic which comprises ~¼ of the global area at these latitudes. We then divide by 10^6 to convert to Sv flux.

Figure 7 Calculation of Evaporative and Preciptiative flux in model mean

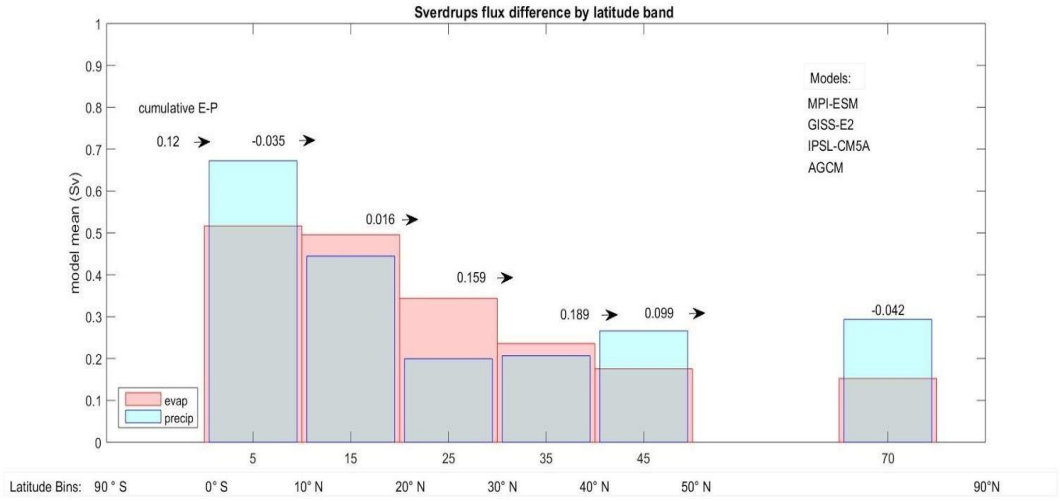

Figure 7 Cumulative E-P flux from 90°S-90°N to determine E-P error in model run averages. Bins are in increments: 90°S-0°S, 0°N-10°N, 20°N-30°N, 30°N-40°N, 40°N-50°N 50°N-90°N. The values of flux in this graph are divided by 4 in order to account for the flux in the Atlantic only.

4.2.1 Water vapor fractionation

The equation which describes the Rayleigh fractionation associated with the export of water vapor to the high latitudes, $R=R_0*f^{\alpha-1}$, is the total expression of alpha of depletion in

the newer 3-box model described here. This expression was first presented by Craig and Gordon, (1965) and describes the mechanical distillation of the oxygen isotope ^{18}O in surface seawater as a function of evaporation and vapor transport to the northern latitudes. The variable R_0 represents the ratio of $^{18}O/^{16}O$ in the evaporative flux which has previously been depleted by the low-latitude depletion of evaporation called alpha 1*(α1)*. The variable *R* is the $^{18}O/^{16}O$ of vapor after a fraction of the initial vapor has been removed by condensation (alpha 2*(α2)*) in the low-latitudes, such that *R* is the ratio in the water vapor that is transported across 50° N, the boundary between the low and high-latitude surface boxes in our 3-box model. We subtract 1 from the numerical value of **α2** to provide the depletion factor.

To calculate our fraction, we assume the majority of vapor transported across 50° N comes from between 30° and 50° N. Although precipitation dominates the Atlantic basin in the equatorial and high-latitudes, the narrowness of the Atlantic makes it a mainly evaporative basin in the middle and low- latitudes (Schmitt et al, 1989).The push and pull of the low pressure system over Iceland and the high pressure system over the Azores create a repeating flux of vapor transport from the low-to the high latitudes in the Atlantic .

The calculation of the mean evaporative transport is described in section 4.1.1. The total transport flux across 50° N is the amount of evaporation in the low latitudes multiplied by the fraction of transport. This fraction is comprised of vapor import across the high latitudes divided by evaporation in the low latitudes. This calculation will be discussed fully in section 4.1.3 below:

4.2.3 Fraction of water vapor export to high latitudes

The fraction ***(f)*** (between zero and one) regulates the amount of vapor transport to the high-latitudes from the low-latitudes between 30° N-50° N. The values of these fractions at the LGM and the modern are determined from separate modern and LGM runs of the four/three Paleoclimate Intercomparison Project Models (PMIP3) described in the evaporative flux above: (*Battisti, 2014* (isotope enabled atmospheric GCM); *DuFresne et al., 2013* (Institut Simon LaPlace CM5A); *Jungclaus et al., 2013* (Max Planck Institute Earth System Model)); *Voldoire et al., 2011* (CNRM-CM5)). The fraction was determined from the mean of low-latitude of evaporation described in section 4.4.1 and the average of vapor import over 50° N:

fraction = average (vapor export over 50° N+vapor import over 50° N)mean of minimum and maximum evaporative flux from 30°-50° N as described in section 4.1.1

We use the average of the vapor export from 90° S-50° N (*low-latitude E-P*) and vapor import into the high latitudes 50° N-90° N (*high latitude (E-P*) as our vapor export in the fraction. This gives us a fraction value of approximately 0.40 for the modern (Table A below) which is close to our estimates from sensitivity tests that we performed (See supplement S1). Our transport flux of 0.12 Sv is the evaporation flux in the low latitudes multiplied by the fraction of transport.

Fraction of transport determined from evaporative and transport flux in model means of modern above (white) and LGM below (green). The mean vapor import over 50° N comes from the average of 2 calculations: (1) the mean of the PMIP3 *E-P* from 90° S-50° N *and* (2) the mean of PMIP3 *E-P* from 50° N-90° N.

Table A Calculating Modern and LGM vapor transport and fraction of export across 50° N

	90-50° N	Export flux across 50° N	Fraction
Modern	0.31 Sv	0.11 Sv	0.36
LGM	0.26	0.079 Sv	0.27

4.3.2 Temperature dependence

The new parameters *(α1 and α2*) in Chapter 3 supplant the simple fractionation value alpha (**α**) from the low-to the high latitudes in Chapter 2. Low-latitude vapor fractionation of $\delta^{18}O_{sw}$ *(α1)* is dependent on the low-latitude sea surface temperature of the evaporative flux (Vachon, 2010). We use an equation by Majoube, (1971) to translate SST to α1:

$$\frac{1}{exp(\frac{1137}{T})-exp(\frac{0.4156}{T^2})-0.0020667} \quad (1)\ \text{Majoube, (1971)}$$

We flip this expression to determine the alpha of condensation *(α2)*:

$$exp(\frac{1137}{T}) - exp(\frac{0.4156}{T2}) - 0.002066 \qquad \text{(2) Majoube, (1971)}$$

In this case alpha 2 is greater than 1 and less than 2.

To generate the SST of evaporation, we create a model mean of SST in the low latitudes which we use in both our LGM and modern model runs:

This SST temperature of evaporation calculation has 2 parts: first an area-weighted mean temperature from all 4(3) models is calculated in a patch from 30-50° N (Flux patch areas: (*30° N-40° N*, *10° W-76° W* and *40°-50° N*, *10° W-64 °W*)).

Second, a *PMIP3* model mean of temperature weighted by evaporative flux was calculated in the low-latitude surface Atlantic. Calculation of the total evaporative flux was described in section 4.1.1. The flux-weighted temperature calculation described below is the average of the calculation of each model's mean temperature weighted by the evaporative flux described in section 4.1.1 :

[(mean Temp of 30-40°)*(total evap flux of 30-40°N)+(mean Temp of 40-50° N)*(total evap flux of 40-50° N)]/[(total evap flux of 30-40°N)+(total evap flux of 40-50° N)].

Temperatures (supplement S2) given for low-latitude temperature of evaporation are generated by weighting the mean temperature of the patch by the evaporative flux from 30-50° N .

The alpha 1 determined by 17° C (290 K) in the modern low-latitude evaporation translates into 14° C (273 K) in the **α2** of the vapor of condensation which is transported to the high latitudes. Similarly, the alpha 1 at the LGM was determined by a 13 C (287 K) low-latitude temperature of evaporation, translating to a 10 C (284 K) temperature of precipitation in the high latitudes (**α2**).The calculation on three PMIP3 models run in the LGM configuration yields an estimated temperature of evaporation for the Last Glacial Maximum of 10° C (283 K) and 7° C (280K) in the **α2** of the vapor of condensation which is transported to the high latitudes.(*Dufresne et al., 2013* (Institut Simon LaPlace CM5A);

Jungclaus et al., 2013 (Max Planck Institute Earth System Model)); *Voldoire et al., 2011* (CNRM-CM5)).

Water vapor fractionation of $\delta^{18}O_{sw}$ in the vapor transport flux alpha 2 (**α2)** was determined from an inversion of the same equation used to calculate alpha 1(**α1**) but at 3 degrees cooler (Majoube, 1971; Vachon 2010). (Because **α1** and **α2** are both a function of low-lat SST, they do not increase the number of parameters relative to the single alpha (**α)** parameter used in Chapter 2).

Appendix B

4.3 Ocean Circulation Parameters

The 3-box reservoirs are a simplification of complex flux systems in the ocean; the latitude of the ocean basin (Coriolis parameter and strength of insolation) and the shape of the Earth's topography at the sea floor (bed friction) determine the total strength and direction of real-world ocean flux.

4.3.1 Estimates for the LGM horizontal mixing surface flux

Waelbroeck et al., (2014) suggests slower mixing in the surface ocean at the LGM was due to less advection of salty waters northward causing enrichment of tropical $\delta^{18}O_{sw}$. A complex model reports 0.5 Sv of northward transport at 10° North and 0.3-0.4 Sv at 34° North (Ballarota et al, 2014). Theories about changes in horizontal mixing at the LGM rely on a more generally slowed circulation due to ocean density changes. However, an inverse model for LGM and present day indicate Eckman transport of approximately 1 Sv in both eras (error: seasonally + 5 Sv in the modern ,+/- 1 Sv LGM) (Gebbie and Huybers, 2017).

Although gyre flux in the surface high latitudes may reach upwards of 5 Sv in the North Atlantic, we keep a modern horizontal flux of 2 Sv for consistency of the tuned version of the model in chapter 2, which must remain at 2 Sv for the balance of the other parameters in the model, including atmospheric flux.

Because literature estimates of horizontal flux in the surface ocean are varied and range from 2-5 Sv in the modern surface ocean above 500 m and may be less than one Sv at the LGM we maintain a moderate mixing parameter of 2 Sv at the LGM for model simplicity.

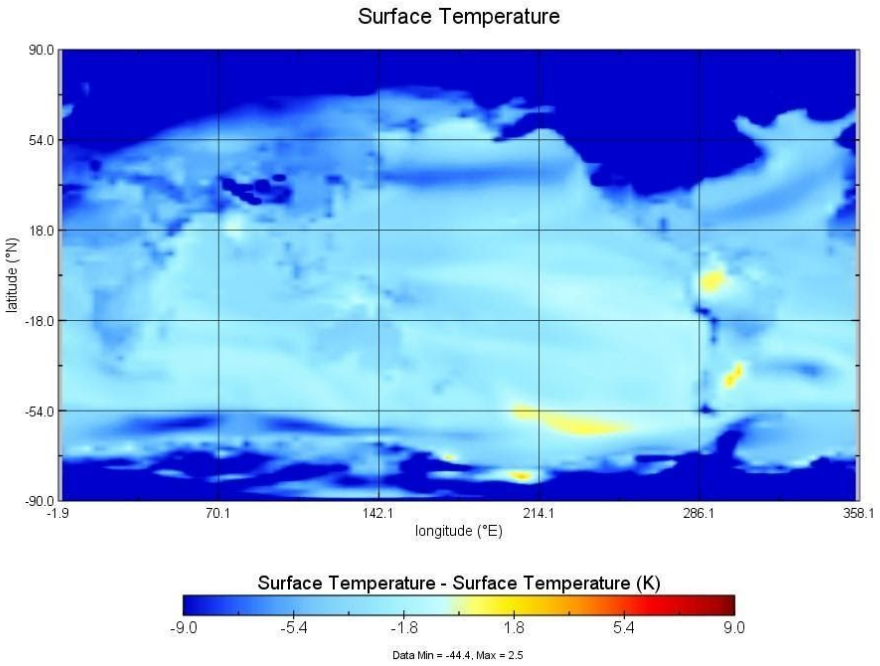

Figure 7 Calculated Atlantic surface temperature anomaly in September from model run of LGM-Modern in Model Institut Simon LaPlace CM5A.

4.3.2 High Latitude Vertical mixing in the modern and LGM

We derive our tuned modern high-latitude vertical mixing value of 7 Sv which is close to literature estimates of 9-12 Sv in Chapter 2. We define our LGM vertical mixing strength similar in magnitude to vertical mixing in a GCM of 3.4 Sv (~0.5*Modern) (Jansen, 2010) and sensitivity tests on our modern parameter: 0.8*Modern=5.6 Sv and 0.6*Modern =4.8 Sv.

4.3.3 Low-Latitude Vertical Mixing as compared to the LGM

Jansen (2014) reports that modern mixing below 300 m depth in the global ocean is half that of the LGM. The reason for increased low-latitude vertical mixing is due to decreased heat flux from the low-latitudes to the high latitudes (Oka, 2009). This may also be due to an increased estimate of poleward heat flux (Burke et al, 2014). Low-latitude heat transport could have been up to 20% greater than modern to 20% lower than modern depending on basin salinity dynamics and vertical mixing dynamics. We therefore modify our tuned low-latitude vertical mixing in the Modern of 3.5 Sv to 1.75 Sv in the case where low-latitude heat flux is increased at the LGM.

4.3.4 LGM overturning flux

There are varied estimates as to the strength of overturning circulation at the LGM, from stronger than that of the modern to almost nonexistent (Oppo and Curry, 2012). Therefore we chose sensitivity tests for overturning circulation at 60% and 80% of modern. However, we do not increase the overturning strength to that above modern, as surface cooling which drives deep water formation and overturning flux in the Atlantic will have reached steady-state; increased brine rejection will occur until cooling reaches a minimum, creating an increased deep-ocean stratification which then slows the inter-hemispheric overturning (Jansen, 2017).

4.3.5 Bering Strait and Arctic runoff

Because the Bering Strait was likely completely closed at the LGM, these experiments are likely not realistic during the coldest period of the LGM when the land-bridge was present due to lowered sea level.

It is likely that Arctic runoff was less at the LGM than today because of colder temperatures and the extent of the Laurentide ice sheet. Sedimentation rates and $\delta^{18}O$ of

calcite in planktic foraminifera indicate that surface flux (including runoff) into the Arctic may have varied by geographical location: According to Nørgaard-Pedersen et al., (2003), there were three distinct zones within the Arctic which influenced surface ocean flux and therefore freshwater runoff:

an open region within the Fram Strait (lat long) including calving and meltwater from the Barents ice sheet, an intermediate region at approximately 84-85 N consisting of ice cover which breaks up only occasionally, and a central Arctic ice cover which blocked the Atlantic from reaching the Arctic via the Barents sea and also reduces sedimentation rates and therefore runoff.

High sedimentation rates occurred in the Northern Barents Sea and off of Northeast Greenland indicating that high productivity occurred and therefore ocean flux occurred along the continental margin of the Barents Sea; Atlantic waters flowed northward into the Arctic at the LGM (Kniess et al, 1999). Rosell-Mele and Koc (1997) suggest that sediment cores from these sites may even contain lake sediment suggesting continental runoff at the LGM. However, from the Fram strait northward, and north of 85 N, sedimentation reduces to nearly zero suggesting increasing ice cover through the Fram strait northwards into the Arctic ocean (Nørgaard-Pedersen et al., 2003).

Supporting evidence shows enriched calcite in cores from the mid-ocean ridge in the Arctic (Gakkel ridge, 84°N, 11°E) and in the Nordic sea from the Fram Strait (84.5°N, 9°W), suggesting that these areas were not affected by depleted runoff during the coldest period of the last glaciation.

Supplement (Ch 3):

Cost function for each workspace:`

```
clear all
close all

c=load('matlab_ex_1_ch_2.mat')
j=load('matlab_ex_2_ch_2')
k=load('matlab_exp_3_ch_2_26_19_19h')%
```

```
%% observed
vapor_d18_value=-10.8%
low_lat_obs=0.8363;%proxy data LeGrande & Schmidt North Atlantic
hi_lat_obs=-.0402;%volume weighted average
deep_oc_obs=0.0736;
f_obs=vapor_d18_value;
observational_data=[low_lat_obs,hi_lat_obs,deep_oc_obs,f_obs]
```

```
%%  cost functions for each workspace

c.cost_box_1=abs((c.box1(:,:,:,:,:,:))-(low_lat_obs));%cost evaluation for each box
c.cost_box_2=abs((c.box2(:,:,:,:,:,:))-(hi_lat_obs));
c.cost_box_3=abs((c.box3(:,:,:,:,:,:))-(deep_oc_obs));
c.cost_fr=abs((c.boxf(:,:,:,:,:,:))-(f_obs));
ccost=c.cost_box_1+c.cost_box_2+c.cost_box_3+c.cost_fr/1000;%Add the cost for each box for each input value
```

```
%%
j.cost_box_1=abs((j.box1(:,:,:,:,:,:))-(low_lat_obs));%cost evaluation for each box
j.cost_box_2=abs((j.box2(:,:,:,:,:,:))-(hi_lat_obs));
j.cost_box_3=abs((j.box3(:,:,:,:,:,:))-(deep_oc_obs));
j.cost_fr=abs((j.boxf(:,:,:,:,:,:))-(f_obs));
jcost=j.cost_box_1+j.cost_box_2+j.cost_box_3+j.cost_fr/1000;
```

```
%%
k.cost_box_1=abs((k.box1(:,:,:,:,:,:))-(low_lat_obs));%cost evaluation for each box
k.cost_box_2=abs((k.box2(:,:,:,:,:,:))-(hi_lat_obs));
k.cost_box_3=abs((k.box3(:,:,:,:,:,:))-(deep_oc_obs));
k.cost_fr=abs((k.boxf(:,:,:,:,:,:))-(f_obs));
kcost=k.cost_box_1+k.cost_box_2+k.cost_box_3+k.cost_fr/1000;
```

Inner function expt 3

```
function  [ dX1,dX2,dX3,dXf]=arrow_3_box_lo_to_hi_4_20_mass_b(X1,X2,X3,Xf,n,k,overturning,mix_l,mix_h,fraction_flux, mix_f);%input concentrations
%output change in concentration at each timestep

standard=.1107/55.55;
Y=((-20/1000)+1)*standard*55.55;  %runoff into high latitude surface box is -20 per mil
Z=((-1.1/1000)+1)*standard*55.55 ;%transport thru Bering Strait is -2 per mil
runoff=.18;%Sverdrup strength of runoff
lo_hi_expt=.8;%Transport thru Bering Strait

%fraction_flux=[ ];%fraction flux value from low to high latitudes: values are for each loop iteration 1-3
overturning_1_2=overturning-fraction_flux-runoff-lo_hi_expt;%overturning flux values from lo latitude box to high latitude box: values are for each loop iteration 1-3
SPYR=86400*365;              % secs per year

V=[1.4858e+16 1.8745e+15  2.7476e+17]; %volumes of the 3 ocean boxes in m^3: in order; low, high, deep

% for i=1:1:n; %number of time iterations for 180 concentration development through each cean box

% Flux matrix
F=[0 (overturning_1_2+mix_f+fraction_flux*(k)) mix_l ; %row one, box one flux values  1,1 (from box 1 to box 1) 1,2 (from box 1 to box 2 o_t)  1,3 (from box 1 to box 3 o_th)
    mix_f      0           (mix_h+overturning);       %row two, box two flux values  2,1 (from box 2 to box 1 t_o) 2,2 (from box 2 to box 2)  2,3 (from box 2 to box 3 t_th)
    (mix_l+overturning)  mix_h               0];     %row 3,   box 3   flux values  3,1 (from box 3 to box 1 th_o) 3,2 (from box 3 to box 2 th_t)  3,3 (from box 3 to box 1)

F = F.*1e6;%Sverdrup conversion
```

Code main, expt 3

```
clear all
close all
conversion1 = 0.110712368610173;
%E=16
%H1=.110706



%%     traces the heavy isotope for each timestep
alpha=.9860:.0014:.9960;%matrix congtains increasing values of alpha for 180
d=length(alpha);% d gives us the same length for all experiments


start=5.5; %base overturning before loop
strongest=7.5 ;
ov=start:.35:strongest;  %overturning flux value in Sverdrups: values are for each loop iteration 1-3
e=length(ov);

mix_l_start=1.6;
mix_low_latitude=mix_l_start:.14:2.6;
f=length(mix_low_latitude);

mix_h_start=5;
mix_high_latitude=mix_h_start:2:19;
g=length(mix_high_latitude);

at_fraction=.092:.009:.155;
h=length(at_fraction);

mix_horiz=1.85:0.85:7.85;
l= length(mix_horiz);

for q=1:e;%overturn from 13.5-17.5
    for r=1:f;%mix low latitude 4
        for s=1:g;%mix high latitude 5
            for t=1:d; %next change in alpha from .976 to .980
                for u=1:h; %atmos fraction
                    for m=1:l;%mix horiz
                        n=900;% timestep in years
```

Code main, continued

```
overturning=ov(q);
k1=alpha(t); %fractionation value for heavy isotope

mix_l=mix_low_latitude(r);
mix_h=mix_high_latitude(s);
fraction_flux=at_fraction(u);
mix_f=mix_horiz(m);
standard=.1107/55.55;   %Standard mean ocean water value in mmol/m^3

dH1=zeros(900,1);
dH2=zeros(900,1);
dH3=zeros(900,1);
dHf=zeros(900,1);
H1=zeros(901,1);
H2=zeros(901,1);
H3=zeros(901,1);
Hf=zeros(901,1);
%
H1(1)=  conversion1 ;  %Initial 18O concentration in mmol/m^3 for low latitude ocean box
H2(1)=  conversion1 ;  %Initial 18O concentration in mmol/m^3 for high latitude ocean box
H3(1)=  conversion1 ;  %Initial 18O concentration in mmol/m^3 for deep ocean box
Hf(1)=H1(1);


heavy_isotope=@arrow_3_box_lo_to_hi_4_20_mass_b;
% Creates an alias called 'heavy isotope'-for
% the box function

for i=1:n;
    % [PHL]=high_latitude_precipitation_flux_2_19(fraction_flux,f,k1,H1,H2);
    [dH1(i),dH2(i),dH3(i),dHf(i)]=heavy_isotope(H1(i),H2(i),H3(i),Hf(i),n,k1,overturning,mix_l,mix_h,fraction_flux, mix_f);

    %Calls the box function with the
    %initial 18O values for each box
    %returns the '-change in'- 18O
    %for each timestep for each box

    %This little loop generates the
    %isotope value at the next timestep
```

Code main, continued

```
                            H1(i+1)=H1(i)+ dH1(i);
                            H2(i+1)=H2(i)+ dH2(i);
                            H3(i+1)=H3(i)+ dH3(i);
                            Hf(i+1)=(H1(i+1))*k1;
                        end
                             %input(i)=(ov(i),mix_low_latitude(i),mix_high_latitude(i),alpha(i),at_fraction(i),mix_horiz(i))


                            %%     traces the light isotope for each timestep



                            box1(q,r,s,t,u,m)=(((H1(i+1)/55.55)./standard)-1)*1000;%d18O values for overturn experiment box1
                            box2(q,r,s,t,u,m)=(((H2(i+1)/55.55)./standard)-1)*1000;%d18O values for overturn experiment box2
                            box3(q,r,s,t,u,m)=(((H3(i+1)/55.55)./standard)-1)*1000;%d18O values for overturn experiment box3
                            boxf(q,r,s,t,u,m)=(((Hf(i+1)/55.55)./standard)-1)*1000;%d18O values for overturn experiment box3


                    end
                end
            end
        end
    end
%% figure
 figure (1)
 plot((((H1/55.55)/standard)-1)*1000,'o');
 hold on
 plot((((H2/55.55)/standard)-1)*1000,'o');
 hold on
 plot((((H3/55.55)/standard)-1)*1000,'o');
 title('single box evolution')
```

IV Three-box model of Atlantic $\delta^{18}O$ of seawater with temperature-dependent Rayleigh fractionation and comparison with modern and LGM data

1 Introduction to the box-model structure

This chapter outlines a new version of the Atlantic 3-box model from Chapter 2 with a more realistic and temperature-dependent simulation of Rayleigh fractionation of atmospheric water vapor. The goal of this chapter is to match the $\delta^{18}O_{sw}$ gradients of the 3 ocean reservoirs and its vapor transport for the Holocene as in Chapter 2, and evaluate how changes in temperature and circulation at the Last Glacial Maximum (LGM) match measured surface and deep spatial gradients in $\delta^{18}O_{sw}$ at the LGM.

Like the model in Chapter 2, this newer box-model allows circulation to change independently of other climate variables. It is useful in part because these experiments are not feasible in a more complex model; the impacts of circulation changes on $\delta^{18}O_{sw}$ can be explored more easily with a simple model than with an isotope enabled General Circulation Model (GCM). The experiments estimate the impact of overturning strength and other parameter changes on $\delta^{18}O_{sw}$ gradients (low-to-high, low-to-deep differences) at the LGM

and examine how the effects of uncertainties in these parameters compare to more well-constrained changes such as the closure of the Bering Strait.

Whereas Chapter 2 uses a single atmospheric GCM (aGCM) to constrain evaporative transport in the modern only (Battisti, et al., 2014), the new model version uses the mean of three Paleoclimate Model Intercomparison Project (PMIP3) models to estimate evaporation, precipitation and fraction of transport across 50° N (Dufresne et al., 2013; Jungclaus et al., 2013*;* Voldoire et al., 2011) for the Holocene (0-4 ka) and Last Glacial Maximum (LGM; 20 ka). Additionally, a new function relates isotopic fractionation during evaporation and condensation/precipitation to sea surface temperature change in the low-latitudes (Majoube, 1971; Vachon, 2010).

These model improvements were made to compare model runs with $\delta^{18}O_{sw}$ data for the Holocene and LGM in both surface and deep measurements. Data for comparison to LGM surface boxes is based on the estimated change in $\delta^{18}O_{sw}$ of the sea surface in 119 relevant sites. The purpose of the LGM-to-Holocene study was to calculate the global $\delta^{18}O_{sw}$ anomaly between these 2 episodes (Waelbroeck et al., 2014). Data for the deep ocean comparison comes from $\delta^{18}O_{sw}$ of pore water (Adkins et al., 2002; Schrag et al., 2002) and

benthic $\delta^{18}O_{sw}$ from a piston core from the deep North Atlantic (Sosdian and Rosenthal, 2009).

The newer model remains an under-constrained system as in Chapter 2; the final version of the 3-box model has 8 input parameters and 4 output ocean reservoir values. Also like Chapter 2, it is still possible to have an infinite number of solutions which fit the four reservoirs' observations of 2 surface boxes, vapor transport, and deep box $\delta^{18}O_{sw}$. Instead of tuning, this chapter evaluates whether physically realistic parameter values produce results consistent with $\delta^{18}O_{sw}$ observations for the modern/Holocene and LGM (LeGrande and Schmidt, 2006; Waelbroeck et al., 2014).

Section 2 of this chapter summarizes the motivation to study $\delta^{18}O_{sw}$ gradients at the LGM and why this motivation required changes to the model presented in Chapter 2. This section also outlines background studies of $\delta^{18}O_{sw}$ variations between the Holocene and LGM. Reconstructions based on proxy data between the Holocene and the LGM based on changes in overturning strength are also examined. Section 3 describes $\delta^{18}O_{sw}$ gradient changes from the low-to-high latitudes, and surface-to-deep boxes and gives an overview of the required model modifications for the LGM. A detailed description of model changes is provided in the supplemental appendices.

Appendix A provides a derivation for the fractionation of vapor transport across 50° N in the Atlantic and the development of a model mean of models of intermediate complexity for the vapor transport parameters. Appendix B summarizes literature estimates of ocean circulation parameters and describes how GCM results were used to derive modern and LGM estimates for temperature of evaporation, evaporative flux and temperature of precipitation.

Section 4 presents model results for the LGM and sensitivity tests which evaluate how changes in temperature of fractionation, ocean circulation and atmospheric water vapor transport affect $\delta^{18}O_{sw}$ gradients. It includes experiments estimating LGM gradients based on data and combinations of the initial sensitivity tests. Finally, it introduces inverse model estimates of $\delta^{18}O_{sw}$ gradient changes based on proxy data in the glacial ocean (Gebbie, 2012; Gebbie, 2014; Gebbie, 2015) and examines global versus regional changes in these models.

Section 5 compares the model run to modern and LGM seawater $\delta^{18}O_{sw}$ gradients and estimates of ocean and atmospheric flux. Section 6 summarizes the conclusions of this study. Model results show that increases in Arctic runoff could disguise the effects that potential slowed overturning has on $\delta^{18}O_{sw}$ gradients between these two time intervals.

2 Background

2.1 Overview and motivation

The impacts of circulation changes on $\delta^{18}O_{sw}$ can be explored faster and more cost-effectively with a simple model than with a complex model. Computational costs make these types of experiments in complex models expensive. However, it is relatively simple to compare the effects on the modeled change when altering one parameter at a time in a 3-box model.

Gradient changes in the model and the data are explored in this study rather than individual box changes because water enrichment during the LGM is variable according to the location of the ocean basin (Duplessy et al., 2002; Adkins et al., 2002); we note that local differences in the $\delta^{18}O_{sw}$ have been attributed to vapor transport, overturning circulation, and turbulent vertical mixing between the surface and the deep ocean. For example, water vapor advected north and south from the subtropics becomes lighter isotopically (Craig and Gordon, 1965).

Gradients should not be sensitive to uncertainty in the amount of ice volume change between the Holocene and LGM. Although glacial-interglacial changes in $\delta^{18}O_{sw}$ are dominated by ice volume changes, deep water masses can be traced using their characteristic $\delta^{18}O_{sw}$ values because $\delta^{18}O_{sw}$ is conserved as it travels through the deep ocean. Tracing $\delta^{18}O_{sw}$ properties of water masses between the modern and the LGM may be a useful tool to estimate the location and depth of source water as it reaches the deep ocean.

Slower overturning circulation results in a larger gradient between the low and the high latitude surface ocean whereas decreased atmospheric flux between the low and high latitudes decreases enrichment of $\delta^{18}O_{sw}$ in the low latitudes and creates relative enrichment of $\delta^{18}O_{sw}$ in the high latitudes, bringing box values closer together (Mix, 1992). Increased high-latitude vertical mixing and overturning circulation decreases the difference in tracer gradients between the surface boxes and between the high-latitude and deep ocean (Archer, 2000). Therefore, these comparisons may help identify how ocean dynamics at the LGM affected the distribution of $\delta^{18}O_{sw}$, independent of uncertainty in the mean Atlantic $\delta^{18}O_{sw}$ change.

2.2 Data

2.2.1 LGM $\delta^{18}O_{sw}$ of surface Atlantic

The $\delta^{18}O_{sw}$ data for the two surface boxes of the LGM model come from gradients in Atlantic $\delta^{18}O_{sw}$ between the modern and the LGM. Sea surface temperature estimates based on data from Mg/Ca, alkenones, and dinoflagellate cyst analyses have been used to estimate LGM minus late Holocene (LH) (0-4 ka) surface $\delta^{18}O_{sw}$ anomalies at 119 sites across the global ocean (Waelbroeck et al., 2014). LGM minus Holocene $\delta^{18}O_{sw}$ on the Iberian Margin is interpreted to result from drier conditions and reduced runoff in the Mediterranean region during the LGM. Positive anomalies found in the tropical North Atlantic are consistent with evidence of increased salinity during the LGM (Carlson et al, 2008), which could reflect reduced advection of salty waters to the north and/or a southward shift of the Intertropical Convergence Zone (ITCZ). Negative anomalies just south of the equator are also interpreted as evidence of a southward shift in the ITCZ.

2.2.2 LGM $\delta^{18}O_{sw}$ of deep Atlantic

The target data for the LGM-to-Holocene vertical gradient change from surface-to-deep comes from the combination of pore water data and data from deep-sea sediment cores. The combined deep-box average is calculated from four individual porewater estimates and one estimate averaged from four piston core measurements. Piston-core data was calculated from a time series of benthic $\delta^{18}O_{sw}$ and bottom water temperature estimates of $\delta^{18}O_{sw}$ measurements in one location: (43° N, 31° W, depth 3406 m; Sosdian and Rosenthal, 2009). This calculation uses the paleotemperature relationship between $\delta^{18}O_{sw}$ calcite and temperature based on Mg/Ca ratios: (T = 16.9 – 4.0 ($\delta^{18}O_c$ – $\delta^{18}O_{sw}$; Sosdian and Rosenthal, 2009; Shakleton, 1974).

The deep-box pore-water measurements of $\delta^{18}O_{sw}$ change are governed by an advection diffusion function which determines the concentration of $\delta^{18}O_{sw}$; it decreases with the distance from the source and levels off over time with the square root of the distance. The measurements are from four locations between 33-61° N, 31-57° W, 2184-4583 m depth (Table 1b; Adkins et al., 2002).

Although estimates of deep ocean change vary from 0.7 to 1.1‰, a consensus exists for a smaller change in the Atlantic than in the Southern Ocean (Duplessy et al., 2002; Adkins et al., 2002). A South Atlantic core site (50° S, 6° E, 3623 m) with a pore water difference of 1.1 +/-0.1‰ likely includes an influence of Southern source water (Schrag et al., 2002). Duplessy et al., (2002) found that a comprehensive assessment of continental ice volume loading at the LGM supports the upper limit of ~1.1‰ Atlantic $\delta^{18}O_{sw}$ change relative to the Holocene; the minimum change in $\delta^{18}O_{sw}$ of 0.7‰ comes from calculations assuming that North Atlantic source water sank at its freezing point.

2.3 Estimates of Atlantic overturning change

2.3.1 Proxy estimates

Spatial studies indicate that source water location and depth in the North Atlantic was different at the LGM and the Holocene. For example, North Atlantic source water reaches depths of 2000 meters in the modern Atlantic (Dickinson et al., 1993), but may have shoaled above 2000 m at the LGM (called Glacial North Atlantic Intermediate Water). Additionally, North Atlantic source water had a different spatial location at the LGM; Gutjahr et al., (2008) used Epsilon-Neodymium (εNd) proxies to show that the North Atlantic water mass

at the LGM was not derived from the Labrador sea which is where modern North Atlantic source water is formed. Piotrowski et al. (2005) strengthened the idea of a different North Atlantic southern boundary by showing that the South Atlantic more closely resembled the Pacific ocean than it does today; at the LGM there was a less depleted Neodymium signal at 41° S, 10° E. Additionally, Rutberg et al. (2000) found that the North Atlantic water export to the Pacific was weaker at the LGM than the present day because of a possibly different southern boundary.

Whereas Nd data can provide information about water mass locations, the proxy $^{231}Pa/^{230}Th$ (Protactinium/Thorium) can suggest relative rates of water mass flux due to differences in decay rates of two daughter products of Uranium. McManus et al. (2004) estimated that North Atlantic deep water production slowed at the LGM to 30% of modern from the time period of 19.8-17.5 ka. A relatively slow overturning circulation would be represented by a ratio of $^{231}Pa/^{230}Th$ similar to the natural production rates of these elements. A drawback of this proxy is non-conservative behavior due to diatom scavenging of ^{231}Pa, which may reset the Pa/Th ratio to its original production rate. Thus, ambiguity in this proxy suggests that stronger overturning at the LGM was possible.

To address the ambiguity of overturning flux caused by microbe nutrient scavenging in the surface ocean, a review was conducted with Pa/Th estimates and primary production proxies including $\delta^{13}C$, Cd/Ca, from deep sea cores at the LGM. Lynch-Stieglitz et al. (2007) find that overturning flux may have been dependent upon a variety of interactions resulting from salinity differences between denser, colder, deep water and fresher surface waters of the LGM. It concludes that overturning circulation at the LGM varied from 30% below modern circulation to slightly above modern values (Lynch-Stieglitz et al., 2007).

To determine the strength and location of North Atlantic overturning over the entire glacial cycle, Boehm et al. (2015) used both Nd and Pa/Th tracers in the Western North Atlantic and inferred a strong and stable overturning circulation throughout the last glacial cycle with the exception of the Last Glacial Maximum. Until 27 ka BP overturning remained strong, but when the northern ice sheet reached its maximum extent, increased meltwater in the surface ocean slowed deep water formation by up to 40% and allowed southern source water to shoal the northern overturning cell. The authors further hypothesized that overturning circulation slowed to its minimum only following the LGM. During abrupt climate occurrences such as Heinrich stadials, surface stratification slowed source water formation even further (McManus et al., 2004; Boehm et al., 2015).

2.3.2 Forward model estimates

Forward model simulations suggest a wide variety of Atlantic meridional overturning circulation (AMOC) estimates at the LGM (13.1-29.5 Sv) as compared to the modern (13.8-23 Sv). The AMOC varies from 40% below modern AMOC to an increase of 40% above the modern in a review of models of intermediate complexity such as the Paleoclimate Model Intercomparison Project (PMIP) models and GCMs (Weber et al., 2007). In these experiments overturning strength is recorded as the maximum flux strength of the main circulation cell, located between 56-65° N. Each modern control run is paired with its LGM run. GCMs which have a slower than modern AMOC include the CCSM (17%), Hudl 2 (3%), UTor (40%), ClimC (20%; Peltier and Solheim, 2003; Gordon et al., 2000; Ganopolski and Rahmstorf, 2001). Those models which have a weakening of NADW also have a southward shift in Atlantic source water formation (Weber et al., 2007). Some models exhibit basinwide shifts in density due to evaporation which scale with the overturning strength, but these relationships are not definitive.

A variety of LGM boundary conditions have yielded increased overturning in climate models. For example, two GCMs which allow circulation through the Bering Strait at 21 ka during the LGM simulated increased overturning: MIROC with a 39% stronger AMOC than the modern reported as 18.8 Sv (Hasumi and Emori, 2004) and MRI with a 9% stronger than modern reported at 27.1 Sv (Kitoh et al., 2001; Weber et al., 2007).

However, strengthened circulation at the LGM is not restricted to models which allow circulation through the Bering Strait. For example, two models also exhibit strengthened AMOC at the LGM do not feature Bering Strait flux at 21 ka. The first of these is a model of intermediate complexity with a sea-ice component and the second is a coupled atmosphere-ocean GCM: The Vanderbilt model ECBilt has 25% overturning flux above the modern and Hadl1.5 has 19% overturning flux above the modern (Weber et al., 2007). Among the models with stronger circulation at the LGM, the MIROC model is initialised from a modern (exclusively warm) state whereas the other three models are initialised from a cold state or with glacial forcing.

Ballarotta et al., (2013) examine ocean circulation flux at the LGM with an ocean GCM using coarse and fine resolution to assess the model's skill in reconstructing the glacial ocean. Results from the eddy resolving version of this model show a maximum of

overturning flux of 11 Sv above 600 m at 35° N. The coarser version of this model shows a maximum of 17 Sv of overturning flux at 100 m depth in the same latitude, with strong overturning above 600 m.

A simpler two-dimensional ocean dynamical model showed that increasing sea-ice extent in the Southern Ocean at the LGM was enough to shoal the Atlantic overturning circulation without slowing it down (Burke et al., 2015). These results were confirmed by a model of intermediate complexity; iLOVECLIM reaches an overturning circulation of 5-20 Sv between 20 and 50 ka, as examined in three time slices (Burckel et al, 2016). The northern source water mass circulated above 2500 m. The iLOVECLIM model is able to reproduce a linear relationship between temperature of the surface ocean and the $\delta^{18}O$ of rainfall for temperatures up to 15° C (Roche, 2013): $\delta^{18}O_{precip.} = 0.61 * T_{surf.} - 15.6$.

Summarizing the research on NADW at the LGM, a combination of water mass proxies and overturning circulation proxies suggest both a shallower and weaker North Atlantic water mass; a 2-dimensional modeling study suggests this might be due to a shifting northward of the deep water formation due to extended sea-ice formation in the South Atlantic. However, a mixture of slower-than-modern and faster-than-modern overturning

exists in climate models initialised from a variety of climate states, suggesting further studies on this topic are warranted.

2.4 Model-data disagreements in $\delta^{18}O_{sw}$

Existing models are not consistently able to match LGM spatial gradients in $\delta^{18}O_{sw}$ in the Atlantic. In particular, the pore-water gradients from Adkins et al. (2002, Table 1b) are not well reproduced by a model of intermediate complexity (Figure 1, Caley et al., 2014; Caley and Roche, 2013). Pore water changes are more negative than the model predicts at a site located at 30° South and 4500 m depth and at 3000m at 5° N, but pore water change is more positive than the model at 3700 m depth at 50° S. When pore water data are superimposed on the North Atlantic transect, areas differ from South to North between model and data by: ~0.08, ~-0.04, ~-0.2, ~-0.13, ~-0.04,~ -0.07 ‰. Model and data however, both suggest about 2-4 degrees of cooling at the LGM (Caley et al., 2014).

Figure 1 Pore water data on iLOVECLIM modeled $\delta^{18}O_{sw}$ in the Atlantic.

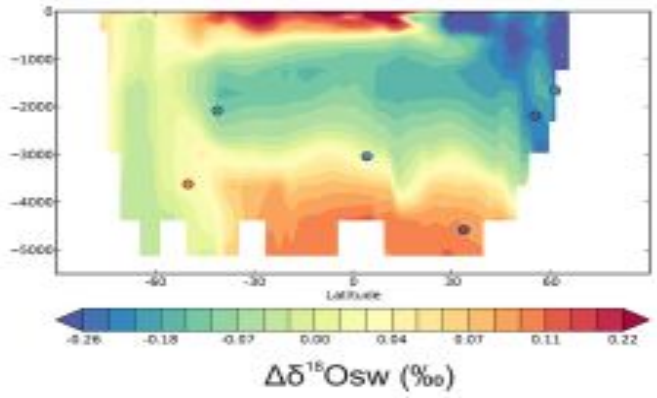

Figure 1 The model of intermediate complexity (Caley and Roche, 2014) shows modeled change in $\delta^{18}O_{sw}$ superimposed with $\delta^{18}O_{sw}$ pore water data. Data representing LGM minus Holocene $\delta^{18}O_{sw}$ change does not match GCM modeled $\delta^{18}O_{sw}$ in the Atlantic. A mean change was subtracted to illustrate regional changes.

3.0 Methods

The water vapor transport from the low to the high-latitudes in the North Atlantic in this chapter includes parameters of evaporative flux, fractionation of evaporation, fraction of transport, fractionation of latitudinal transport. A detailed description of model changes is provided in Appendix A. Because the fractionation parameters are based on the low-latitude

temperature of evaporation, the number of essential parameters changes from 6 to 8 instead of 6 to 9.

Impacts of the 3-box model on ocean basin $\delta^{18}O_{sw}$ are explored with several circulation changes at the LGM. Summaries of how LGM parameter values were selected is provided in Appendix B. All parameters affecting atmospheric transport were estimated from the mean values of three Paleoclimate Model Intercomparison Project (PMIP3) GCM models. Holocene parameters of horizontal mixing remain the same as in Chapter 2. Other parameters are from the literature as described in Appendix B.

The 3-box model at the LGM maintains the same box volumes as the modern/Holocene for simplicity of calculation. Ice volume effects on global mean $\delta^{18}O_{sw}$ are circumvented by comparing the change in gradients between low and high-latitude surface boxes rather than changes of the $\delta^{18}O_{sw}$ of each box. The effects of each model parameter except low-latitude vertical mixing are explored with sensitivity tests that vary parameters one at a time for three different values: modern, estimated LGM, and a value intermediate between the two. Whereas the atmospheric parameters are estimated using model mean values, the ocean flux experiments consider plausible percentage changes relative to the modern (Tables 5a and 5b).

4 Results

4.1 Proxy estimates for each model box

4.1.1 Surface changes

Waelbroeck et al. (2014) estimate the surface Atlantic change in $\delta^{18}O_{sw}$ between the LGM and Holocene by combining 47 pairs of temperature proxies and $\delta^{18}O_c$ measurements from Atlantic locations (by correcting the effect of temperature variation on surface records in $\delta^{18}O_{calcite}$). Waelbroeck et al., (2014) showed that differences exist in Northern and Southern surface $\delta^{18}O_{sw}$ and between LGM and Holocene. Because it is difficult to measure exact surface $\delta^{18}O_{sw}$ in each box at the LGM, examining the change between boxes as a difference between Holocene and LGM values is a more realistic way to examine the alterations in $\delta^{18}O_{sw}$ (Table 1a, Figure 2; Waelbroeck, 2014).

Pairs of measurements for the high-latitude surface ocean in the Atlantic are reported in Supplement table 1 at the end of this chapter. Of nineteen total core sites in the high-latitude

North Atlantic, this chapter only considers data points from 50°-74° N for consistency's sake with the model. Five data points are excluded from the high-latitude compilation because the authors consider a large positive temperature anomaly in the North Atlantic unrealistic. The unrealistic values tend to correspond to LGM-Holocene $\delta^{18}O_{sw}$ anomalies greater than 2‰, and temperatures generally are derived from proxies other than Mg/Ca in foraminifera. In another location, a negative $\delta^{18}O_{sw}$ anomaly was likely caused by its proximity to the Greenland ice sheet and was removed from south of Iceland because of its inconsistency with the others. Isotope enabled climate models generate negative $\delta^{18}O_{sw}$ anomalies in the Arctic from -0.3 to -0.7‰ between the Holocene and LGM, but the Arctic was removed from this model.

The mean error for the high-latitude Atlantic and low-latitude Atlantic was determined by taking the root of the sum of the squared standard deviation for each site, divided by the number of measurements. For the thirteen sites included in the high latitude mean, the average $\delta^{18}O_{sw}$ change is 1.18‰ with an uncertainty of 0.26‰ (one standard deviation; Table 1a, Figure 2). Thirty-four MARGO data pairs comprise the low-latitude surface Atlantic $\delta^{18}O_{sw}$. The mean low-latitude change in $\delta^{18}O_{sw}$ is 1.14‰ with an uncertainty of 0.12‰. The error is smaller in the low latitude box than in the high latitude box because there are

more measurements (34 versus 13). The measured surface gradient change between the LGM and Holocene is near zero at -0.04‰ (Table 1a, Figure 2)with a propagated error of +/-0.29‰.

Table 1a MARGO gradients between boxes and change between LGM and Holocene

Observations of $\delta^{18}O_{sw}$	**No. of sites**	**Mean Holocene $\delta^{18}O_{sw}$ from core sites ‰**	**Estimated $\delta^{18}O_{sw}$ LGM ‰**	**LGM-Holocene change ‰**
High-Latitude Box Mean (Waelbroeck et al., 2014)	**13**	**0.56 (+/-0.06)**	**1.74**	**1.18 (+/0.26)**
Low-Latitude Box Mean (Waelbroeck et al., 2014)	**34**	**1.08 (+/-0.03)**	**2.22**	**1.14 (+/-0.12)**
Gradient Low-High boxes		**0.52 (+/-0.07)**	**0.48**	**-0.04 (+/-0.29)**

Table 1a indicates gradients in proxy data between specified surface model boxes (Low box minus high box is the surface gradient, and change between the 2 eras is LGM minus Holocene (0-4 ka) for each box (column 3; Waelbroeck, 2014). The dataset estimates an approximate 0.5‰ gradient between the low and high-latitude surface boxes during both the LGM and Holocene (0-4 ka; Waelbroeck et al., 2014).

4.1.2 Deep Atlantic $\delta^{18}O_{sw}$ change

Data for deep-box sites include pore-water measurements in four locations and indicate a mean change of approximately 0.76‰ between the Holocene and the LGM at depths between 3000 and 4500 meters (Adkins and Schrag, 2002; Schrag et al, 2002). A single piston core location records 0.86 ‰ of change (Table 1b; Schrag et al, 2002; Sosdian and Rosenthal, 2009). Three measurements comprise the piston core LGM datapoint, and the combined error for the change is +/- 0.34‰. Combined, the two datasets average 0.78‰ change in the model's deep box with a combined error of +/- 0.09‰. The last row illustrates the benthic change in pore water estimates in the North Atlantic in locations from 4° N to 65° N and in Sodian and Rosenthal (2009) piston core estimates at 43° N.

4.1.3 Gradient changes

Differences between the mean LGM-Holocene $\delta^{18}O_{sw}$ anomaly in each box are used to calculate the gradient change (LGM minus Holocene) between the two surface boxes as -0.04‰, and the gradient change between the low-latitude surface box and the deep box as 0.36‰. Gradient change is the metric used for comparison with model results because it is not dependent upon estimates of global ice volume change.

Table 1b Deep $\delta^{18}O_{sw}$ changes, LGM minus Holocene, 3 reservoir boxes

Observations of $\delta^{18}O_{sw}$	No. of sites	Mean Holocene $\delta^{18}O_{sw}$ ‰ from core sites	Estimated $\delta^{18}O_{sw}$ ‰ LGM	LGM-Holocene change ‰
Schrag et al. 2002 Site 984 61° N	**1**	**0.1(+/-0.03)**	**0.9**	**0.8 +/-0.1**
Schrag et al. 2002 Site 925 4° N 43° W depth 3041 m	**1**			**0.8 +/-0.1**
Schrag et al. 2002 Site 1063 33° N 57° W depth 4583 m	**1**	**0.05*(+/-0.03)**		**0.75 +/- 0.05**
Schrag et al 2002 Site 981 55° N Depth 2184 m	**1**	**0.25(+/-0.03)**	**1.05**	**0.7 +/-0.1**
Sosdian and Rosenthal 2009 Piston Core Chain 82-2-23PC 43° N, 31° W (depth 3406 m)	**1**	**0.22 (+/- 0.32)**	**1.08(+/-0.13) Average of three measurements**	**0.86 (+/-0.34)**
Deep Box Mean	**5**	**0.15(+/-0.16)**	**0.93**	**0.78‰(+/-0.08)**

Table 1b Observed $\delta^{18}O_{sw}$ values for each Atlantic location. Average deep box $\delta^{18}O_{sw}$ values from an Atlantic piston core (Sosdian and Rosenthal, 2009) and pore water measurements (Schrag et al., 2002). However, core-top value is not reported in Schrag (2002), but in Adkins and Schrag (2001), which has a slightly different mean change of 0.75. Core-top precision is assumed to be the same in this case as Schrag (2002). Sosdian and

Rosenthal (2009) determine the relationship between temperature and the $\delta^{18}O_{sw}$ using the expression $T = 16.9 - 4.0 (\delta^{18}O_c - \delta^{18}O_{sw})$.

Table 1c Atlantic $\delta^{18}O_{sw}$ values for each box and gradient changes between boxes. Gradient change is the metric used for comparison with model results because it is not dependent upon estimates of global ice volume change.

	Mean Holocene $\delta^{18}O_{sw}$ from core sites ‰	**Estimated $\delta^{18}O_{sw}$LGM ‰**	**LGM-Holocene change ‰**
High-Latitude Box Mean (Waelbroeck et al., 2014)	**0.56 (+/-0.06)**	**1.74**	**1.18 (+/-0.26)**
Low-Latitude Box Mean (Waelbroeck et al., 2014)	**1.08 (+/-0.03)**	**2.22**	**1.14 (+/-0.12)**
Deep Box Mean	**0.15‰(+/-0.16)**	**0.93**	**0.78‰(+/-0.08)**
Gradient Low-High boxes	**0.52 (+/-0.07)**	**0.48**	**-0.04 (+/-0.29)**
Gradient Low-Deep Boxes	**0.93(+/-0.16)**	**1.29**	**0.36(+/-0.14)**

Figure 2 Graph of magnitudes of $\delta^{18}O_{sw}$ observations, Holocene (left) and LGM minus Holocene (right)

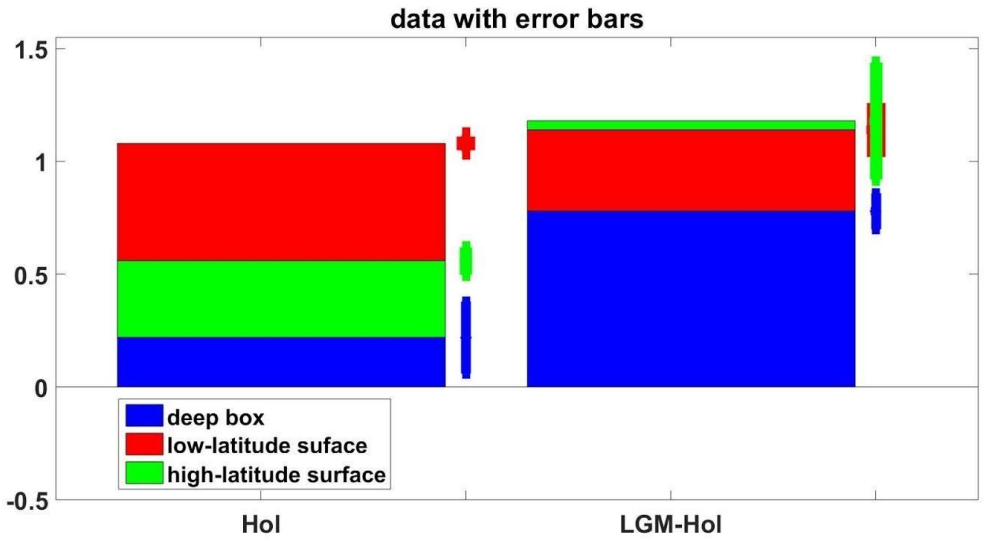

Figure 2 Graphical representation of surface and deep data from Table 1c, columns 2 and 4: Color bars represent ocean boxes with error bars to the right representing the uncertainty. Holocene data is plotted on the left. LGM minus Holocene change, on the right, includes the effect of ice volume change.

4.2 LGM model results

The Holocene model run has similar box values to the modern model run in Chapter 2, despite the fact that the Holocene and LGM runs were not tuned in this chapter. All LGM parameters are lower/slower than the Holocene values, according to literature consensus. See Appendix B for details. The model parameters all have a smaller magnitude during the initial LGM runs (Table 2a); including slower overturning, the overall effect of narrowing the gradient between the surface low and high-latitudes in the LGM run creates vertical and horizontal negative gradient changes between the two eras. Table 2a shows the model configurations while Table 2b shows all the outcomes of the change between the LGM and the Holocene. Freshwater flux parameters when slowed, tend to make model boxes closer together (while ocean flux parameters when slowed, make the modeled boxes farther apart). Therefore, the freshwater flux parameters are able to overcome surface and vertical gradients ocean flux parameters in the LGM model configuration.

The LGM model run yields a surface gradient of 0.35‰, which is a -0.6‰ change from the Holocene surface gradient of 0.95‰. The LGM vertical gradient is 0.3‰ which is a -0.45‰ change of 0.75‰ (Table 2a).

Table 2a Model configuration at the Holocene and LGM

Expt	ov	lo	hi	evap	Tem	hor	frac	Isth vap	River runoff	Low	High	Deep	Water vapor $\delta^{18}O_{sw}$	Sur grad	Vert grad
Hol	5.5	2	7	0.31	292	2	0.36	0.8	0.18	0.8247	-0.1252	0.0748	-19.21	0.9499	0.7499
LGM	3.3	1.2	4.2	0.26	287	2	0.27	0.0	0.018	0.3968	0.0487	0.0967	-23.52	0.3481	0.3001

Table 2a Modern and LGM runs with all parameters.

Table 2b LGM and Holocene summary of model runs

	Low box	***High box***	***Deep box***	***Water vapor*** $\delta^{18}O_{sw}$	Surface gradient	Vertical gradient
Holocene	0.8247	-0.1252	0.0748	-19.2135	0.9499	0.7499
LGM	0.3968	0.0487	0.0967	-23.5201	0.3481	0.3001
Change	-0.4279	0.1739	0.0219	-4.3066	-0.6018	-0.4498

Table 2b LGM and Holocene summary run table indicates $\delta^{18}O_{sw}$ values for each box and surface and deep gradients between boxes. Change from the LGM to the Holocene run is recorded in the third row. Ice-volume effect is not recorded in the model run. Model run at the LGM shows box values closer together than in the Holocene run.

Figure 3 LGM and Holocene $\delta^{18}O_{sw}$ estimates from the box model compared to data estimates for each box.

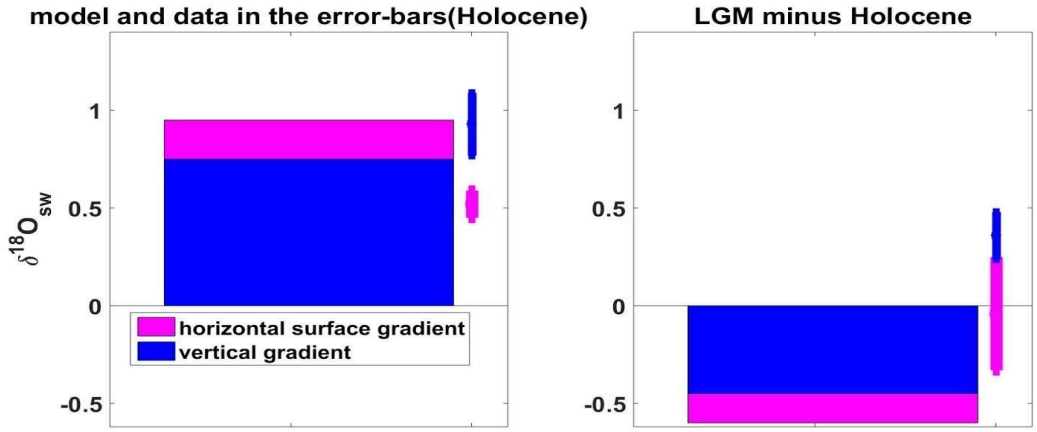

Figure 3 Graphical representation of Table 1d, above, columns 2 and 4. Left figure: Surface horizontal gradients (pink) in the model (bars) compared to proxy-based estimates with error bars (plotted to the right of the bars) and the low-latitude surface-to-deep vertical gradient (blue) in the Atlantic in the Holocene (numbers in Table 1d, column 2). Right figure: LGM minus Holocene modeled horizontal gradient change and vertical gradient change (numbers in Table 1d, column 4). Mean data and error in the error bars to the right of each figure, repeated from Figure 2, above. The difference between the error bars (right) and the modeled boxes in the LGM minus Holocene column provide a reason for the sensitivity tests in Section 4.3 below.

Table 2c Percent difference between modeled LGM-Holocene and Data

	LGM-Hol $\delta^{18}O_{sw}$ *Model*	*LGM-Hol* $\delta^{18}O_{sw}$ *Data*	*Data-Model difference (‰)*
High box	0.1739	1.18	1.01
Low box	-0.4279	1.14	1.57
Deep box	0.0219	0.78	0.76
Surface gradient change	-0.60	-0.04	0.56
Vertical gradient change	-0.45	0.36	0.81

Table 2c indicates that a large amount of change is required if the model were to match the LGM-to-Holocene changes in each of the boxes. The ice volume change of ~1.1‰ is not included in the model so a larger change is expected in the data.

We expect that the data will reflect a mean change of ~1.1 ‰ across the entire Atlantic. Regional low-latitude surface changes reflect a possible regional low-latitude enrichment in the low-latitude surface ocean.The last two rows of Table 2c indicate the need to model gradient change rather than modeled box change.

4.3 Model comparison to $\delta^{18}O_{sw}$ estimates from LGM and Holocene inverse reconstructions

A group of inverse ocean model reconstructions (Gebbie 2012, Gebbie 2014, Gebbie 2015) have been used to infer changes in the LGM Atlantic $\delta^{18}O_{sw}$ and provide a point of comparison for the planktonic and benthic data in Tables 4a-4c . These models trace $\delta^{18}O$ calcite converted to $\delta^{18}O_{sw}$ $\delta^{13}C$ and Cd/Ca, but do not estimate the strength of the LGM overturning. These reconstructions use LGM observations combined with assumed LGM watermass trajectories to estimate the tracer field in the LGM ocean. They have the advantage of providing an interpolated ocean with a 4° by 4° resolution (Gebbie, 2012; Gebbie, 2014; Gebbie 2015). The reconstructions vary in the following ways: the Gebbie (2012) model uses modern water mass trajectories and surface temperature and $\delta^{18}O_{sw}$observations, the Gebbie (2014) model uses $\delta^{13}C$, Cd/Ca and $\delta^{18}O_{calcite}$ surface observations with modern water mass trajectories, while an alternate method utilising this model allows no change in remineralisation of $\delta^{13}C$ in the model. Gebbie et al (2015) uses a global compilation of $\delta^{13}C$ and $\delta^{18}O$ measurements with adjustments to the model for

increased salinity and global sea level fall. Grid cells for each reconstruction have been volumetrically averaged to calculate mean $\delta^{18}O_{sw}$ values for the spatial dimensions of the reservoirs in the three-box model.

Graphs of each model in Figure 4 depict a depth-latitude transect at 318° W (this North-South transect intersects the southern tip of Greenland) where the modern/Holocene $\delta^{18}O_{sw}$ has been subtracted from the LGM $\delta^{18}O_{sw}$. The mean change (LGM minus modern) in each model has been subtracted to show the change without the ice volume contribution. A smaller mean Atlantic LGM $\delta^{18}O_{sw}$ change of 0.88‰ occurs in the Gebbie (2012) reconstruction, and a larger change of approximately 1-1.1‰ is removed from Gebbie (2014), Gebbie (2014)-alt. and Gebbie (2015) reconstructions (Figures 4b-4d). The $\delta^{18}O_{sw}$ in the top 1000 m of the low latitude Atlantic are slightly increased, but the change of $\delta^{18}O_{sw}$ in the North Atlantic remains homogenous from the equator to 90° N between the LGM and the Holocene. The Gebbie (2014)-alt. model results in a slightly enriched surface ocean as compared to the Gebbie (2014) model (Figures 4c and 4b). Although LGM reconstructions are somewhat similar numerically, proxy data show a much less enriched ocean at the LGM than in the data. Differences between proxy and model reconstructions indicate a variety of interpretations possible at the LGM (Table 3).

Figure 4 LGM minus Holocene minus mean change

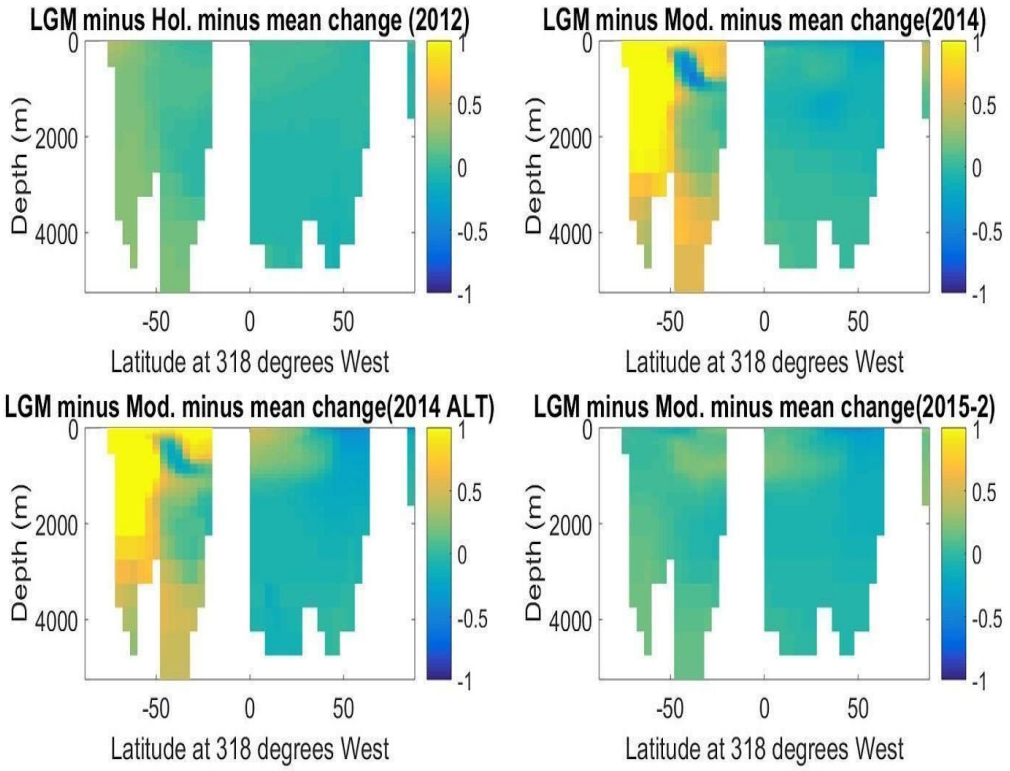

Figure 4a-4d inverse model reconstructions with mean change subtracted: graphs show variations in possible LGM water mass $\delta 18O_{sw}$: Figure 4a Gebbie 2012 reconstruction (LGM minus Holocene (3ka) $\delta^{18}O_{sw}$ reconstruction minus mean change of 0.8834‰) Longitude: 318° West. Figure 4b Gebbie 2014 reconstruction, (LGM minus modern $\delta^{18}O_{sw}$ reconstruction minus mean change of 0.9514‰) Longitude: 318° West. Figure 4c Gebbie 2014 ALT reconstruction, (LGM minus modern $\delta^{18}O_{sw}$ reconstruction minus mean change of 1.0184‰) Longitude: 318° West. Figure 4d Gebbie 2015-2 LGM reconstruction (LGM

minus modern $\delta^{18}O_{sw}$ reconstruction minus mean change of 1.1551‰) Longitude: 318° West.

Table 3 Summary Table of Holocene and LGM Reconstructions

Atlantic boxes	Holocene GISS	Proxy	(G12-3ka)	LGM G12	G14	G14ALT	G15-2	Proxy
High	**-0.04**	**0.56**	**-0.08**	**0.76**	**0.74**	**0.35**	**0.79**	**1.74**
Low	**0.84**	**1.08**	**0.73**	**1.67**	**1.75**	**2.15**	**1.94**	**2.22**
Deep	**0.07**	**0.22**	**0.09**	**0.97**	**1.03**	**1.08**	**1.23**	**1.00**
Δ Surface	**0.88**	**0.52**	**0.81**	**0.91**	**1.01**	**1.80**	**1.15**	**0.48**
Δ Vertical	**0.76**	**0.86**	**0.64**	**0.70**	**0.72**	**1.07**	**0.71**	**1.22**

Table 3 Reconstructions and MARGO proxy data in this table include mean $\delta^{18}O_{sw}$ change due to ice volume. However, gradient changes are not affected by this ice volume effect. Holocene reconstructions in left column, LGM reconstructions in right column. Holocene GISS reconstruction is an interpolation of the surface data from (LeGrande and Schmidt, 2006).

Table 4 Results table: Reconstructions vs. Data results (LGM minus Holocene)

	G12 GISS (3ka)	G14 (surface)	G14ALT	G15-2	**Proxy (MARGO)**
High	**0.80** **0.84**	**0.78** **(0.74)**	**0.39** **(0.2)**	**0.83** **(0.70)**	**1.18(+/-0.26)**
Low	**0.83** **0.94**	**0.92** **(0.80)**	**1.32** **(1.2)**	**1.10** **(1.00)**	**1.14(+/-0.12)**
Deep	**0.90** **0.88**	**0.95**	**1.01**	**1.16**	**0.78(+/-0.03)**
Surface change	**0.03** **0.10**	**0.13**	**0.92**	**0.27**	**-0.04(+/-0.29)**
Vertical change	**-0.07** **0.06**	**-0.04**	**0.31**	**-0.06**	**0.36(+/-0.14)**

Table 4 Each box shows change from the Holocene; in boxes where there are two rows, the values in grey are the change from 3 ka (otherwise, modern). In boxes where the second row is in parentheses, the second row is the surface layer change only. MARGO proxies include 1 sigma error. The Deep box change (middle row) shows the mean change of 0.78 ‰ in Figure 2 above.

4.4 Sensitivity tests

Tables 5a and 5b below display results of sensitivity tests of the model. By changing one parameter at a time, each model run gives one parameter an intermediate (middle column) or Holocene (left column) parameter value while the other model parameters remain at LGM values (right column). The sensitivity of each parameter is ranked against the others and the parameters in each table (5a, 5b) are listed from top to bottom from most positive to most negative change. For example, exhibiting the most change, the modern parameter of runoff shows the largest effect. The cell values in Tables 5a (surface gradient) and 5b (vertical gradient) include the parameter value, the middle value is the gradient for that sensitivity run, and the bottom value indicates the gradient change or percent gradient change (in parentheses) from the LGM. Parameter values and box $\delta^{18}O_{sw}$ values for all sensitivity tests can be found in the supplemental tables at the end of the main section in this chapter.

Negative gradient changes indicate a smaller LGM $\delta^{18}O_{sw}$ gradient than the modern whereas positive gradient changes indicate a larger gradient in the LGM than in the modern. Percentage change indicates the percent of the sensitivity test as compared to the model

LGM run. Percentages greater than 100% indicate a larger change as compared to the LGM experiment whereas less than 100% indicates a change smaller than the full LGM run.

For example, the runoff experiment's surface gradient change yields only 4% of the LGM-minus-Holocene change when given a modern value of 0.18 Sv (Table 5a, row 1) as compared to the LGM run which generates 100% of the LGM minus Holocene gradient change. The surface sensitivity target from Table 2c is 6.66%, indicating that runoff is a likely candidate for further experimentation.

The modern vertical gradient change in the runoff parameter is -14% of the modeled LGM-to-Holocene change of -0.45‰ (Table 5b, row 1). The sensitivity tests on the modeled parameters (runoff, Bering Strait, overturning circulation, evaporation, atmospheric fractionation, low and high-latitude vertical mixing and temperature) exhibit a modeled surface gradient change from 4% to 120% of the LGM minus Holocene gradient change (Table 5a). In the vertical gradient tests (Table 5 b) all parameters except runoff yield a positive modeled change of 45% to 116% of the LGM minus Holocene change (Graph version of Table 5a and Table 5b in Figure 5 shows vertical and horizontal change together). When the runoff parameter is given a modern value of 0.18 Sv, the change between the 2 eras switches signs, yielding -14% of the change (Table 5b, row 1, Figure 5, top row). The

vertical sensitivity target is -80%; the only negative sensitivity experiment is Runoff, indicating further experimentation is warranted. Because of the large negative anomaly, however, it is unlikely that the current model configuration will be able to achieve this value.

Because there was no flux through the Bering Strait at the LGM, the effect of varying this parameter away from zero at the LGM is unrealistic. However, the gradient change sensitivity test results almost double in magnitude when varied from the LGM parameter of no-flux to the modern parameter of 0.8 Sv. The test varies from 0.3‰ to 0.58‰ change in the surface gradients and 0.3‰ to 0.50‰ in the vertical gradients.

The evaporation and fraction of transport experiments show a surface gradient change of only 91 to 92% of the change with modern parameter values, and similarly the vertical gradient change is only 89 to 91% of the change, respectively.

The surface gradient changes in the high-latitude vertical mixing experiments show very little effect, results are 101-100% of the LGM-to-Holocene model change. The low latitude vertical mixing parameter yields a similar 103-100%. In the vertical gradient experiments, high and low-latitude vertical mixing yield 99 and 109% of the change when given modern parameters. Temperature yields 102% of both the surface and vertical change when given a modern parameter.

The parameter which increases the change the most between the LGM and the modern is overturning circulation, which increases the change to 120% when given a modern value of 5.5 Sv. An intermediate value of 4.4 Sv increases the change to 115%, indicating that the effect is slightly non-linear; a 110% intermediate change would indicate a linear change in this case.

4.5 Model experiments with multiple parameter changes

To evaluate whether any reasonable combination of parameter changes can reproduce the gradient change values in the data in both vertical and horizontal gradients, a series of experiments were performed with moderate values for evaporation and fraction of transport and a variety of different runoff values (Table 6). Experiment 7 in Table 6 comes the closest of all the experiments to modeling the vertical and horizontal gradient changes in the data (Figure 3). The modeled surface gradient change of 0.03‰ is very close to the proxy-based estimate, and the model's positive vertical gradient of 0.1‰ is closest to the observed value of 0.36 +/- 0.14, although still outside of the 95% confidence interval.

Similar to the Gebbie (2014) alternate reconstruction, experiment 1 Table 6 shows a positive gradient change in the vertical and horizontal. The parameter configurations are all slow-flux at the LGM with the exception of runoff, at modern flux levels of 0.18 Sv.

Overturning is extra-slow, at 2.2 Sv. Like the proxy data, a positive vertical gradient change is possible. A change of 0.25‰ in the LGM experiment is possible as compared to the model. However, there is also a positive surface gradient change of 0.24‰ whereas the surface gradient change is very little in the proxy data of -0.04‰. Unlike the model and the pore water data, the remaining three reconstruction values show little change in the vertical gradient between the LGM and the Holocene.

Table 5a Surface gradient, percent of modeled change

Sensitivity tests: Parameter change	**Holocene param Modeled diff between LGM-Holocene AND Percent % gradient difference between sensitivity test and model of -0.6 ‰**	**Moderate param Modeled diff between LGM-Holocene AND Percent % gradient difference between sensitivity test and model of -0.6 ‰**	**LGM param Modeled diff between LGM-Holocene AND Percent % gradient difference between sensitivity test and mode of -0.6‰**
Runoff (Sv)	**0.18**	**0.099**	**0.018**
Test gradient (‰)	**0.92**	**0.63**	**0.30**
Gradient change(‰,%)	***-0.03(4%)***	***-0.32(53%)***	***-0.60(100%)***
Bering Strait (Sv)	**0.8**	**0.4**	**0**
Test gradient (‰)	**0.58**	**0.46**	**0.30**
Gradient change(‰,%)	**-0.37(62%)**	**-0.49(82%)**	***-0.60(100%)***
Evap (Sv)	**0.31**	**0.285**	**0.26**
Test gradient (‰)	**0.40**	**0.38**	**0.30**
Gradient change(‰,%)	**-0.55(91%)**	**-0.57(95%)**	***-0.60(100%)***
Atmospheric fraction	**0.36**	**0.315**	**0.27**
Test gradient (‰)	**0.40**	**0.37**	**0.30**
Gradient change(‰,%)	**-0.55(92%)**	**-0.58(96%)**	***-0.60(100%)***
Vertical Mixing (hi) (Sv)	**7**	**5.6**	**4.2**
Test gradient (‰)	**0.34**	**0.34**	**0.30**
Gradient change(‰,%)	**-0.61(101%)**	**-0.61(101%)**	***-0.60(100%)***
Temperature (C)	**18.86**	**15.86**	**13.85**
Test gradient (‰)	**0.34**	**0.34**	**0.30**
Gradient change(‰,%)	**-0.61(102%)**	**-0.61(101%)**	***-0.60(100%)***
Vertical Mixing (lo) (Sv)	**2**	**1.8**	**1.2**
Test gradient (‰)	**0.33**	**0.33**	**0.30**
Gradient change(‰,%)	**-0.62(103%)**	**-0.62(102%)**	***-0.60(100%)***
Overturning (Sv)	**5.5,**	**4.4**	**3.3**
Test gradient (‰)	**0.23**	**0.26**	**0.30**
Gradient change(‰,%)	**-0.72(120%)**	**-0.69(115%)**	***-0.60(100%)***

Surface gradient change table Parameter is the top value in each cell. Middle value is the gradient result for each test. Bottom value is change from the LGM for each test (LGM

minus Holocene change). Only 6.66 percent of the modeled surface gradient is required to recreate the surface gradient in the data, indicating the modern Runoff experiment is a likely candidate for further experimentation.

Table 5b Vertical Gradient, percent of model change

Sensitivity tests: Parameter change	**Holocene param Modeled diff between LGM-Holocene AND Percent % gradient difference between sensitivity test and data of-0.45 ‰**	**Moderate param Modeled diff between LGM-Holocene AND Percent % gradient difference between sensitivity test and data of -0.45 ‰**	**LGM param Modeled diff between LGM-Holocene AND Percent % gradient difference between sensitivity test and data of -0.45 ‰**
Runoff **Test gradient (‰)** **Gradient change(‰,%)**	**0.18** **0.81** **0.06(-14%)**	**0.099** **0.55** **-0.20(45%)**	**0.018** **0.30** **-0.45(100%)**
Bering Strait (Sv) **Test gradient (‰)** **Gradient change(‰,%)**	**0.8** **0.5** **-0.25(56%)**	**0.4** **0.40** **-0.36(79%)**	**0** **0.30** **-0.45(100%)**
Evap (Sv) **Test gradient (‰)** **Gradient change(‰,%)**	**0.31** **0.35** **-0.40(89%**	**0.285** **0.32** **-0.43(95%)**	**0.26** **0.30** **-0.45(100%)**
Atmospheric fraction	**0.36** **0.40** **-0.41(91%)**	**0.315** **0.37** **-0.43(95%)**	**0.27** **0.30** **-0.45(100%)**
Vertical Mixing (hi) (Sv) **Test gradient (‰)** **Gradient change(‰,%)**	**7** **0.30** **-0.45(99%)**	**5.6** **0.30** **-0.45(100%)**	**4.2** **0.30** **-0.45(100%)**
Temperature (C) **Test gradient (‰)** **Gradient change(‰,%)**	**18.86** **0.29** **-0.46(102%)**	**15.86** **0.30** **-0.45(101%)**	**13.85** **0.30** **-0.45(100%)**
Vertical Mixing (lo) (Sv) **Test gradient (‰)** **Gradient change(‰,%)**	**2** **0.26** **-0.49(109%)**	**1.8** **0.27** **-0.48(107%)**	**1.2** **0.30** **-0.45(100%)**
Overturning (Sv) **Test gradient (‰)** **Gradient change(‰,%)**	**5.5** **0.23** **-0.52(116%)**	**4.4** **0.26** **-0.49(109%)**	**3.3** **0.30** **-0.45(100%)**

Vertical gradient change table Parameter is the top value in each cell. Middle value is the gradient result for each test. Bottom value is change from the LGM for each test (LGM minus Holocene change). The sensitivity target is -80%; a negative gradient change is only possible with the runoff parameter in the vertical change.

Figure 5 Sensitivity tests showing modeled horizontal and vertical gradient change between the LGM and Holocene compared to data

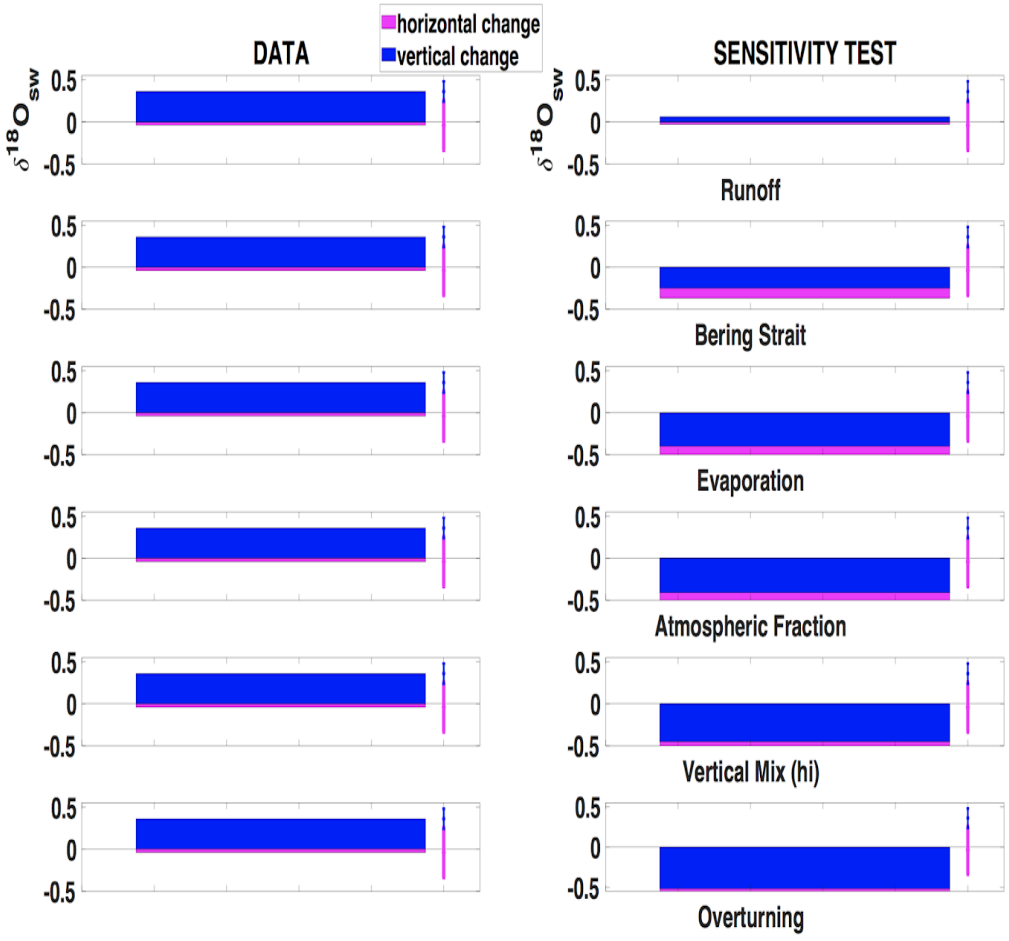

Figure 5 This graph illustrates the main findings of **Table 5a** and **Table 5b** above: Sensitivity tests (right) as compared to data (left). Sensitivity test shows results of changing one modeled parameter at a time to the modern model value. Color bars indicate surface change (magenta), vertical change (blue). The Runoff experiment is within error for the surface change. Changing runoff shows the closest values as compared to the data and is able to produce the only positive vertical change value. A positive vertical change is difficult to achieve because the deep box values must lie between the two surface box values. (Note: the model here explores gradient changes rather than absolute box changes because the absolute value of the LGM-to-Holocene change varies by geographic location.

Table 6 Summary table of combined experiments (intermediate evaporation and fraction of transport, low temperature and vertical mixing)

Experiment number	LGM with 2.2 Sv of overturning	Δ surface gradien	Δ vertical gradient
	MARGO Proxy sites	-0.04	0.34
1	Runoff: 0.18	0.24	0.25
2	0.14	0.07	0.10
3	0.12	-0.02	0.03
4	0.10	-0.11	-0.04
5	0.05	-0.33	-0.22
6	0.018	-0.46	-0.34
	LGM scenarios with 3.3 Sv of overturning	Δ surface gradient	Δ vertical gradient
7	Runoff: 0.18	0.03	0.10
8	0.14	-0.11	-0.03
9	0.12	-0.19	-0.29
10	0.10	-0.26	-0.15
11	0.05	-0.43	-0.31
12	0.018	-0.57	-0.42

Table 6 Modified experiments Effects on change from LGM with combined parameter changes of intermediate evaporation and fraction of transport. We see a large positive gradient in experiment 1, but this experiment yields a nearly equal surface gradient change.

Figure 6 Best modified runoff test from Table 6 (Experiment 7)

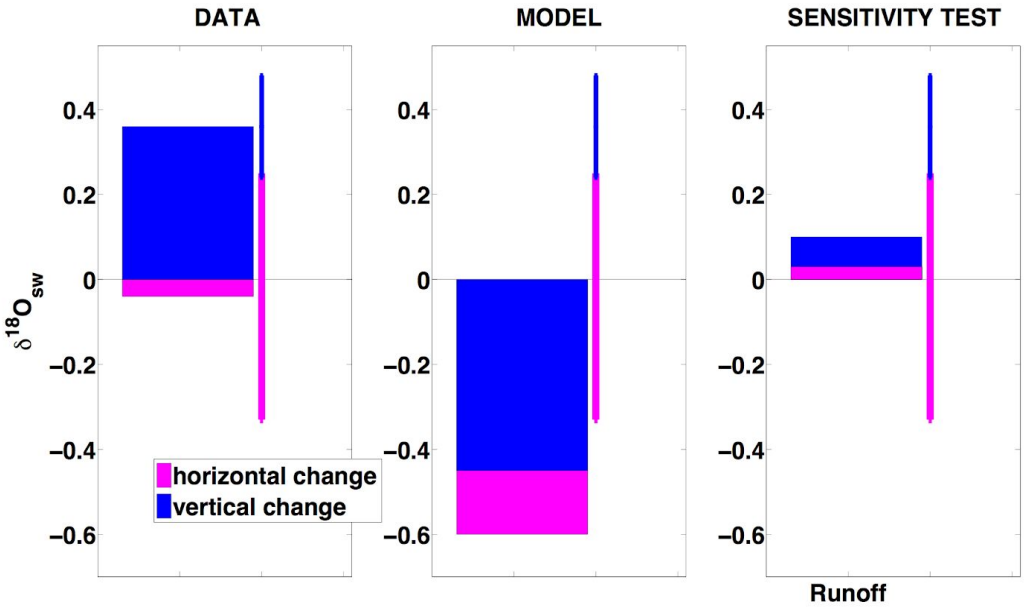

Figure 6 Experiment 7 (right, and Table 6, line 7, above) with 3.3 Sv of overturning, (intermediate evaporation and fraction of transport, low temperature and vertical mixing). Data error bars to the right of each figure. By increasing Arctic runoff, experiment 7 is able to achieve a small horizontal gradient change while achieving a modest positive vertical change, indicating more testing of the runoff parameter is warranted.The modeled surface sensitivity is within the error of the data in this experiment.

5 Discussion

5.1 LGM model and data comparison

The model's surface gradient change is -0.6 ‰ as compared to -0.45‰ in the vertical gradient at the LGM. The greater change in the surface gradient between the LGM and the Holocene could imply greater changes in surface processes between the 2 eras than in the deep ocean. However, because the deep ocean reflects the modern high-latitude surface ocean, there are likely stronger vertical gradient changes than horizontal. For example, more changes in surface-based processes such as evaporative transport, fraction of vapor transport across 50° N, and runoff may have occurred at the LGM which then affected surface-to-deep processes which include vertical mixing and overturning circulation.

The change in the modeled surface gradient (Table 5a) is -0.6‰ from 0.35‰ at the LGM to 0.95‰ in the Holocene. This change indicates a depletion of the low-latitude surface ocean relative to the high latitude surface ocean in the model at the LGM. However, the MARGO data indicate very little change in the surface gradient at the LGM, of -0.04 +/- 0.29 (one standard deviation).

The change in the model's vertical gradient (Table 5b) is -0.45‰ from 0.30‰ at the LGM to 0.75‰ in the Holocene. This change indicates a depletion of the low-latitude surface ocean relative to the high latitude deep ocean by -0.45 ‰ in the model at the LGM. However, the combined pore water and benthic $\delta^{18}O_{sw}$ data indicate a positive vertical change of 0.78 (+/-0.03) ‰ at the LGM.

5.2 Interpretation of gradient changes

The purpose of this study is to test whether reconstructed estimates of LGM circulation changes can reproduce the observations in the data at the LGM. When comparing these effects to the data, one can make hypotheses about how various model changes will affect the horizontal and vertical gradients (comparisons of change between the boxes).

Mean ice volume changes, (ice volume effects) will be defined as a mean change between the 2 time periods, affecting all boxes equally. These effects may be inferred by the comparison of horizontal and vertical gradient changes to the changes in the individual boxes; whereas gradient changes will not be affected by mean-state changes in all reservoirs, individual boxes will. For example, a horizontal change of nearly 1.15 ‰ occurred in both surface boxes, with a relative vertical enrichment of nearly 0.4 ‰. This suggests that the 3

Atlantic areas changed with a possible mean enrichment of 0.4 ‰ throughout the entire Atlantic at the LGM, with a stronger relative enrichment of the low and high latitude surface ocean of 0.75 ‰ relative to the deep ocean.

Mathematically, however, it is not possible to have a model value in the deep box that is lower than the values of the two surface boxes, because the modeled value of the deep box must remain in-between the values of the 2 surface boxes. Therefore, the mechanics of a strongly enriched surface as compared to the deep remains an unexplored possibility; this chapter will only explore the variation in the changes of the two gradients as the result of regional effects rather than exploring the mean change across the time periods.

The model has two opposing regional effects: individually, the effect of slowing each of the freshwater transport parameters brings the $\delta^{18}O_{sw}$ of all three boxes closer together, making the change negative between each of the boxes between the two time periods. Conversely, the effect of slowing each of the ocean flux parameters makes the $\delta^{18}O_{sw}$ of all three boxes farther apart, with positive change between all boxes between the two time periods.

Thus, the similar $\delta^{18}O_{sw}$ responses in both surface boxes suggests the same mixing and freshwater transport parameters between the two time periods or a slowed mixing combined with increased freshwater transport.

Conversely, the positive vertical gradient change implies enrichment of the deep ocean with slowed mixing or decreased freshwater transport, or both.

With the horizontal and vertical gradients taken together, it is possible to have slowed mixing parameters at the LGM as compared to the modern. Following a slowed mixing run, sensitivity tests with variations in the freshwater parameters might achieve the desired effects in the surface and deep gradients.

5.3 Sensitivity test results

Because the model's results don't match the data, the sensitivity tests in this chapter have a two-fold purpose: 1) to find logical combinations of parameters which could match the LGM MARGO data and 2) to determine the extent to which $\delta^{18}O_{sw}$ gradients are affected by different circulation parameters and, thus, have the potential to provide constraints for LGM circulation changes. If the model's $\delta^{18}O_{sw}$ gradients are not sensitive to changes in a particular parameter, then observations of $\delta^{18}O_{sw}$ gradients cannot be used to provide

estimates of how that parameter may have varied in the past. Collectively, the sensitivity tests help to clarify reasonable ranges in parameter choices at the LGM:

First, the surface gradient in the MARGO data changes very little between the LGM and modern. Therefore, sensitivity tests which achieve a modern surface gradient with LGM parameter configurations provide a potential scenario for LGM circulation that is consistent with $\delta^{18}O_{sw}$ data . Second, the model sensitivity tests are able to explore the relative impact of each parameter change on the LGM $\delta^{18}O_{sw}$ gradients further clarifying how each parameter affects the model's outcome.

The sensitivity tests that freshwater flux was generally slower at the LGM than the modern, following the literature that vapor export from the low-to the high-latitudes was slower at the LGM, as described in Appendix B. Slower freshwater transport creates negative anomalies between the 2 eras as seen in Table 2b.

Additionally, some complex models continue to show faster overturning in some cases; faster mixing at the LGM also creates negative vertical and surface anomalies between the LGM and Holocene. The reconstructions shown in Figure 4 and Table 4 show little to slightly positive vertical gradients at the LGM, indicating little surface-to-deep mixing changes to slightly weaker surface-to-deep mixing changes at the LGM.

Sensitivity test results (Tables 5a and 5b, Figures 5 and 6) are analyzed to investigate : 1) how generally slower parameters at the LGM could create a near zero change in the surface gradient and: 2) how many parameters recreate gradients seen in the reconstructions, the model explores.

5.2.1 Sensitivity tests compared to the LGM data

From the results of the simple model, a variety of vertical mixing strengths and atmospheric transport values at the LGM are possible because their effects on the modeled vertical gradients show lower sensitivity. When given modern parameter values (with all other model parameters kept at LGM configurations, greater high-latitude vertical mixing increases the model's surface gradient by 101%. Therefore, close-to-modern surface to deep mixing is capable of recreating the LGM-type gradients in the data, giving credence to hypotheses that strong surface-to deep mixing occurred at the LGM (Burke et al., 2015).

Likewise, the modeled vertical gradient change of -0.45‰ (Table 5b) from the LGM to the Holocene is nearly achievable with 60% of the overturning circulation and modified atmospheric transport parameters (Table 6, experiment 12).

However, a modern-day low-latitude temperature of evaporation is unlikely despite the relative insensitivity of the model in both the surface and vertical gradient at 102% (Tables 5a and 5b). The model insensitivity indicates that the model does not constrain temperature or vertical mixture well in the vertical gradient, but it also illustrates that a variety of temperatures and vertical mixing values will yield the same modeled change between the Holocene and the LGM. From the viewpoint of the simple model, the modern high latitude vertical mixing parameter, e.g. modern-strength high-latitude mixing from the surface to the deep supported by Burcke et al. (2015) cannot be ruled out at the LGM.

5.3 Implications for Arctic runoff

Sensitivity tests yielding a modern surface gradient indicate similarity with the surface data because the MARGO data indicate little change between the Holocene and LGM.

Runoff, evaporation, and fraction of transport when decreased make the gradient change smaller between the low and the high latitudes in the model. Because of the model's lowered sensitivity [89-91% in the vertical change] to atmospheric transport, a modern gradient is plausible with a variety of atmospheric transport values.

The sensitivity tests indicate that increasing runoff from 0.018 Sv to 0.18 Sv while leaving all other parameters alone is enough to move the surface gradient change from a value of -0.6‰ to a value of -0.03‰ , by widening the LGM surface gradient (Table 5a, Figure 3), which is nearly identical to the proxy results in the surface gradient of -0.04 +/-0.29 (Table 1a). Interestingly, the modern runoff sensitivity test creates a surface gradient of 0.92‰ which is very close to the modern model run surface gradient of 0.95‰ (Table 5a, row 1). This is an important result because sensitivity tests indicate that altering runoff while decreasing the other parameters is enough to create a near zero surface gradient change between the two time periods. This sensitivity test therefore illustrates that a 'modern-type' surface gradient is achievable at the LGM by changing the runoff parameter alone.

The sensitivity results of the runoff tests indicate that carefully choosing runoff constraints will be important for future simulations of LGM gradients. Flux through the Arctic from the Atlantic may not have occurred through the Fram Strait at the LGM, some meltwater flux from the Barents ice sheet may have occurred, lowering mass balance of calcite by approximately 0.3 ‰ as compared to measurements from the Eastern and central Fram Strait (Nørgaard-Pedersen et al., 2003). Thus, although stable isotope values in calcite cannot be taken as direct measurements of flux changes, we choose an LGM value of

sensitivity tests of 10% of and 55% of modern runoff in order to discern the magnitude of the effect that runoff has on the modeled gradients between the LGM and modern.

Runoff as high as modern seems unlikely. However, because LGM ice-sheets can be more depleted than modern runoff (*-20 ‰ in the model*) and may range from -40 to -17 ‰ (Duplessy et al, 2002), ice-sheet calving into the Arctic at the LGM could create the same experimental 'runoff' result with up to ½ of the volume of water exchange (0.09 Sv). Thus, study of runoff constraints and ice-sheet depletion are important to modeling the LGM $\delta^{18}O_{sw}$ gradients.

To determine the ability of the model to achieve a modern surface gradient with mostly LGM parameters, a modified experiment combining reduced overturning of 2.2 Sv and increased runoff achieved a nearly zero surface gradient (Sensitivity experiment 3, Table 6). Similarly, a sensitivity test with slightly faster LGM flux of 3.3 Sv but with modern Runoff shows that very little surface change is achievable with modern runoff (Sensitivity experiment 7, Table 6, Figure 5). However, a less dramatic but positive vertical gradient change is achieved with 0.1 ‰ change between the 2 eras.

5.4 Model vs. reconstructions

In contrast with the proxy data and model results in Table 2a,b the volume-averaged reconstructed surface gradient change in three separate inverse LGM reconstructions are all positive, varying from 0.13 to 0.92‰ (Figure 4, Gebbie, 2014; Gebbie, 2015). The inverse model vertical gradient change may be mostly positive because the water masses in the interior of the ocean are mapped from surface observations with a tracer trajectory, and rates of transport are not taken into account. Surface data at the LGM indicate at least a 0.5‰ positive change between the 2 eras, which may ultimately reflect the surface to deep change in the inverse model runs. The inverse models suggest an enrichment of the low-latitude surface ocean at the LGM as compared to the high-latitudes.

When comparing the model's vertical gradient between the LGM and the Holocene with the vertical gradient in the data (Table 2a), the model's vertical gradient change of -0.45‰ is of opposite-sign with the proxy data result of 0.36‰ (Table 4). The positive vertical gradient change in the data might imply that the direction of enrichment is towards the surface ocean at the LGM. However, because the data's surface gradient change is near zero (Table 4) at

-0.04‰, this implies the magnitude of the deep ocean change is smaller than the magnitude change of the 2 surface boxes of ~1.15‰. The deep ocean change in the data from the LGM to the Holocene is 0.78‰ with a vertical change of 0.36‰. A similar vertical LGM-to-Holocene change of 0.31‰ is present in the Gebbie (2014) alt. reconstruction (Figure 4).

5. 5 Model limitations

The deep ocean is difficult to model using the simple 3-box model. The model's constraints require the deep ocean $\delta^{18}O$ concentration to be intermediate within the range of the low-latitude surface ocean and the high-latitude surface ocean, whereas the deep ocean of the real-world Atlantic is also influenced by the Southern Ocean. Therefore further study and expansion of the model to a comprehensive whole-ocean study is warranted. Mixing with other oceans will affect the deep box concentration. Deep-box values will also be affected by limitations of the model in its simple atmospheric transport which will affect surface to deep concentrations. Keeping the ocean depth constant between the Holocene and LGM may also alter the concentration of the vertical gradient.

When evaluating agreement between gradient changes in the model and proxy data, it is also important to remember that the relatively high error of +/- 0.26‰ in the high-latitude surface ocean and +/- 0.12‰ in the low-latitude surface ocean makes model-data comparison difficult. Additional $\delta^{18}O_{sw}$ data or improved measurement precision would improve the model's ability to constrain the LGM circulation state.

6 Conclusions

With an improved atmospheric transport with Rayleigh fractionation physics and utilizing a model mean of paleoclimate model intercomparison models, this study simulates $\delta^{18}O_{sw}$ gradient changes between the Holocene and LGM using a 3-box model. Parameter values were estimated based on the literature. Because overturning estimates vary, sensitivity tests are used to evaluate the effects of different overturning values.

Gradient changes between the model surface boxes are compared with the horizontal surface gradients in the proxy observations, which comprise about 50 pairs of $\delta^{18}O_{sw}$ estimates in both the LGM and Holocene. The data show little surface gradient change between the LGM and Holocene and a positive vertical gradient change between the 2 eras. However, the model shows a negative surface and vertical gradient change between the 2

eras. Although the data have large error bars, the LGM model results are not consistent with the data.

Likewise, the LGM to Holocene anomaly in the vertical gradient is negative whereas it is positive in the combined pore-water and sediment-core data. It is likely that the data-model misfit arises because the model lacks the Antarctic Bottom water influence of the Southern Ocean.

The combined experiments provide the opportunity to evaluate whether changes in the atmospheric and oceanic mixing parameters can match the gradients in the data. The small surface change between the modern and LGM is achievable with a variety of parameter alterations, including increasing runoff and combined sensitivity experiments with modified atmospheric parameters and 60% of modern overturning. A positive change in the vertical gradient, similar to that observed in the data, is achievable with increased runoff alone. It is difficult to achieve positive change in both the surface and the vertical gradients in the model because the model must derive a deep box value which is between the modeled values in the 2 surface reservoirs. Experiment 1, Table 6, does achieve a small surface change in the surface gradient with a vertical change of 0.1‰. Future studies with global coverage will

allow the model to explore in more detail the contribution of the Indian and Pacific Ocean to ice volume change at the LGM.

The results indicate it is possible to achieve the near-zero surface gradient change apparent in the data using a modeled modified atmospheric transport and modern Arctic runoff, with all other LGM parameters remaining at their original specifications. Similar to the data, a positive vertical gradient change in the model is achievable with Arctic runoff at near modern levels. However, Arctic runoff in the model can represent a combination of multiple processes at the LGM, including melting or calving of continental ice sheets; because these ice sheets would be more isotopically depleted than modern river runoff, fluxes can be smaller than modern in proportion to the change in isotopic composition of the runoff flux.

7 References

Adkins, J.F., Schrag D.P., Pore fluid constraints on deep ocean temperature and salinity during the last glacial maximum,Geophys. Res. Lett., 28(5), 771–774, 2001.

Adkins J.F., McIntyre K., Schrag D.P.: The salinity, temperature, and delta ^{18}O of the glacial deep ocean, Science. Nov 29; 298(5599):1769-73, 2002.

Archer, D. F., Eshel, G.., Winguth, A., Atmospheric pCO_2 sensitivity to the biological pump in the ocean, Global Biogeochemical Cycles, 14 (4), 1219-1230, doi:/10.1029/1999GB001216, 2000.

Ballarotta, M., Brodeau, L., Brandefelt, J., Lundberg, P., Doos, K., Last Glacial Maximum world ocean simulations at eddy-permitting and coarse resolutions: do eddies contribute to a better consistency between models and palaeoproxies? Clim. Past, 9, 2669–2686, 2013.

Battisti, D, Ding, Q., Roe, G.H.: Coherent pan-Asian climate and isotopic response to precessional forcing, J. of Geophy. Research, 119 (21), 11,997-12,020,doi:/10.1002/2014JD021960, 2014.

Boehm E., Lippold, J., Gutjahr, M., Frank, M., Blaser, P., Antz, B., Fohlmeister, J., Frank, N., Andersen, M.B., Deininger, M..: Strong and deep Atlantic meridional overturning circulation during the last glacial cycle. Nature volume 517, pps.73–76, 2015.

Burke, A., Stewart, A. L., Adkins, J. F., Ferrari, R., Jansen, M. F., and Thompson, A. F.: The glacial mid‐depth radiocarbon bulge and its implications for the overturning circulation, *Paleoceanography*, 30, 1021– 1039, doi:10.1002/2015PA002778, 2015.

Burckel, P., Waelbroeck, C., Luo,Y., Roche, D.M., Pichat, S. et al.: Changes in the geometry and strength of the Atlantic meridional overturning circulation during the last glacial (20–50 ka). Climate of the Past, European Geosciences Union (EGU), 2016, 12 (11), pp.2061-2075, doi: 10.5194/cp-12-2061-2016,hal-01587574, 2016.

Craig, H., Gordon, L.I., Deuterium and oxygen 18 variations in the ocean and marine atmosphere, in Tongiorgi, 15., ed., Stable isotopes in oceanic studies and paleotemperatures (Third SPOLETO Conference on Nuclear Geology: Pisa, Consiglio Nazionale Delle Richerche, Laboratorio di Geologia Nucleare, p. 9—130, 1965.

Caley, T., Roche, D.M., Waelbroeck, C., Michel, E., Oxygen stable isotopes during the Last Glacial Maximum climate: perspectives from data–model (iLOVECLIM) comparison, Clim. Past, 10, 1939–1955, doi:10.5194/cp-10-1939-2014, 2014.

Caley, T. and Roche, D. M.: δ18O water isotope in the iLOVECLIM model (version 1.0) – Part 3: A palaeo-perspective based on present-day data-model comparison for oxygen stable isotopes in carbonates, Geosci. Model Dev., 6, 1505–1516, doi:10.5194/gmd-6-1505-2013, 2013.

Dickinson R.E., Sellers A.H., Kennedy P.J., Biosphere atmosphere transfer scheme (BATS) version 1e as coupled to the NCAR Community Climate Model. NCAR Tech Note, NCAR/TN-387+STR, National Center for Atmosphere Research Boulder, Colorado, USA,1993.

Dufresne, JL., Foujols, MA., Denvil, S. et al., (2013), Climate change projections using the IPSL-CM5 Earth System Model: from CMIP3 to CMIP5, Clim Dyn 40: 2123, doi.org/10.1007/s00382-012-1636-1, 2013.

Duplessy J.C., Labeyrie, L., Waelbroeck,C.: Constraints on the ocean oxygen isotopic enrichment between the Last Glacial Maximum and the Holocene: Paleoceanographic implications Quaternary Science Reviews 21 315-330, 2002.

Ganopolski A., Rahmstorf, S.: Rapid changes of glacial climate simulated in a coupled climate model, Nature. Jan 11;409(6817):153-8, 2001.

Gebbie, G., Tracer transport timescales and the observed Atlantic-Pacific lag in the timing of the Last Termination, Paleoceanography, 27, PA3225, doi:10.1029/2011PA002273, 2012.

Gebbie, G.,How much did Glacial North Atlantic Water shoal?, Paleoceanography, 29, 190– 209, doi:10.1002/2013PA002557, 2014.

Gebbie, G.Peterson, C.D. Lisiecki, L.E., and Spero H.J., Global-mean marine d13C and its uncertainty in a glacial state estimate. Quaternary Science Reviews, 125, doi://10.1016/j.quascirev.2015.08.010, 2015.

Gordon, C.C., Cooper, C.A., Senior C.A. et al.: The simulation of SST, sea ice extents and ocean heat transports in a version of the Hadley Centre coupled model without flux adjustments, Volume 16, Issue 2–3, pp 147–168, 2000.

Gu, S.,Liu, G., Lynch-Stieglitz, J., Jahn, J., Jhang, J., Wu, L..: Assessing the ability of Zonal $\delta^{18}O$ contrast in benthic foraminifera to reconstruct deglacial evolution of Atlantic Meridional Overturning Circulation, Paleoceanography and Paleoclimatology, doi:/full/10.1029/2019PA003564, 2019.

Gutjahr M., Frank, M., Stirling, C.H., Keigwin, L.D., Halliday, A.N.: Tracing the Nd isotope of North Atlantic Deep and Intermediate Waters in the western North Atlantic since the Last Glacial Maximum from Blake Ridge sediments, Earth and Planetary Science Letters 266 (2008) 61–77, 2008.

Hasumi and Emori , Hasumi H., Emori S. K-1 Coupled GCM (MIROC) Description Center for Climate System Research, University of Tokyo, 2004.

Jungclaus, J. H., Fischer, N., Haak, H., Lohmann, K., Marotzke, J., Matei, D., Mikolajewicz, U., Notz, D., and von Storch, J. S.: Characteristics of the ocean simulations in MPIOM, the ocean component of the MPI-Earth system model, *J. Adv. Model. Earth Syst.*, 5, 422– 446, doi:/10.1002/jame.20023, 2013.

Kitoh, A., Shigenori, M., A Simulation of the LAst Glacial Maximum with a coupled atmosphere-ocean GCM, Geophysical Research Letters, Vol. 20, No. 11, pp 2221-2224, 2001.

LeGrande, A.N., Schmidt, G.A.: Global gridded data set of the oxygen isotopic composition in seawater. Geophys. Res. Lett., 33, L12604, doi:10.1029/2006GL026011, 2006.

Lynch-Stieglitz, J., Adkins, J., Curry, W.B., Dokken, T., Herguera, J.C., et al.: During the Last Glacial Maximum Atlantic Meridional Overturning Circulation, Science 316, 66, 2007.

Majoube, M., Fractionnement en oxygène-18 et en deuterium entre l'eau et sa vapeur. J . Chin,. Phys., 68, 1423- 1436, 1971.

Mix, A, Constraints on timing and extent of ice-growth events (120-65 ka): Special Paper, Geological Society of America, 270, The Last Glacial-Interglacial Transition, Peter D. Clark, ed., pp. 19-30, doi.org/10.1594/PANGEA/836033, 1992.

McManus, J., Francois, R., Gherardi, J. et al.: Collapse and rapid resumption of Atlantic meridional circulation linked to deglacial climate changes. *Nature* 428, 834–837 doi:10.1038/nature02494, 2004.

Nørgaard-Pedersen, N et al.: Arctic Ocean during the Last Glacial Maximum: atlantic and polar domains of surface water mass distribution and ice cover. *Paleoceanography*, 18(3), 1063, https://doi.org/10.1029/2002PA000781, 2003.

Notz, D., Haumann, F. A., Haak, H., Jungclaus, J. H., and Marotzke, J.: Arctic sea‐ice evolution as modeled by Max Planck Institute for meteorology's Earth system model, J. Adv. Model. Earth Syst., 5, 173– 194, doi:10.1002/jame.20016, 2013.

Patton, H., Hubbard, A., Andreasson, K., Auriac, A et al., Deglaciation of the Eurasian ice sheet complex, Quaternary Science Reviews 169 148-172, 2017.

Peltier and Solheim: The climate of the Earth at Last Glacial Maximum: Statistical equilibrium state and a mode of internal variability, Quaternary Science Reviews 23(3):335-357, 2003.

Piotrowski A. M., Goldstein, S., Hemming, S., Fairbanks, R.: Temporal Relationships and Ocean Circulation at Glacial Boundaries Temporal Relationships of Carbon Cycling, Science 3 , 1933 (2005); 307, doi: 10.1126/science.1104883, 2005.

Roche, D.M.,: $\delta^{18}O$ water isotope in the iLOVECLIM model (version 1.0) – Part 1: Implementation and verification, Geosci. Model Dev., 6, 1481-1491, doi:10.5194/gmd-6-1481-2013, 2013.

Schmidt, G.A., M. Kelley, L. Nazarenko, R. Ruedy, G.L. Russell, I. Aleinov, M. Bauer, S.E. Bauer, M.K. Bhat, R. Bleck, V. Canuto, Y.-H. Chen, Y. Cheng, T.L. Clune, A. Del Genio, R. de Fainchtein, G. Faluvegi, J.E. Hansen, R.J. Healy, N.Y. Kiang, D. Koch, A.A. Lacis, A.N. LeGrande, J. et al.: Configuration and assessment of the GISS ModelE2 contributions to the CMIP5 archive. J. Adv. Model. Earth Syst., **6**, no. 1, 141-184, doi:/10.1002/2013MS000265, 2014.

Spratt, R. M. and Lisiecki, L. E., A Late Pleistocene sea level stack, Clim. Past, 12, 1079–1092, doi:/10.5194/cp-12-1079-2016, 2016.

Schrag, D.P., Adkins, J., McIntyre, K., Alexander, J.L., Hodell, D.A., et al..: The oxygen isotopic composition of seawater during the Last Glacial Maximum Quaternary Science Reviews 21 331–342, 2002.

Shackleton, N.: Attainment of isotopic equilibrium between ocean and water the benthonic foraminiferal species Uvigerina: Isotopic changes in the ocean during the last glacial Colloquez international du C. N.R.S., 1974.

Sosdian S,. Rosenthal, Y.: Deep-Sea Temperature and Ice Volume Changes Across the Pliocene-Pleistocene Climate Transitions Science, 306-310, 2009.

Vachon, R. W., Welker, J. M., White, J. W. C., and Vaughn, B. H.: Moisture source temperatures and precipitation δ18O-temperature relationships across the United States, Water Resour. Res., 46, W07523, doi:/10.1029/2009WR008558, 2010.

Voldoire, A., E. Sanchez-Gomez, D. Salas y Mélia, B. Decharme, C. Cassou, S.Sénési, S. Valcke, I. Beau, A. Alias, M. Chevallier, M. Déqué, J. Deshayes, H. Douville, E. Fernandez, G. Madec, E. Maisonnave , M.-P. Moine, S. Planton, D.Saint-Martin, S. Szopa, S. Tyteca, R. Alkama, S. Belamari, A. Braun, L. Coquart, F. Chauvin : The CNRM-CM5.1 global climate model : description and basic evaluation, Clim. Dyn., doi:10.1007/s00382-011-1259-y, 2011.

Waelbroeck, C., Kiefer, T. ,Dokken, T., Chen, M.-T., Spero, H.J., Jung, S.,Weinelt, M., Kucera, M., Paul, A., Constraints on surface seawater oxygen isotope change between the Last Glacial Maximum and the Late Holocene, Quaternary Science Reviews, Volume 105, Pages 102-111,ISSN 0277-3791,doi:/10.1016/j.quascirev.2014.09.020, 2014.

Weber S.L., Drijfhout, S.S., Abe-Ouchi, A., Crucifix, M. et al.: The modern and glacial overturning circulation in the Atlantic ocean in PMIP coupled model simulations Clim. Past, 3, 51–64, 2007.

Supplement 1

Surface Data: High latitude $\delta^{18}O_{sw}$ LGM and Holocene for model sensitivity tests

(Waelbroeck et al, 2014)

coordinates	Hol $\delta^{18}O_{sw}$ (‰)	assigned error	$\Delta\ \delta^{18}O_{sw}$ (‰)	$\Delta\delta^{18}O_{sw}$ 1-σ error
**77.26 9.09*	*0.40*	*0.20*	*1.29*	*1.34*
**75.60 1.30*	*0.19*	*0.20*	*1.05*	*0.74*
73.77 2.38	0.41	0.20	1.68	0.72
72.25 -9.23	-0.07	0.20	1.19	0.70
71.78 1.60	0.55	0.20	3.31	0.86
69.98 -18.08	-0.35	0.20	2.97	0.46
69.48 -9.51	0.29	0.20	1.51	2.01
68.43 -13.87	0.18	0.20	2.71	0.49
66.68 7.57	0.41	0.20	0.58	0.46
62.44 -4.00	0.77	0.20	1.62	0.50
62.37 -0.98	0.76	0.20	2.49	0.56
58.00 -16.51	0.51	0.20	-0.05	0.91
57.93 -29.10	0.35	0.20	1.92	1.31
55.50 -14.70	0.54	0.20	1.24	1.59
55.48 -14.70	0.54	0.20	1.43	1.54
54.64 -16.36	0.54	0.20	1.16	0.90
54.64 -16.36	0.54	0.20	1.60	0.92
52.50 -22.07	0.50	0.20	1.08	1.38
52.50 -22.07	0.50	0.20	0.53	1.37
50.69 -21.87	0.56	0.20	1.04	1.38
50.69 -21.87	0.56	0.20	0.67	1.38
	***Mean 0.43*(‰)**	***0.2*(‰)**	***Mean 1.18* (‰)**	***Mean of error: 0.26*(‰)**

Surface Data Table High-latitude surface box boundaries: 50°-74° N, 76° W- 20° E

**Measurements with Asterisk have been removed from final calculations because they are outside our reservoir boundaries for the high-latitude surface box in the Atlantic. Additionally, values greater than 2 ‰ are excluded from the mean.*

Table Low latitude $\delta^{18}O_{sw}$ LGM and Holocene data for sensitivity tests

coordinates	Hol $\delta^{18}O_{sw}$ (‰)	assigned error	$\Delta\ \delta^{18}O_{sw}$ (‰)	$\Delta\delta^{18}O_{sw}$ 1-σ error
43.50 -29.87	0.77	0.20	0.84	1.32
42.98 -55.25	-0.23	0.20	1.43	0.46
42.15 -9.7	0.69	0.20	1.41	0.64
42.04 4.15	1.88	0.20	0.47	0.58
41.76 -47.35	0.40	0.20	--	--
41.76 -47.35	0.40	0.20	--	--
41.52 17.98	2.04	0.20	1.19	0.57
41.28 17.62	2.04	0.20	1.29	0.62
41.28 17.62	2.04	0.20	1.62	0.47
41.10 4.84	1.71	0.20	0.83	0.56
40.58 11.71	1.82	0.20	0.77	0.63
40.58 -9.86	0.71	0.20	1.53	0.61
39.67 13.57	1.78	0.20	0.63	0.54
39.16 15.08	1.73	0.20	0.61	0.56
37.77 -10.18	0.95	0.20	1.29	0.62
37.74 -10.17	0.95	0.20	1.22	0.66
37.10 -9.48	0.99	0.20	1.17	0.84
37.09 -32.03	0.97	0.20	1.15	0.63
36.77 -9.85	1.00	0.20	1.69	0.75
36.69 12.28	1.54	0.20	0.76	0.63
36.69 12.28	1.54	0.20	0.36	1.42
36.69 12.28	1.54	0.20	0.99	0.80
17.43 -77.66	0.82	0.20	1.83	0.60
17.43 -77.66	0.82	0.20	1.76	0.54
12.75 -78.73	0.83	0.20	1.04	0.74
12.1 -61.4	0.69	0.20	1.26	0.49
11.57 -78.42	0.83	0.20	0.83	0.80
4.24 -43.67	0.84	0.20	1.28	0.43
-1.67 -12.43	0.81	0.20	0.46	0.60
-3.67 -37.72	0.86	0.20	1.14	0.48
-4.25 -36.35	0.89	0.20	0.99	0.49
-4.30 -37.09	0.87	0.20	1.51	0.49
-7.01 -34.44	0.94	0.20	1.24	0.44
-8.53 -34.02	0.95	0.20	1.19	0.41
-23.32 12.38	0.71	0.20	1.95	1.37
-27.52 -46.47	0.95	0.20	0.99	0.52
Mean	***Mean 1.08*(‰)**	***0.2*(‰)**	***Mean 1.14* (‰)**	M***ean of error (+/-0.12)***

Table Low-latitude surface box boundaries: *part 1* 18°-50° N, 100° W-20° E, *part 2* 10°-18°N , 88° W-20° E, *part 3* 42° S-10° N, 68° W-20° E *(Waelbroeck et al, 2014)*. *Underlines indicate boundaries of box part boundaries*

Table of all model runs, experiments listed change one parameter at a time

Expt	***ov***	***lo***	***hi***	***evap***	***T.***	***h***	*Vap*	***Run.***	***Low***	***High***	***Deep***	***vapor $\delta^{18}O$***	*Surface grad*	***Vert grad***
1) Mod	5.5	2	7	0.31	292	2	0.8	0.18	0.8247	-0.1252	0.0748	-19.2135	0.9499	0.7499
2) LGM	3.3	1.2	4.2	0.26	287	2	0.0	0.018	0.3968	0.0487	0.0967	-23.5201	0.3481	0.3001
3)Int ov	4.4	1.2	4.2	0.26	287	2	0.0	0.018	0.3583	0.0625	0.0987	-23.5576	0.2596	0.2596
4)Mod ov	5.5	1.2	4.2	0.26	287	2	0.0	0.018	0.3288	0.0720	0.1003	-23.5865	0.2285	0.2285
5)Int T	3.3	1.2	4.2	0.26	289	2	0.0	0.018	0.3927	0.0496	0.0970	-23.1073	0.3431	0.2957
6)Mod T	3.3	1.2	4.2	0.26	292	2	0.0	0.018	0.3867	0.0510	0.0973	-22.5040	0.3357	0.2894
7))Int hi	3.3	1.2	5.6	0.26	287	2	0.0	0.018	0.3988	0.0558	0.0966	-23.5181	0.3400	0.3022
8) Mod hi	3.3	1.2	7	0.26	287	2	0.0	0.018	0.4004	0.0611	0.0965	-23.5166	0.3393	0.3039
9)Int lo	3.3	1.8	4.2	0.26	287	2	0.0	0.018	0.3683	0.0336	0.0984	-23.5479	0.3347	0.2699
10) Mod lo	3.3	2	4.2	0.26	287	2	0.0	0.018	0.3600	0.0292	0.0989	-23.5560	0.3308	0.2611
11)Int evap	3.3	1.2	4.2	0.285	287	2	0.0	0.018	0.4193	0.0438	0.0956	-23.4981	0.3755	0.3237

12) Mod evap	3.3	1.2	4.2	0.31	287	2	0.0	0.018	0.4419	0.0388	0.0944	-23.4761	0.4031	0.3475
13)Int Ber	3.3	1.2	4.2	0.26	287	2	0.4	0.018	0.4853	0.0292	0.0921	-23.4337	0.4561	0.3932
14)Mod Ber	3.3	1.2	4.2	0.26	287	2	0.8	0.018	0.5850	0.0071	0.0868	-23.3363	0.5779	0.4982
15) Mod frac	3.3	1.2	4.2	0.26	287	2	0	0.018	0.4359	0.0401	0.0947	-20.4931	0.3958	0.3412
16)Int frac	3.3	1.2	4.2	0.26	287	2	0.	0.018	0.4175	0.0441	0.0957	-21.8995	0.3734	0.3218
17)Int run	3.3	1.2	4.2	0.26	287	2	0.	0.099	0.6302	-0.0028	0.0845	-23.2023	0.6330	0.5457
18) Mod. run	3.3	1.2	4.2	0.26	287	2	0.	0.18	0.8690	-0.0556	0.0719	-23.0592	0.9246	0.8134

Combine params	***ov***	***lo***	***hi***	***evap***	***T.***	***h***	***Vap***	***Run.***	***Low***	***High***	***Deep***	***Water vapor $\delta^{18}O$***	*Surface grad*	*Vertical grad*
19)Mod ex Arct, loT	5.5	2	7	0.31	287	2	0	0.018	0.3732	0.0540	0.0980	-20.5545	0.3192	0.2752
20)Mod ex Arctic lo ov, loT	3.3	2	7	0.31	287	2	0	0.018	0.4459	0.0260	0.0942	-20.4833	0.4199	0.3517
21) Mod ex Arctic hi ov, hiT	5.5	2	7	0.31	292	2	0	0.018	0.3634	0.0561	0.0985	-19.6656	0.2649	0.2649
22) Mod ex Arctic lo ov, hiT	*3.3*	*2*	*7*	*0.31*	*292*	*2*	*0*	*0.018*	*0.4335*	*0.0291*	*0.0949*	*-19.5969*	*0.4044*	*0.3386*
23) Modified runoff 0.094	*3.3*	*.2*	*4.2*	*0.31*	*292*	*2*	*0*	*0.094*	*0.6156*	*0.0004*	*0.0852*	*-23.3065*	*0.6152*	*0.5304*
24) Modified runoff 0.060	*3.3*	*.2*	*4.2*	*0.31*	*292*	*2*	*0*	*0.060*	*0.5171*	*0.0221*	*0.0904*	*-23.4026*	*0.4950*	*0.4267*
25) Modified runoff 0.025	*3.3*	*.2*	*4.2*	*0.31*	*292*	*2*	*0*	*0.025*	*0.4167*	*0.0443*	*0.0957*	*-23.5006*	*0.3724*	*0.3210*

Combine params	***ov***	***lo***	***hi***	***evap***	***Tem***	***hor***	***Vap.***	***Run.***	***Low***	***High***	***Deep***	***Vapor $\delta^{18}O$***	Surface grad	Vert grad
26) Low runoff, LGM overturning	3.3	1.2	4.2	0.285	287	2	0.0	0.018	0.4221	0.0387	0.0944	-21.8755	0.3834	0.3227
27) Moderate runoff, LGM overturning	3.3	1.2	4.2	0.285	287	2	0.0	0.18	0.9154	-0.0659	0.0695	-21.4127	0.9813	0.8459
28) Moderate runoff, LGM overturning	3.3	1.2	4.2	0.285	287	2	0.0	0.14	0.7965	-0.0396	0.0757	-21.5290	0.8361	0.7208
29) Moderate runoff, LGM overturning	3.3	1.2	4.2	0.285	287	2	0.0	0.12	0.7376	-0.0266	0.0788	-21.5866	0.7642	0.6588
30) Moderate runoff, LGM overturning	3.3	1.2	4.2	0.285	287	2	0.0	0.10	0.6790	-0.0136	0.0819	-21.6439	.6926	0.5971
31) Moderate runoff, LGM overturning	3.3	1.2	4.2	0.285	287	2	0.0	0.05	0.5339	0.0184	0.0895	-21.7857	0.5155	0.4444

32) Modern runoff, low overturning	2.2	1.2	4.2	0.285	287	2	0.0	0.18	1.0653	-0.1265	0.0618	-21.2661	1.1918	1.0035
33)Moderate runoff, low overturning	2.2	1.2	4.2	0.285	287	2	0.0	0.14	0.9234	-0.0910	0.0692	-21.4049	1.0144	0.8542
34)Moderate runoff, low overturning	2.2	1.2	4.2	0.285	287	2	0.0	0.12	0.8532	-0.0735	0.0729	-21.4736	0.9267	0.7797
35)Moderate runoff, low overturning	2.2	1.2	4.2	0.285	287	2	0.0	0.10	0.7834	-0.0561	0.0766	-21.5418	0.8395	0.7068
36)Moderate runoff, low overturning	2.2	1.2	4.2	0.285	287	2	0.0	0.05	0.6109	-0.0130	0.0856	-21.7104	0.6239	0.5253
37)Moderate runoff, low overturning	2.2	1.2	4.2	0.285	287	2	0.0	0.018	0.5021	0.0142	0.0913	-21.8168	0.4879	0.4108

9 Appendix: Cost function for each workspace:

```
clear all
close all

c=load('matlab_ex_1_ch_2.mat')
j=load('matlab_ex_2_ch_2')
k=load('matlab_exp_3_ch_2_26_19_19h')%
```

```
%% observed
vapor_d18_value=-10.8%
low_lat_obs=0.8363;%proxy data LeGrande & Schmidt North Atlantic
hi_lat_obs=-.0402;%volume weighted average
deep_oc_obs=0.0736;
f_obs=vapor_d18_value;
observational_data=[low_lat_obs,hi_lat_obs,deep_oc_obs,f_obs]
```

```
%%  cost functions for each workspace

c.cost_box_1=abs((c.box1(:,:,:,:,:,:))-(low_lat_obs));%cost evaluation for each box
c.cost_box_2=abs((c.box2(:,:,:,:,:,:))-(hi_lat_obs));
c.cost_box_3=abs((c.box3(:,:,:,:,:,:))-(deep_oc_obs));
c.cost_fr=abs((c.boxf(:,:,:,:,:,:))-(f_obs));
ccost=c.cost_box_1+c.cost_box_2+c.cost_box_3+c.cost_fr/1000;%Add the cost for each box for each input value
```

```
%%
j.cost_box_1=abs((j.box1(:,:,:,:,:,:))-(low_lat_obs));%cost evaluation for each box
j.cost_box_2=abs((j.box2(:,:,:,:,:,:))-(hi_lat_obs));
j.cost_box_3=abs((j.box3(:,:,:,:,:,:))-(deep_oc_obs));
j.cost_fr=abs((j.boxf(:,:,:,:,:,:))-(f_obs));
jcost=j.cost_box_1+j.cost_box_2+j.cost_box_3+j.cost_fr/1000;
```

```
%%
k.cost_box_1=abs((k.box1(:,:,:,:,:,:))-(low_lat_obs));%cost evaluation for each box
k.cost_box_2=abs((k.box2(:,:,:,:,:,:))-(hi_lat_obs));
k.cost_box_3=abs((k.box3(:,:,:,:,:,:))-(deep_oc_obs));
k.cost_fr=abs((k.boxf(:,:,:,:,:,:))-(f_obs));
kcost=k.cost_box_1+k.cost_box_2+k.cost_box_3+k.cost_fr/1000;
```

Inner function expt 3

```
function  [ dX1,dX2,dX3,dXf]=arrow_3_box_lo_to_hi_4_20_mass_b(X1,X2,X3,Xf,n,k,overturning,mix_l,mix_h,fraction_flux, mix_f);%input concentrations
%output change in concentration at each timestep

standard=.1107/55.55;
Y=((-20/1000)+1)*standard*55.55;  %runoff into high latitude surface box is -20 per mil
Z=((-1.1/1000)+1)*standard*55.55 ;%transport thru Bering Strait is -2 per mil
runoff=.18;%Sverdrup strength of runoff
lo_hi_expt=.8;%Transport thru Bering Strait

%fraction_flux=[ ];%fraction flux value from low to high latitudes: values are for each loop iteration 1-3
overturning_1_2=overturning-fraction_flux-runoff-lo_hi_expt;%overturning flux values from lo latitude box to high latitude box: values are for each loop iteration 1-3
SPYR=86400*365;               % secs per year

V=[1.4858e+16 1.8745e+15  2.7476e+17]; %volumes of the 3 ocean boxes in m^3: in order; low, high, deep

% for i=1:1:n; %number of time iterations for 18O concentration development through each cean box

% Flux matrix
F=[0 (overturning_1_2+mix_f+fraction_flux*(k)) mix_l ; %row one, box one flux values  1,1 (from box 1 to box 1) 1,2 (from box 1 to box 2 o_t)  1,3 (from box 1 to box 3 o_th)
    mix_f       0             (mix_h+overturning);        %row two, box two flux values  2,1 (from box 2 to box 1 t_o) 2,2 (from box 2 to box 2)  2,3 (from box 2 to box 3 t_th)
    (mix_l+overturning)  mix_h                  0];      %row 3,   box 3   flux values  3,1 (from box 3 to box 1 th_o) 3,2 (from box 3 to box 2 th_t)  3,3 (from box 3 to box 1)

F = F.*1e6;%Sverdrup conversion
%(mmol / [m^3])*(# Sv* 1e6 m^3/ yr) * (Sv)*(# seconds per yr)*(1/ ocean vol [#m^3])
runoff=runoff*1e6;
lo_hi_expt=lo_hi_expt*1e6;
dX1=(((F(3,1)*X3+F(2,1)*X2)-((F(1,2)+F(1,3))*X1)-runoff*Y-lo_hi_expt*Z))*SPYR/V(1); %box 1, surface low-lat
dX2=(((F(1,2)*X1+F(3,2)*X3+runoff*(Y)+lo_hi_expt*Z)-(F(2,3)+F(2,1))*X2))*SPYR/V(2); %box 2, surface high latitude
dX3=(((F(1,3)*X1+F(2,3)*X2)-(F(3,1)+F(3,2))*X3))*SPYR/V(3);% box 3, deep ocean
dXf=dX1;
```

Code main, expt 3

```
clear all
close all
conversion1 = 0.110712368610173;
%E=16
%H1=.110706



%%     traces the heavy isotope for each timestep
alpha=.9860:.0014:.9960;%matrix congtains increasing values of alpha for 18O
d=length(alpha);% d gives us the same length for all experiments


start=5.5; %base overturning before loop
strongest=7.5 ;
ov=start:.35:strongest;  %overturning flux value in Sverdrups: values are for each loop iteration 1-3
e=length(ov);

mix_l_start=1.6;
mix_low_latitude=mix_l_start:.14:2.6;
f=length(mix_low_latitude);

mix_h_start=5;
mix_high_latitude=mix_h_start:2:19;
g=length(mix_high_latitude);

at_fraction=.092:.009:.155;
h=length(at_fraction);

mix_horiz=1.85:0.85:7.85;
l= length(mix_horiz);

for q=1:e;%overturn from 13.5-17.5
    for r=1:f;%mix low latitude 4
        for s=1:g;%mix high latitude 5
            for t=1:d; %next change in alpha from .976 to .980
                for u=1:h; %atmos fraction
                    for m=1:l;%mix horiz
                        n=900;% timestep in years
```

Code main, continued

```
overturning=ov(q);
k1=alpha(t); %fractionation value for heavy isotope

mix_l=mix_low_latitude(r);
mix_h=mix_high_latitude(s);
fraction_flux=at_fraction(u);
mix_f=mix_horiz(m);
standard=.1107/55.55;   %Standard mean ocean water value in mmol/m^3

dH1=zeros(900,1);
dH2=zeros(900,1);
dH3=zeros(900,1);
dHf=zeros(900,1);
H1=zeros(901,1);
H2=zeros(901,1);
H3=zeros(901,1);
Hf=zeros(901,1);
%
H1(1)=  conversion1 ;  %Initial 18O concentration in mmol/m^3 for low latitude ocean box
H2(1)=  conversion1 ;  %Initial 18O concentration in mmol/m^3 for high latitude ocean box
H3(1)=  conversion1 ;  %Initial 18O concentration in mmol/m^3 for deep ocean box
Hf(1)=H1(1);


heavy_isotope=@arrow_3_box_lo_to_hi_4_20_mass_b;
% Creates an alias called 'heavy isotope'-for
% the box function

for i=1:n;
    % [PHL]=high_latitude_precipitation_flux_2_19(fraction_flux,f,k1,H1,H2);
    [dH1(i),dH2(i),dH3(i),dHf(i)]=heavy_isotope(H1(i),H2(i),H3(i),Hf(i),n,k1,overturning,mix_l,mix_h,fraction_flux, mix_f);

    %Calls the box function with the
    %initial 18O values for each box
    %returns the '-change in'- 18O
    %for each timestep for each box

    %This little loop generates the
    %isotope value at the next timestep
```

Code main, continued

```
                            H1(i+1)=H1(i)+ dH1(i);
                            H2(i+1)=H2(i)+ dH2(i);
                            H3(i+1)=H3(i)+ dH3(i);
                            Hf(i+1)=(H1(i+1))*k1;
                        end
                             %input(i)=(ov(i),mix_low_latitude(i),mix_high_latitude(i),alpha(i),at_fraction(i),mix_horiz(i))


                            %%     traces the light isotope for each timestep



                            box1(q,r,s,t,u,m)=(((H1(i+1)/55.55)./standard)-1)*1000;%d18O values for overturn experiment box1
                            box2(q,r,s,t,u,m)=(((H2(i+1)/55.55)./standard)-1)*1000;%d18O values for overturn experiment box2
                            box3(q,r,s,t,u,m)=(((H3(i+1)/55.55)./standard)-1)*1000;%d18O values for overturn experiment box3
                            boxf(q,r,s,t,u,m)=(((Hf(i+1)/55.55)./standard)-1)*1000;%d18O values for overturn experiment box3


                    end
                end
            end
        end
    end
%% figure
 figure (1)
 plot((((H1/55.55)/standard)-1)*1000,'o');
 hold on
 plot((((H2/55.55)/standard)-1)*1000,'o');
 hold on
 plot((((H3/55.55)/standard)-1)*1000,'o');
 title('single box evolution')
```

V Conclusions

The $\delta^{18}O$ of seawater ($\delta^{18}O_{sw}$) contains a signal of past sea level change on long timescales, corresponding to changes in the size large ice sheets on continents. In the first project of this dissertation, individual sea level records derived from the $\delta^{18}O$ of foraminiferal calcite and other methods were combined into a stack using Principal Components Analysis (PCA). Principal Component 1 (PC1) provides a eustatic sea level record for 800 ka derived from surface and deep data from the world's ocean basins. The sea level stack was to scaled eustatic sea level using an LGM value of −130 m at 24 ka based on a GIA-corrected coral compilation (Clark et al., 2009) and a Holocene value of 0 m at 5 ka.

Confidence in the common sea level signal among all the records in the stack derives from the fact that it explains 77%-82% of the variance in the records, and each record provided approximately equal loads to the stack (Sosdian and Rosenthal, 2009; Elderfield, 2012; Waelbroeck, 2002; Rohling et al., 2009; Rohling et al., 2013; Bintanja, 2005; Shakun

et al., 2014). Monte Carlo simulations were used to estimate the error associated with the set of records analyzed and the sea level scaling. The 95% confidence interval for sea level at the Last Glacial Maximum (18-25 ka) is specified to span 136 to 128 m below present day sea level. The sea level stack agrees to within uncertainty with other sea level constraints; it agrees to within 3 m of sea level estimates with glacial isostatic corrected sea level estimates for Marine Isotope Stage (MIS) 5e (119-126 ka) of 6-9 m (Dutton et al., 2015; Kopp et al., 2009) and for MIS 11 (399-408 ka) of 6-13 m (Raymo and Mitrovica, 2012). Because less data is available further back in time, the 95% confidence interval for Marine Isotope Stage 19 (761-782 ka) is less well constrained, spanning from 25 m below present day to 10 meters above present day sea level.

The sea level stack (PC1) has a 2000 year lag with respect to a stack of benthic $\delta^{18}O$ which contains both temperature and ice volume signal (Lisiecki and Raymo, 2005). This result suggests that temperature leads ice volume changes in the deep ocean despite a 0.9 correlation of the sea level stack with the benthic stack . Further quantifying the impact of

sea level change on benthic $\delta^{18}O_{calcite}$, the sea level stack accounts for 44% of the total spectral variance in the benthic $\delta^{18}O_{calcite}$ stack and 47% of the 100-kyr power in the benthic stack over the last 800 kiloyears.

Data for the individual records of sea level in this study come from the Atlantic, Pacific, combined Atlantic and Pacific records, the Red Sea, the Mediterranean sea, a global benthic calcite stack, and a global planktonic calcite stack (Sosdian and Rosenthal, 2009; Elderfield, 2012; Waelbroeck, 2002; Rohling et al., 2009; Rohling et al., 2013; Bintanja, 2005; Shakun et al., 2014). The regional variations from these individual records are described by principal components two and three PC2 likely reflects variation between the Atlantic and Pacific due to equal but opposite sign loading , and PC3 describes differences between the surface and the deep ocean.

To discern the local variation associated with circulation changes between cold and warm climate states, a simple box model of the Atlantic Ocean was fitted with literature mixing and vapor transport parameters. The simple model has 3 boxes representing the

low-latitude surface, the high latitude surface, and the deep ocean. It was tuned to the modern climate record of $\delta^{18}O$ of seawater in these three reservoirs by adjusting parameters for modern mixing and vapor transport within literature estimates. The modern data show a depleted high-latitude surface ocean as compared to the low-latitude surface ocean, while the deep ocean has a value between the two surface boxes (LeGrande and Schmidt, 2006; Waelbroeck et al., 2014).

Subsequently, the same model with a more realistic representation of atmospheric Rayleigh fractionation reconstructed similar gradients between the low and high latitudes, and between the surface and the deep. Although the model was made to incorporate a multi-model mean of temperature from a PMIP3 model mean, low-latitude temperature of evaporation had a very small effect on the model results. The model was compared to data for the cold climate at the LGM, determined from a compilation of LGM to Holocene data pairs for the surface (Waelbroeck et al., 2014), and deep Atlantic (Adkins et al., 2002). To simulate the LGM, the model used literature estimates for slower overturning (McManus,

2004; Bohm et. al, 2015) and slower mixing processes at the LGM. Additionally, multi-model means of three GCM models of the LGM were used to generate values for vapor flux and fraction of vapor flux across 50° N in the model. Like the ocean flux parameters, these model parameters were also smaller for the LGM than the modern.

The model produced a diminished surface gradient for the LGM compared to the Holocene. The surface gradient (low-latitude minus high-latitude box) changed by -0.6 ‰, from a gradient of 0.95 ‰ in the Holocene to 0.35‰ at the LGM. For comparison, the surface gradient change in the proxy data between the two time periods was very small, at -0.04 ‰ gradient change, maintaining an almost 0.5 ‰ gradient between the surface low and high latitudes for both time periods. However, paleoclimate estimates of this gradient change are very uncertain, with a range of +/-0.29 ‰ (one standard deviation). An alternate LGM simulation was able to match the observed horizontal gradient change by increasing the amount of continental runoff into the Arctic Ocean to the modern value of 0.18 Sv. The modeled change in the vertical gradient (low-latitude surface minus deep box) of -0.45 ‰

between the LGM and the Holocene also did not match the positive gradient change of nearly 0.4 ‰ in the data. Whereas parameter changes had success in modeling the observed surface gradient change, parameter changes were unable to fit the observed vertical change exactly. With increased runoff of 0.18 ‰ and slower overturning, the model solution achieved approximately two-thirds of the LGM vertical gradient change in the data. It may be impossible for a simple 3-box Atlantic model to fit the vertical gradient change exactly because the model does not consider any flow into the deep box from the Southern Ocean and, therefore, the deep box value must remain in between the end-member values of the $\delta^{18}O_{sw}$ of the two modeled surface boxes.

Future studies on Atlantic ocean gradients between the LGM and the Holocene will benefit from improved estimates of Arctic runoff at the LGM. Additionally, the propagated error in surface gradient change estimate is too large to conclude that the model is inconsistent with the data. Therefore, future studies on $\delta^{18}O_{sw}$ gradients between warm and cold periods will also require increased data availability from Atlantic sediment records.

Finally, a more complex box model that includes the Pacific and Southern oceans and more vertical levels could provide a more realistic depiction of ocean circulation changes for comparison with paleoclimate data .

In summary, similar patterns in global sea level were observed in five to seven individual records of sea level were combined into a 800-kyr long global stack. Using principal components analysis, PC1 shows a correlation of 0.9 to a record of the $\delta^{18}O$ of benthic foraminiferal calcite but also a 2-kyr lag. Sea level change is estimated to account for nearly 45% of the 100-kyr power of the benthic calcite stack.

Additionally, regional variation in the sea level records captured by the PC2 and PC3 inspired a modelling project to evaluate the impacts of Atlantic Ocean circulation change between the Holocene and the LGM. A simple three-box Atlantic model was compared to surface and deep gradients in $\delta^{18}O_{sw}$ in planktonic foraminiferal, benthic foraminiferal, and pore-water estimates. The data exhibit a surface gradient change in the data of -0.4 ‰ between the two time periods; the model was able to achieve this gradient by changing

Arctic runoff to its modern value. The vertical gradient was more difficult to recreate with the box model because of the simple three-box formulation. Despite this, nearly two-thirds of the gradient in the data was achieved by slowing the overturning circulation while increasing the runoff parameter to a modern value. Notwithstanding the success of the model in recreating the surface gradient in the data, the error in the proxy surface and vertical gradient change estimates is quite large (+/-0.29 ‰ and +/-0.12 ‰, respectively), suggesting a need for additional LGM $\delta^{18}O_{sw}$ measurements. An additional future improvement to this study would be a global ocean box model, which could include the influence of the Southern Ocean on Atlantic $\delta^{18}O_{sw}$ gradients.